Spatial organization of localized pulses in a self-imaging vertical external cavity surface emitting laser

Adrián Alejandro Bartolo González

UNIVERSITÉ CÔTE D'AZUR

ÉCOLE DOCTORALE
SCIENCES FONDAMENTALES ET APPLIQUÉES

THÈSE DE DOCTORAT

Structuration spatiale des impulsions localisées dans les lasers à émission surfacique avec cavité externe auto-imageante

Adrián Alejandro Bartolo González

Institut de Physique de Nice

Présentée en vue de l'obtention du grade de docteur en Physique **de** l'Université Côte d'Azur

Dirigée par : Massimo Giudici

Soutenue le : 13 Juin 2022

Devant le jury, composé de :

Thorsten Ackemann, Pr., University of Strathclyde

Mustapha Tlidi, Pr., Université Libre de Bruxelles

Giovanna Tissoni, Pr., Université Côte d'Azur

Arnaud Mussot, Pr., Université de Lille

Sylvain Barbay, D.R. CNRS, Université Paris-Saclay

Arnaud Garnache, D.R. CNRS, Universté de Montpellier

Massimo Giudici, Pr., Université Côte d'Azur

PROJET FINANCÉ PAR L'ANR · PROJECT FUNDED BY THE ANR
ANR
cnrs

Spatial organization of localized pulses in a self-imaging vertical external cavity surface emitting laser

BY

ADRIÁN ALEJANDRO BARTOLO GONZÁLEZ

THESIS SUBMITTED FOR OBTAINING THE DEGREE:

DOCTOR IN SCIENCES (PHYSICS)

SUPERVISED BY

PROF. MASSIMO GIUDICI

INSTITUT DE PHYSIQUE DE NICE

UNIVERSITÉ CÔTE D'AZUR

Structuration spatiale des impulsions localisées dans les lasers à émission surfacique avec cavité externe auto-imagéante

Jury:

Président
Giovanna Tissoni, Professeur, Université Côte d'Azur

Rapporteurs
Thorsten Ackemann, Professeur, University of Strathclyde
Mustapha Tlidi, Professeur, Université Libre de Bruxelles

Examinateurs
Giovanna Tissoni, Professeur, Université Côte d'Azur
Arnaud Mussot, Professeur, Université de Lille
Sylvain Barbay, D.R. CNRS, Université Paris-Saclay
Arnaud Garnache, D.R. CNRS, Universté de Montpellier

Directeur de Thèse
Massimo Giudici, Professeur, Université Côte d'Azur

Résumé

Cette thèse est consacrée à l'analyse expérimentale de la dynamique spatio-temporelle d'un laser à grand rapport d'aspect fonctionnant dans le régime de verrouillage de mode localisé dans le temps. Dans ce régime, le laser émet un ensemble périodique d'impulsions et chaque impulsion de cet ensemble peut être adressée individuellement par une perturbation externe. Par conséquent, ces impulsions sont des structures localisées dans le temps (SLT), l'équivalent, dans le domaine temporel, des structures localisées spatiales. Celles-ci ont été observée dans une grande variété de systèmes dissipatifs en biologie, chimie, botanique et en physique. Le système que nous étudions est un laser de semi-conducteur à émission surfacique à cavité externe (VECSEL) à base GaAs, où la cavité externe est délimitée par un miroir à gain et par un miroir absorbant saturable à semi-conducteur (SESAM). Ce dispositif a été conçu et développé en collaboration avec l'Institut d'Electronique et des Systèmes de Montpellier pour satisfaire aux conditions d'existence des SLT. Les III-V nanostructures ont été réalisées par la centrale technologique Renatech au Centre de Nanosciences et de Nanotechnologies de Paris. Des travaux préliminaires ont montré que ce système peut accueillir des SLT avec un profil transversal monomode.

Dans mon travail de thèse, j'étudie la possibilité de créer des SLT dans un VECSEL à grand rapport d'aspect, où la localisation spatiale et temporelle de la lumière deviendrait possible. Les structures localisées spatio-temporelles dans les systèmes dissipatifs, également appelées Balle de Lumière (BL), sont très attractives pour leur application au traitement de l'information car elles peuvent être utilisées pour encoder des bits d'information dans les trois dimensions du résonateur laser. Pour réaliser un VECSEL à grand rapport d'aspect il faut que la cavité externe soit auto-imageante et, en même temps, qu'une large section du miroir à gain soit pompée. J'ai identifié un protocole d'observation pour atteindre la condition auto-imageante (CAI) de la cavité externe. Ce protocole était essentiel pour établir la CAI car la pompe optique du VECSEL induit une lentille thermo-électronique parasite qui rend irréaliste toute tentative d'atteindre le CAI en positionnant les éléments optiques selon les calculs.

Lorsque l'on opère le VECSEL dans la limite de grand rapport d'aspect, c'est-à-dire près du CAI, des motifs spatiaux complexes apparaissent. Leurs caractéristiques dépendent du signe des coefficients B et C de la matrice $ABCD$ d'aller-retour de propagation dans la cavité externe. La transformation de Fresnel dans cette matrice montre que B contrôle le coefficient de diffraction du second ordre tandis que C introduit un profil de phase de masque quadratique sur le champ proche qui peut avoir un effet de focalisation ($C < 0$) ou défocalisation ($C > 0$). Pour $C < 0$, les motifs observés consistent en une combinaison d'une onde plane axiale avec un ensemble d'ondes plane inclinées ayant une disposition presque hexagonale dans l'espace de Fourier. Ces ondes planes sont verrouillées en phase et leur interférence donne naissance à un profil en nid d'abeille en champ proche. Pour $C > 0$, les motifs observés consistent en un ensemble de couples d'ondes plane inclinées ayants des vecteurs d'onde transversaux opposés. Différents couples présentent des vecteurs d'onde transversaux orientés différemment mais ayant le même module, ce qui dessine un cercle dans le profil de l'émission en champ lointain. Lorsque la symétrie rotationnelle est brisée par une anisotropie dans la cavité, seuls deux points sont observés dans le champ lointain et un rouleau apparaît dans le champ proche.

Dans le domaine temporel, ces motifs correspondent à des impulsions picosecondes, et je montre qu'ils peuvent être adressés individuellement via une perturbation optique externe ou en renvoyant une portion de l'émission avec un retard contrôlé ; il s'agit donc de motifs localisés dans le temps. Dans chaque situation, l'ensemble du motif pulse de manière synchrone et tous les points du profil de champ proche sont corrélés.

Même si le système n'émet pas spontanément de manière décorrélée, on peut l'induire à le faire en superposant à la pompe principale de faisceaux de pompage de taille faible qui permettent de contrôler le gain localement dans la section du VECSEL. Ainsi, j'ai pu créer des points sources émettant de motifs dont la pulsation est contrôlée individuellement et elle peut être asynchrone. Ces « points chauds » ont également été imprimé directement sur la facette supérieure du miroir de gain par le dépôt d'un masque de sous-longueur d'onde non diffractive absorbant en chrome. Ainsi, j'ai réalisé une preuve de principe pour la réalisation de sources multiplexées de motifs SLT dans le même VECSEL.

Mots clés : Structures Localisées, Laser à Cavité Externe Verticale Émettant par la Surface (VECSEL), Verrouillage de Modes Passif, Balles de Lumiére

Abstract

This thesis is devoted to the experimental analysis of spatio-temporal dynamics in a large aspect-ratio semiconductor laser operated in the regime of temporally localized mode-locking. In this regime the laser emits a periodic set of pulses and each pulse in this set can be individually addressed by an external perturbation. Hence, these pulses are Temporally-Localized Structures (TLS), the equivalent in time domain of the more famous Spatially-Localized Structure, which appear in many different dissipative systems in nature ranging from biology to physics. The system we study is a GaAs-based semiconductor Vertical External-Cavity Surface-Emitting Laser (VECSEL) where, the high finesse and large numerical aperture external cavity, is delimited by a gain mirror and by a Semiconductor Saturable Absorber Mirror (SESAM). This device was developed to match the requirements for hosting TLS in collaboration with the Institut d'Electronique et des Systèmes of Montpellier. The III-V nanostructures were realized by the technological facility Renatech at Centre de Nanosciences et de Nanotechnologies de Paris. Preliminary work has shown that this system can host TLS with a single transverse mode profile.

In my thesis work I address the possibility of implementing TLS in a large-aspect ratio VECSEL, where both spatial and temporal localization of light may be possible. Spatio-temporal localized structures, also called Light Bullets (LB), in dissipative system are very attractive for their application to information processing because they can be used to encode information bits in the three dimensions of a laser cavity. Large aspect-ratio VECSEL requires a self-imaging external cavity and, at the same time, a broad pumped area on the gain section. I have identified an observational protocol to achieve self-imaging condition (SIC) of the external cavity. This protocol was essential for establishing SIC because the optical pump of the VECSEL induces a parasitic thermo-electronic lens which affects SIC and makes unrealistic any tentative of reaching SIC by positioning optical elements according to calculations.

When operating the VECSEL in the limit of large aspect ratio, i.e. close to SIC, complex patterns appear, for instance self-amplitude and self-phase modulation. Their

characteristics depends on the sign of the B and C coefficients of the $ABCD$ round-trip matrix describing the propagation in the external cavity. Fresnel transformation in an $ABCD$ matrix approach shows that B controls the second order diffraction coefficient while C introduces a quadratic mask phase profile on the near field which may have a focusing ($C < 0$) or defocusing effect ($C > 0$). For $C < 0$ the patterns observed consist of a combination of an axial plane-wave with a set of tilted waves having a nearly hexagonal arrangement in the Fourier space. These plane waves are locked in phase and their interference gives birth to a honeycomb profile in near-field. For $C > 0$ the patterns observed consist of a set of counterpropagating tilted waves with opposite transverse wavevectors. These wavevectors share the same modulus and they draw a circle in the far field profile. When the rotational symmetry is broken by some anisotropy in the cavity, only two spots are observed in the far field and a roll pattern appears in the near-field.

In the time domain these patterns correspond to picosecond pulses, and I show they can be individually addressed via an external optical perturbation or by sending back an small portion of the emission with a controlled delay; hence they are temporally localized patterns. In each situation the entire pattern is pulsating synchronously, and all the points of the near-field profile are correlated.

Even if the system does not emit in a decorrelated way spontaneously, I have induced it by overlapping to the main pump small pump beams that create hot spots on the section of the gain mirror. By controlling the gain level on each of these hot spots, I have induced gain-pinned temporally-localized pattern which are pulsing asynchronously. These hot spots have been also engineered directly onto the top facet of the gain mirror through integration of sub-wavelength non-diffractive Chromium absorptive mask. Accordingly, I have realized a proof of principle for the realization of multiplexed sources of TLS patterns into the same VECSEL.

Key-words: Localized Structures, Vertical External Cavity Surface-Emitting Laser (VECSEL), Passive Mode-Locking, Light Bullets

Resúmen

Esta tesis está dedicada al análisis experimental de la dinámica espacio-temporal en un láser con gran relación de aspecto, operado en el regimen de *amarre de modos* (PML) localizados en el tiempo. En este regimen, el láser emite un conjunto de pulsos periódico, donde cada pulso puede ser manipulado individualmente mediante una perturbación externa. Por lo tanto, estos pulsos son *estructuras localizadas temporales* (TLS), siendo el equivalente en el dominio del tiempo de la estructura localizada espacial más famosa, que aparece en muchos sistemas disipativos diferentes en la naturaleza desde la biología hasta la física. Nuestro sistema de estudio es un *láser emisor de superficie de cavidad externa vertical* (VECSEL) fabricado a base de GaAs, donde la cavidad está delimitada por un espejo de ganancia y por un espejo semiconductor de absorción saturable (SESAM). Dichos dispositivos fueron diseñados para cumplir con los requisitos para obtener TLS en colaboración con el Institut d'Electronique et des Systèmes de Montpellier, y fueron desarrollados por el Centre de Nanosciences et de Nanotechnologies (C2N) de Paris. Trabajos preliminares han mostrado que este sistema puede albergar TLS con el modo fundamental transversal.

En esta tesis planteo la posibilidad de implementar TLS en un VECSEL con gran relación de aspecto, donde en principio la localización espacial y temporal de la luz podría ser posible. Las estructuras espacio-temporales localizadas, también conocidas como *balas de luz* (LB), en sistemas disipativos resultan de gran relevancia debido a que podrían usarse para codificar bits de información en las tres dimensiones de una cavidad láser. El VECSEL con gran relación de aspecto requiere una cavidad externa en condición de auto-imagen (SIC), y al mismo tiempo, un área del haz de bombeo en la sección de ganancia suficientemente grande. Así pues, he podido identificar un protocolo de observación para aproximar dicha condición de auto-imagen en la cavidad externa. Esto procedimiento resultó de gran relevancia, ya que el bombeo óptico induce una lente termo-electrónica en el medio de ganancia que afecta la condición de auto-imagen, y hace irreal cualquier intento de aproximarla colocando los elementos ópticos usando los parámetros de una cavidad pasiva.

Cuando el VECSEL es operado en el límite de gran relación de aspecto, es decir, cerca de SIC, aparecen estructuras espaciales, *i.e.*, patrones de luz, no triviales. Sus características dependen del signo de los coeficientes B y C de la matriz $ABCD$ de ida y vuelta que describe la propagación de la luz en la cavidad externa. La transformación de Fresnel en función de los parámetros $ABCD$ nos hace ver que B controla el coeficiente de difracción mientras que C introduce un perfil de fase cuadrática en el campo eléctrico, teniendo un efecto de enfoque ($C < 0$) o un efecto de desenfoque ($C > 0$). Para $C < 0$, los patrones observados consisten en una combinación de una onda plana axial con un conjunto de ondas inclinadas fuera de eje que tienen una disposición casi hexagonal en el espacio de Fourier. Estas ondas planas están en fase y su interferencia da lugar a un perfil de tipo panal de abeja en el campo cercano del medio de ganancia. Para $C > 0$, los patrones observados consisten en un conjunto de ondas inclinadas que se contrapropagan con vectores de onda transversales opuestos. Estos vectores de onda comparten el mismo módulo y dibujan un círculo en el perfil de campo lejano. Cuando la simetría rotacional se rompe por alguna anisotropía en la cavidad, solo se observan dos puntos en el espacio de Fourier que interfieren formando un patrón de franjas en el campo cercano del medio de ganancia.

En el dominio del tiempo, estos patrones corresponden a pulsos de picosegundos que pueden ser controlados individualmente; por lo tanto, son patrones localizados temporalmente. En cada situación, todo el patrón pulsa sincrónicamente y todos sus puntos del perfil amplitud de campo cercano están correlacionados.

Incluso si este sistema no emite espontáneamente de forma descorrelacionada en el espacio, esta se indujo superponiendo en el bombeo principal pequeños haces que crean secciones de mayor intensidad en la sección ganancia. Al controlar el nivel de ganancia en cada sección, se induce un patrón localizado temporalmente, acotado por dichos haces y que pueden pulsar de manera asíncrona. Estos puntos también se diseñaron directamente en la superficie superior del espejo de ganancia mediante la deposición de una máscara de absorción de cromo no difractiva. En consecuencia, ha sido posible la realización de una fuente de patrones multiplexados temporalmente localizados en nuestro VECSEL.

Palabras clave: Estructuras Localizadas, Vertical External Cavity Surface-Emitting Laser (VECSEL), Amarre de modos, Balas de Luz

A mis padres, Lulú y Felix

A mi hermana, Yeya

.

Agradecimientos

Todo gran logro es fruto de un gran esfuerzo. Una vez más he podido concretar una etapa que parecería ser la culminación de una larga carrera académica. Pero hace falta estar en este punto para darse cuenta que esto es sólo una transición hacia el sueño que tenemos muchos al empezar a estudiar física. Desde mis inicios como estudiante he tenido la fortuna de contar con personas que me han impulsado y motivado, por lo que las siguientes palabras no son suficientes para poder expresar lo agradecido que estoy con cada una de ellas.

Esta aventura comenzó aquella tarde en el metro de Múnich en camino hacia la CLEO-2017, donde esa charla primigenia, seguida de una buena excelente guía, ha dado como resultado la estructuración espacial de pulsos localizados en láseres de semiconductores. Así pues, agradezco a mi director de tesis, Massimo Giudici, por todo su apoyo durante estos casi cuatro años. Desde el primer día he recibido tus consejos, soporte, paciencia y enseñanzas. Gracias por tu confianza y por las oportunidades que se han abierto debido a nuestro trabajo. Ha sido un placer trabajar contigo. A Mathias Marconi, que me ha apoyado siempre y compartido toda su experiencia sobre pulsos localizados. Además, me demostró que la ciencia se tiene que hacer con mucho entusiasmo y que el mínimo descubrimiento merece una celebración. A los demás integrantes del proyecto ANR-BLASON. A Arnaud Garnache, por todos sus consejos y observaciones. Hemos empezado una nueva etapa y siempre agradeceré las nuevas oportunidades que me has brindado. A Nathan Vigne, con quien he compartido más de una vez el laboratorio, y que a lo largo de estos años me ha enseñado desde francés, hasta cómo disfrutar Montpellier. A Julien Javaloyes y Svetlana Gurevich por las interesantes discusiones que tuvimos sobre las observaciones experimentales. A Isabelle Sagnes, por el arduo trabajo que realizó con su equipo para la fabricación de nuestros dispositivos. Al director del instituto Guillaume Huyet, por todo el apoyo a los estudiantes, antes, durante y después de la pandemia. A los miembros de mi jurado, Thorsten Ackemann, Mustapha Tlidi, Giovana Tissoni, Sylvain Barbay y Arnaud Mussot, por sus comentarios y sugerencias sobre este trabajo.

En general al INPHYNI, donde a lo largo de estos años pude conocer mucha gente y compartir grandes experiencias. Empezaré desde luego por tres personas importantes, autodenominados *les Mousquetaires*: Alexis, Jesús y Pierre[†], con quienes empecé y terminé (casi) al mismo tiempo el doctorado. Una amistad que comenzó aprendiendo a preparar un buen café italiano, terminó siendo una hermandad. Me han brindado risas y discusiones, individualmente o en grupo, y han estado presente en momentos críticos para este trabajo. Les agradezco y les aseguro que hay Mosqueteros para muchos años más. A los demás estudiantes, postdocs, internos e investigadores, que han estado o continúan, y que tuve la ventaja de disfrutar su compañía. En particular a Julián, Amy, Ana, Patrice, Pierre L., Martial y Álvaro. A las personas de la administración, Nathalie, François y Christian, que a lo largo de estos años han realizado un trabajo arduo para el instituto. A mi comité de tesis, Gian Lucca y Jaques-Alexandre, por sus comentarios y siempre mantenerse al pendiente de mis avances.

A todas las personas que no están en Francia pero que me han brindado un sostén a lo largo de este tiempo. A Steph por la bella amistad que construimos. Las comidas y todos los paseos en Niza siempre estarán en mi memoria. Al futuro doctor Carlos Maciel, que hemos sido el escucha oficial uno del otro por más de tres años. No hay forma de agradecerte toda esa hermandad. A todos mis orígenes académicos en México. A la UNAM, por brindarme educación de calidad desde más de la mitad de mi vida. A Alessio, César, Lalo y Ángel, que siempre me brindaron su apoyo y conocimiento, desde aquellas tardes interminables en el Instituto de Materiales. A Karen Volke, con quien siempre estaré agradecido por sus enseñanzas, oportunidades y amistad. En general a todo el grupo de micro-manipulación óptica del IFUNAM. A todas mis amistades que han seguido al pendiente de mi carrera académica, y que, de acuerdo a ellos, se veía o sigue viendo *interminable*.

Finalmente quiero agradecer a mis padres, Lulú y Félix, y a mi hermana Andrea. Su cariño, apoyo y confianza, me ha permitido lograr todo en esta vida. Aun estando lejos, sus enseñanzas se mantienen en pie y me hacen salir adelante día con día. A toda mi familia de origen. A Loren que siempre quiso que compartieramos este momento con un buen mole. A Oscar y a Lau por todas las navidades y el acojo que me brindaron, y que han sido una gran parte de mi sustento familiar estos años.

Gracias a todos.

[†]Orden alfabético que no tiene relevancia alguna.

Contents

Index

LS Localized structure

TLS Temporal localized structure

SLS Spatial localized structure

PML Passive mode-locking

DDE Delay differential equation

SIC Self-imaging condition

TW Tilted waves

LB Light bullets

VCSEL Vertical cavity surface emitting laser

VECSEL Vertical external cavity surface emitting laser

SESAM Semiconductor saturable absorber mirror

RSAM Resonant saturable absorber mirror

CS Cavity soliton

LLS Lasing localized structure

CHAPTER 1

General Introduction

Contents

The formation of patterns from the homogeneous state of a dynamical system, also called *morphogenesis*, has been widely investigated in many areas of science spanning from biology, ecology, meteorology, chemistry and physics [Turing, 1952; Hansen, 1988; Cross, 1993; Bowman, 1998; Gollub, 1999; Sekimura, 2013; Tlidi, 2014]. Some examples are the arrangements of the dunes of sand in the desert, the rolls in sky clouds, or formation of florets in sunflowers, and even pigmentation in animals like jaguar or angelfish (see Figure 1.1).

In general, morphogenesis is a typical phenomena occurring in nonlinear *dissipative systems* far from thermodynamical equilibrium. In a scientific laboratory, where systems are under certain control, morphogenesis appears in different situations. For instance, when a fluid is under an orthogonal force of its surface, the formation of hexagonal patters is produced by Faraday instabilities [Faraday, 1831]. In biology and chemistry, reaction-diffusion systems may produce a state between bland uniformity and disorderly chaos (see figure 1.2). In 1952 the mathematician Alan Turing explained that an instability of the homogeneous state, triggered off by random disturbances leads to the formation of this patterns [Turing, 1952].

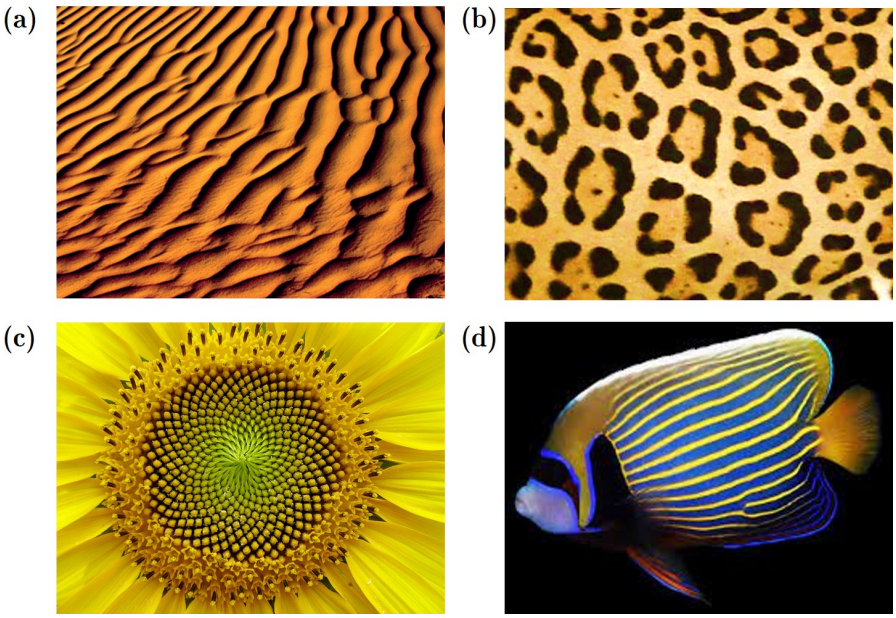

Figure 1.1. Examples of pattern structures observed in nature. (a) Stripes in dune sands, (b) Jaguar skin spots, and (c) Spiral floret formation in sunflowers [Ball, 2015]. (d) Stripes in angelfish [Kondo, 1995]

When the system is spatially extended, *i.e.* it is not ruled by its boundary conditions, its evolution stems from its symmetries and from the interplay between dissipation and non-linearity. Dissipation drives the system to evolve from an initial condition to an asymptotic state spontaneously. Nowadays this process, called self-organization, is well described by different theoretical models, for instance, reaction-diffusion model [Liehr, 2013], complex Ginzburgh-Landau equation [Stuart, 1966; Segel, 1969; Newell, 1969], Swift-Hohenberg equation [Swift, 1977] and so on.

In optics, when light is coupled with a nonlinear dissipative medium, patterns appear as a result of interaction between diffraction and nonlinearities. These patterns should not be confused with the transverse modes observed in waveguides or resonators, which are solutions imposed by the system boundaries, as the Gauss-Laguerre or the Hermite-Gauss family modes. The concept of spatial extension in optical resonators is well quantified by the Fresnel number, which corresponds to the ratio between the smallest structure generated in the transverse plane of the resonator and its transverse aperture. In a seminal paper, Arecchi and his group studied the evolution of pattern formation in a nonlinear dissipative extended system [Arecchi, 1993; Arecchi, 1995]. In this work it is shown how, by controlling the Fresnel number in a photo-refractive oscillator, the transverse emission evolves from boundaries-ruled patterns to short correlation range structures.

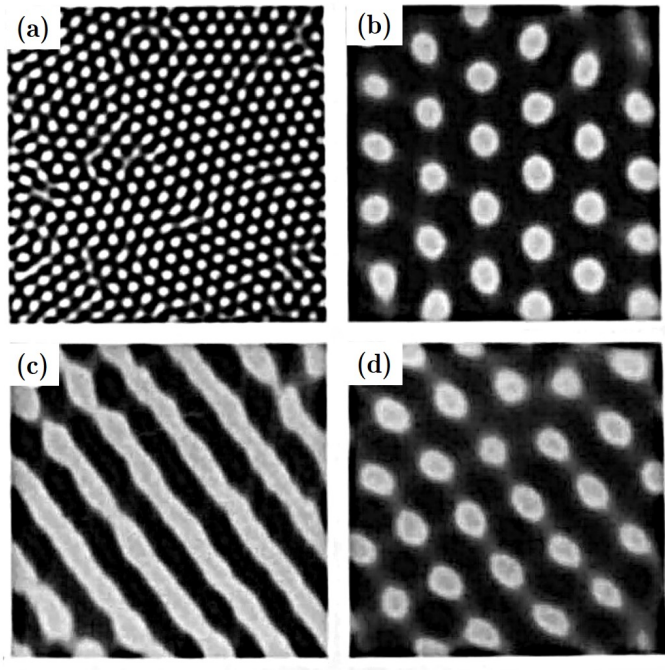

Figure 1.2. Different Turing patterns observed in polyacrylamide gel in contact with a reservoir of reagents of the chlorite-iodide-malonic acid reaction. They could appear as (a) random spots, (b) hexagons, (c) stripes and (d) a mixed state [Ouyang, 1991].

This first chapter aims to introduce the fundamental concepts of pattern formation in optical systems, and in particular, the notion of *localized structures* (LS) which are a sort of fundamental bricks of patterns. A description on how and why these structures are generated in laser devices is presented.

1.1 Morphogenesis and localized structures in optics

We can classify morphogenesis in two categories depending on the underlying mechanism. When a spatially homogeneous beam of light is injected into a nonlinear medium, diffraction and nonlinearities modify its transverse profile giving birth to patterns. This mechanism is called *passive morphogenesis*. Examples of this pattern formation have been described in sodium atomic vapors [Grynberg, 1988], and when a Kerr slice [D'Alessandro, 1991] or atomic vapors [Ackemann, 1994] are submitted to optical feedback from a mirror placed at a proper distance. On the other hand, if the nonlinear medium is active, as it would be the gain material for lasers, the pattern formation is generated from spontaneous emission noise, without any external beam [Arecchi, 1995]. Then we speak of *active morphogenesis*.

Beyond fundamental interest, pattern formation in optics has been widely investigated

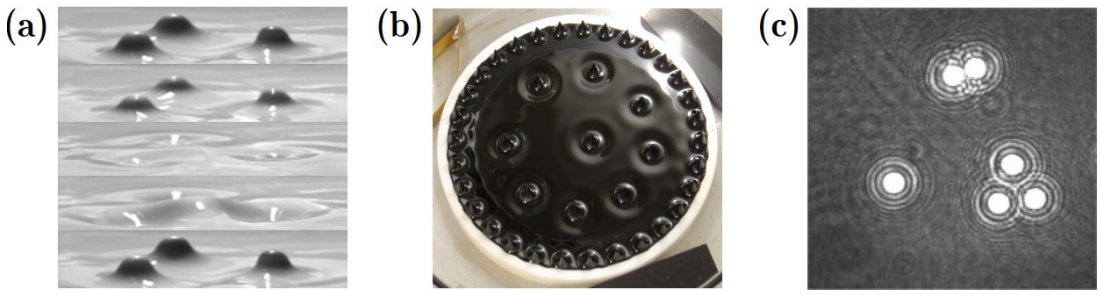

Figure 1.3. Localized structures in physical systems. (a) Colloidal suspensions under vibrations [Lioubashevski, 1999], (b) ferrofluids [Richter, 2005] and (c) liquid crystals [Ramazza, 2003].

for applications, namely in all-optical information processing. The possibility of controlling the light emitted by a passive and active optical resonator by light injected into the resonator has been discovered in the '90 and this concept paved the way towards optical transistors and information processing [Gibbs, 1985]. For example, bistability between a low intensity output and high level intensity output can be used as fundamental bits "0" and "1". Consequently, the possibility of storing information in the transverse light distribution of a resonator has attracted a lot of attention in the last 30 years. One of the major obstacles is that, when transverse boundaries determine the spatial emission, the correlation range of the intensity output in the transverse section of the resonator is almost equal to its size. In this condition, any local perturbation in the transverse plane will affect the whole transverse section. Nevertheless, in spatially extended optical resonators, a new scenario may rise, leading to structures having a correlation range much shorter than the size of the system and which are individually addressable. These structures are called *Localized Structures* (LS). We can understand them as a "piece of pattern", as one of the spots of the hexagonal pattern shown in figure 1.2 b). LS are ubiquitous in nature and they can be observed in a variety of different systems such as granular media under Faraday instabilities [Umbanhowar, 1996], vibrated colloidal suspensions [Lioubashevski, 1999], ferrofluids under magnetic fields [Richter, 2005], plasma spots in gas discharges [Astrov, 2001] and even in gaped vegetation in nature [Cisternas, 2020]. Some of these examples are shown in figure 1.3. The common property that links these systems is that the Turing instability leading to pattern formation appears subcritically [Fauve, 1990]. Moreover, stable fronts link each period of the pattern with the homogeneous solution, thus leading to a decomposition of the pattern in cellular units.

In optics, LS appear as independent peaks or holes in the intensity field, as in figure 1.3 c). Experimentally, they have been observed in liquid crystals [Ramazza, 2003],

atomic gases [Schäpers, 2000] and photo-refractive crystals [Arecchi, 1995].

The first theoretical approaches that led to the comprehension of LS on optical cavities date back to the earlies 1980's. In 1983 McLaughlin and coworkers developed simulations for studying a bistable optical cavity driven by a beam injection [Mc Laughlin, 1983]. A modulation instability appears in the parameter region of coexistence between the *on* and *off* solutions, creating a set of intensity peaks. They were interpreted as solitons circulating in the cavity perturbed by the output coupling and held by the injected beam. This system only accept two solutions, either zero solitons or full set. In terms of optical memory, that means just 2 bits of information. Years after, Firth and McDonald studied how, by introducing a modulation in the injected beam, a switching of tens of independent solitons could be obtained in the cavity [McDonald, 1990]. Another precursor study was done in parallel by Rosanov, who brought the concept of *diffractive autosolitons* for an optical bistable cavity [Rosanov, 1990]. Due to diffraction, a switching wave present ripples in its tails and this oscillation can lock a second switching wave. Hence, the velocity of the fronts becomes zero even if the parameters of the system are not exactly at the Maxwell point. That is, the two fronts can be auto trapped and generate a new one, whose width depends on the period of the initial ripples, *i.e.* an autosoliton. In 1993, Tlidi and Mandel predict the existence of stable LS using the Swift-Hohenberg equation in the frame of optical bistability and the weak dispersion limit [Tlidi, 1994]. After, in 1996 Firth predicts LS states for a saturable absorber in an optical cavity [Firth, 1996].

To summarize, localized structures are solutions of nonlinear extended systems kept far from equilibrium. They are characterized by a correlation range much shorter than the size of the system. That is, they are independent of the boundaries. The works of McDonald and Rosanov started to include the terminology of *soliton* for some of their dissipative structures. So, I would like to take a small step back to explain what we mean as solitons in optics, and why this terminology has been used to indicate dissipative localized structures. The study of solitary waves started years before in conservative (also known as Hamiltonian) systems. Light propagation in a nonlinear medium that can be self-focused (or defocused), was already described and understood with the nonlinear Schrödinger equation (NLS)

$$i\frac{\partial E}{\partial t} + \frac{1}{2}\Delta_\perp E + \mathcal{F}(|E|^2)E = 0, \tag{1.1}$$

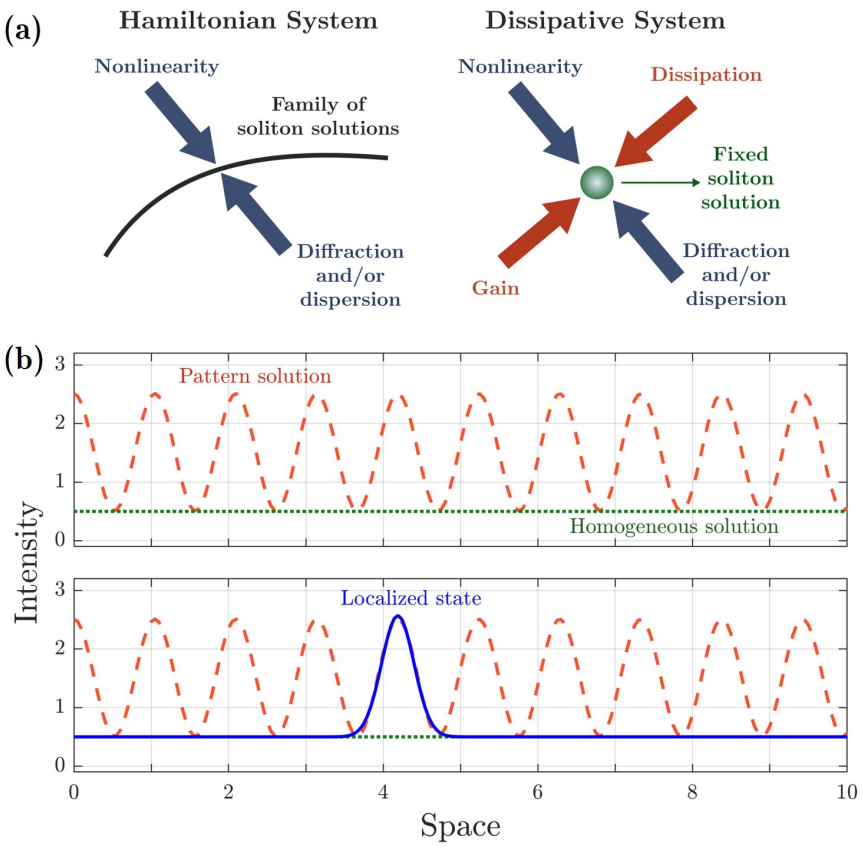

Figure 1.4. (a) Schematic differences of the solitonic solutions in conservative and dissipative systems [Grelu, 2012]. (b) Representation of how a localized state appears as the connection between an homogeneous solution and a patterned one in a bistable system.

where E is the scalar electric field, $\Delta_\perp$ the transverse laplacian, and $\mathcal{F}$ is a function of the intensity $|E|^2$. The formation of solitons is possible when the diffraction and/or dispersion balance the nonlinearities. It has been shown that this system is integrable using the inverse scattering method, finding an infinity of conserved quantities when $\mathcal{F} = |E|^2$ [Gardner, 1967]. There is a family of solutions, and if the initial condition allows the balance between nonlinearity and diffraction and/or dispersion, a soliton solution could be achieved (figure 1.4 a)).

LS are also found in equations that turns out to be similar to NLS equation, but which includes the terms of losses and energy injection resulting from the coupling of the light field with the resonator material. Because of that, in some cases, LS are also known as *dissipative solitons*. This is only valid when the dissipation acts just as a weak perturbation. For instance, Lugiato-Lafever (LLE) equation, that describes a nonlinear passive cavity driven by a coherent plane wave [Lugiato, 1987]. This equation is,

$$i\frac{\partial E}{\partial t} + \frac{1}{2}\Delta_\perp E + |E|^2 E = i(-E + E_{inj} - i\theta E), \tag{1.2}$$

where the first part is the NLS equation, and the three following terms are the cavity losses, the driving field E_{inj} and the cavity mistuning θ.

Even with these similarities in the mathematical models, there are some differences between conservative and dissipative solitons. In contrast with the NLS, the LLE and other models for dissipative systems are not in general integrable. LS are *rigid*, in the sense their characteristics are fixed by the system parameters and not by the initial condition. This is a result not only of the nonlinearities and diffraction and/or dispersion compensation, but also a balance between loss and energy injected (figure 1.4 a)) [Fauve, 1990; Grelu, 2012].

Moreover, LS appear when the system is multistable. The simples situation is pictured by a homogeneous state coexisting with a patterned one (figure 1.4 b) up). Then, stable fronts, making a connection between the homogeneous state and the pattern states appear. This is pictured in the blue profile in figure 1.4 b) down for the case of one stable front, and corresponds to a single LS. Due to this multistability, several scenarios may occur, with different number of LS. In addition, it has been shown that these LS may interact each other forming clusters or molecules [Coullet, 2000].

Most important, LS are attractors of the system. If a local perturbation creates one of them, this LS persists even when the perturbation is gone, and will stay until another perturbation switch it off. This *on* and *off* states make them suitable for application as bits of information.

In general LS could appear in systems where dissipation is not only a perturbation, but the dominant factor compensated by the external energy supplied. Then, the look for a master equation results impossible, since scenarios and system they arise from could be totally of different origin.

As we will see in the following sections, our interest will focus on optical semiconductor resonators, where spatial LS have been widely studied and observed in [Barland, 2002]. Several important applications of LS have been demonstrated in these devices as their use for optical memory [Pedaci, 2006], semiconductor layers microscopy [Pedaci, 2008b] and delay line [Pedaci, 2008a].

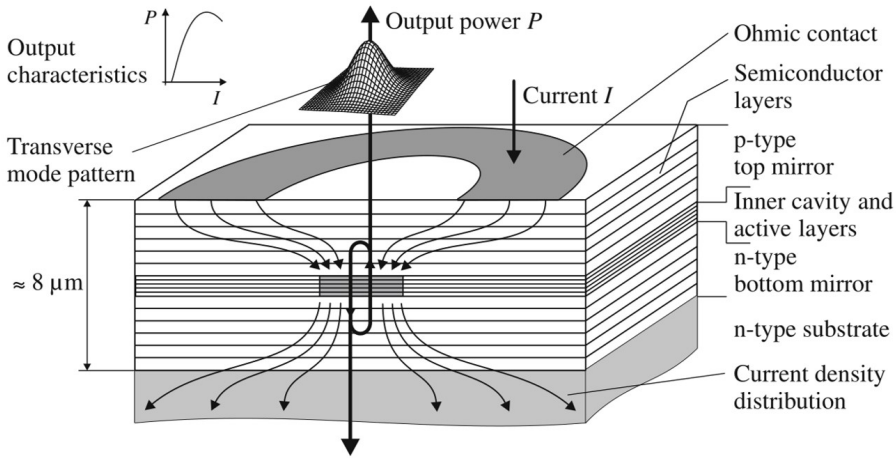

Figure 1.5. Function scheme of an electrically pump VCSEL structure. [Michalzik, 2013]

1.2 Localized structures in semiconductor cavities

The requirement of large aspect-ratio for the existence of LS is difficult to be fulfilled in real systems because this condition require short cavities and wide transverse resonant size. While the former implies a small amount of gain available in a single pass, the latter implies a high level of losses. Vertical cavity surface emitting lasers (VCSEL) allow to overcome most of these difficulties.

VCSELs are one of the most used semiconductor laser sources since their prediction and invention in the late 1970s by Kenichi Iga [Iga, 1988; Iga, 2000]. In the decade of 1980s the first continuous wave (CW) operation was demonstrated with a GaAs based source, combining metal and dielectric mirrors. Years after, a full monolithic electrically pumped InGaAs-GaAs VCSEL was created, incorporating epitaxial distributed Bragg reflectors (DBR) enclosing the active medium. A typical scheme of this VCSEL is presented in figure 1.5. In this case the operation wavelength was about 960 nm with a current threshold close to 1.3 mA [Jewell, 1989]. The success of these devices comes from a combination of unique properties, mainly focused on optical data transmission. For example, their low current threshold, below 1 mA, minimize the energy consumption for electronic circuits. They present good digital modulation behavior for data rates, allowing to reach tens of GHz. On top of that, because of their high power efficiency, more than 50%, thermal menagement is easy to handle.

Because of their reduced longitudinal length, usually few microns, they operate in single longitudinal mode. Moreover, their fabrication allows to achieve transverse dimensions of hundreds of microns. Then, VCSELs can reach unprecedented large Fresnel number in the history of lasers.

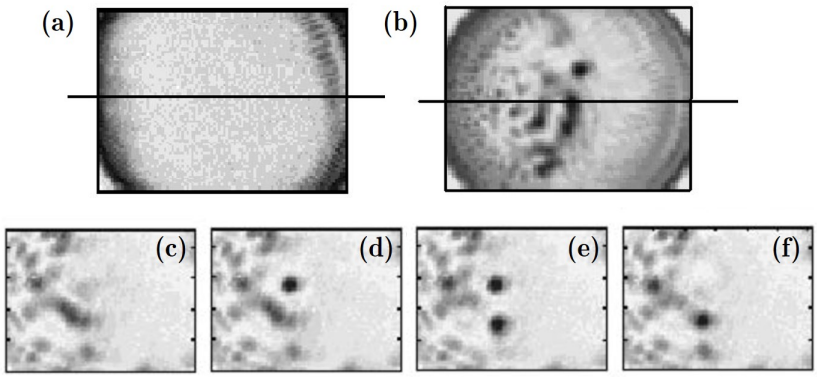

Figure 1.6. Panels (a) and (b) show the transition between the homogeneous emission and a pattern state after a coherent holding beam is injected. (c)-(d) shows multiple scenarios before and after the perturbation beam writes or erase one spot [Barland, 2002].

This characteristic of VCSEL led to the first observation of spatial localized structures (SLS) in an optical cavity [Barland, 2002]. This was realized by using an electrically pumped VCSEL of 150 μm area operated as an amplifier, i.e. pumped above transparency. The VCSEL was injected by a coherent and spatially homogeneous holding beam. For properly chosen parameters of this beam (intensity and detuning with respect the cavity resonance), the VCSEL exhibited bistable response between an off state and a state with bright spots of around 10 μm in the transverse plane, as shown in Figure 1.6 a)-b). These spots could be individually addressed by shining small-size beam pulses in the transverse plane. Switching on or off procedure was realized by changing the phase relationship between the perturbation beam and the holding beam (see Figures 1.6 c)-f)). These SLS observed in an injected resonator were named *cavity solitons* (CS). In 2006, the control of the writing position was obtained by introducing a phase mask in the holding beam, creating an array formation of CSs [Pedaci, 2006]. Furthermore, the same authors studied the possibility to drift the position of one pixel by using a gradient line of phase in the holding beam [Pedaci, 2008a]. An important remark in this system is that the position and appearance of LS are affected by inhomogeneities in the transverse section of the VCSEL appearing during the device growth process. These inhomogeneities are sudden variations of the optical length of the resonator and they affect locally the cavity resonance. These defects have been used as a source of drifting CS along an specific direction when the holding beam had a phase gradient [Caboche, 2009a; Caboche, 2009b].

Cavity solitons rely on the coupling between the holding beam and the nonlinear amplifier, hence they appear in the context of passive morphogenesis. In 2008 when

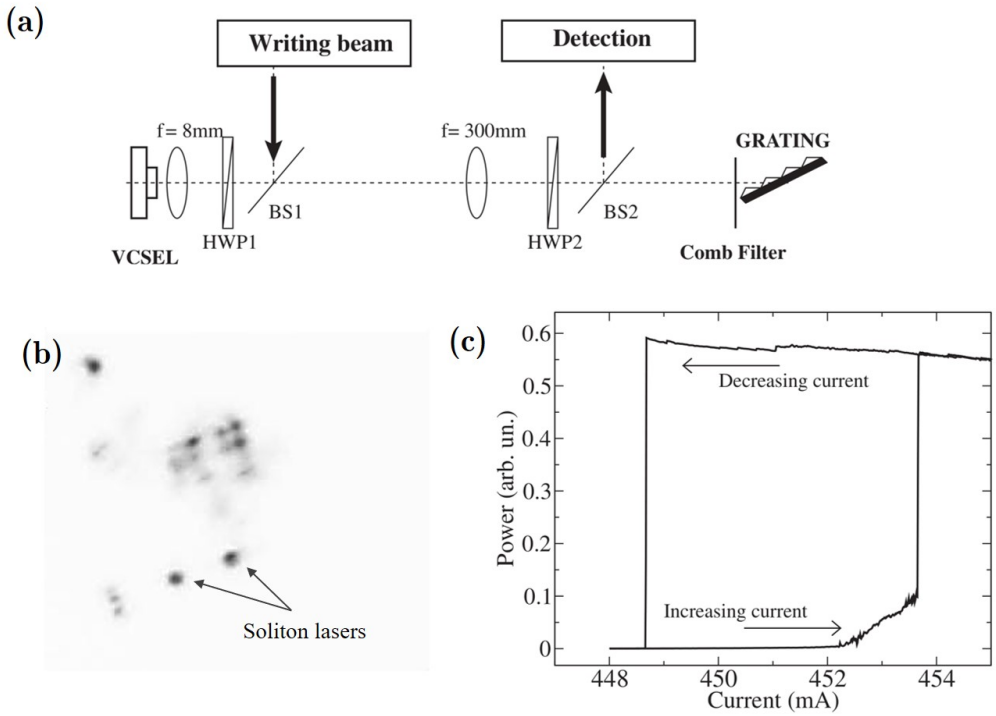

Figure 1.7. (a) Experimental setup, where a VCSEL is coupled with an external cavity to a grating. (b) VCSEL facet showing the appearance of independent light spots of 10 μm. (c) Bistability regime of one of them, showing its abrupt generation and annihilation [Tanguy, 2008]

Tanguy and collaborators developed the first experiment for generate CSs in a laser system, getting rid of the holding beam and assessing the existence of SLS also in the context of active morphogenesis. To mark the difference with CS, these SLS were called *laser solitons*. They coupled a 200 μm area VCSEL to a frequency-selecting element in external cavity configuration [Tanguy, 2008]. The cavity was composed by two lenses and by a holographic grating in Littrow configuration, as it is shown in the scheme of figure 1.7 a). The positions of the lenses were chosen for achieving the *self-imaging* condition, that is, the VCSEL surface was projected onto the grating and imaged back. This allows to prevent losses due to diffraction and fulfill the high Fresnel number condition. The frequency of maximal feedback of the grating was set to be red-detuning with respect to the longitudinal resonance frequency of the VCSEL, when it is pumped below threshold. By increasing the injection current several spots of the same spatial dimensions, around 10 μm appeared (1.7b). Bistability of each of them was observed, depending on the current value. Their appearance was sudden under a critical current injection, so they can be switched on and off independently. This bistability is shown in 1.7c. Each one of these spots can be understood as a single tiny single longitudinal mode laser with emission line-width of 10 MHz. In this experiment, the origin of

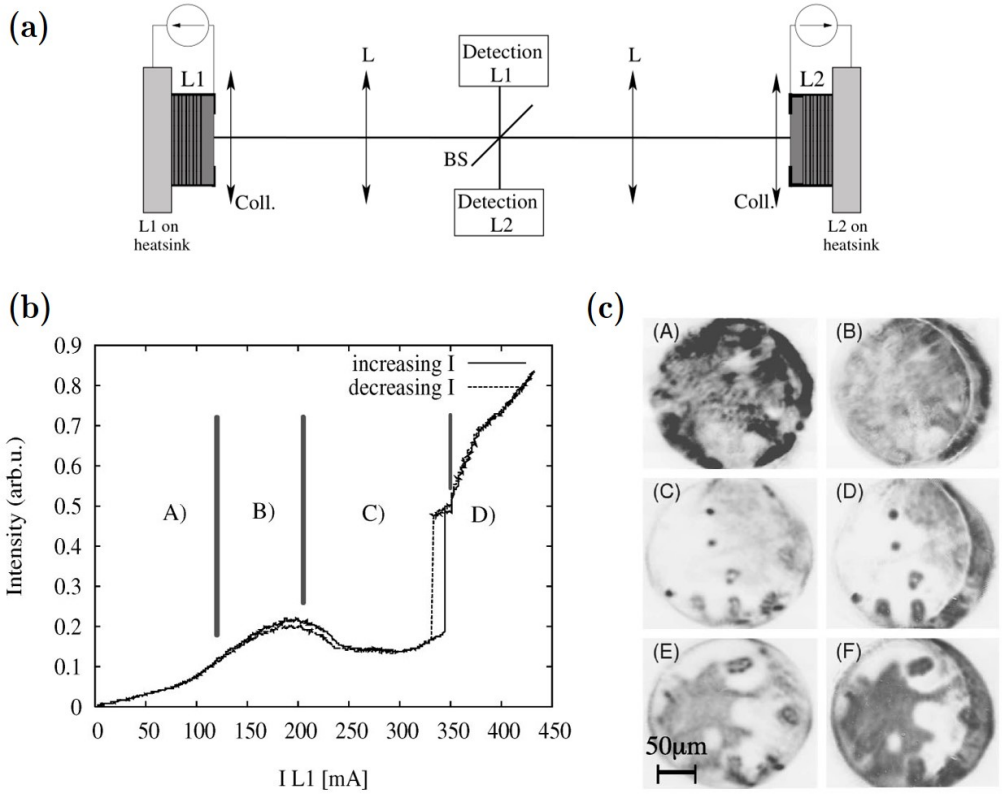

Figure 1.8. (a) Cavity setup, formed by two VCSEL's, L1 used as an amplifier and L2 as an absorber. (b) Intensity output when incrementing the current injection of L1, with markers (A) below threshold, (B) lasing with the feedback, (C) absorption of L2 where bistability appears, and (D) pattern formation. In (c) it is shown the transverse profiles of the intensity evolution described [Genevet, 2008].

bistability comes from the phase-amplitude coupling [Henry, 1982], generating different frequencies for the lasing and non-lasing states.

In the same year, another scheme for laser solitons was proposed. It is based onto the coupling between two broad-area VCSELs resonators, one operated as amplifier (L_1) the second as saturable absorber (L_2) [Genevet, 2008]. The two devices delimit a 4-lenses cavity (see figure 1.8 a)). Again, the self-imaging condition is imposed in order to achieve the high aspect-ratio of the system. The lasers are thermally controlled for detuning at a proper value the cavity resonance of L1 with respect the one of L2 when no current was injected in both VCSELs. By increasing the current of L1, due to Joule heating, the frequency of the laser grows linearly. At a critical value of current (200 mA), both laser frequencies match and absorption in L2 takes place. A decrease of the output intensity can be observed in region C of figure 1.8 b). In this regime a sudden transition from low to high intensity due to saturation of L_2 appears, and corresponds to the emergence of bistable spots in the transverse plane (figures 1.8 c) C-D). Finally, when

the pump increase even more, around 350 mA, the spots start to filament and connect through a pattern-like structure that starts covering the whole transverse area (figures 1.8 c) E-F). For demonstrating that the spots in the bistable regime are LSs, a writing beam of 15 μm has been used for turn them on and off, similarly to the procedure described before for CSs. Since these LSs are not generated by a holding beam, they do not share a common phase, as shown in an interferometric analysis [Genevet, 2010].

The experiment of Genevet unveiled the possibility of generate LS by exploiting a resonant absorber. This system is very interesting from the dynamical point of view because it has been widely used to implement passive mode-locking, a regime leading to short pulses. Hence, it paved the way to spatial localized lasers which emit pulse trains. More exciting perspectives have risen when, as described in the following section, the idea of temporal localized structures appeared.

1.3 Temporal localized structures

Conservative temporal solitons have been widely studied in the frame of NLS which described pulse propagation in a nonlinear fiber. The balance between group-velocity dispersion (GDV) and self-phase modulation (SPM) due to Kerr nonlinearity, allows the creation of a temporal soliton [Kivshar, 2003]. In dissipative systems, as in resonators, it has been shown that a pulsating emission can be generated through a modulational instability [Haelterman, 1992]. For many years the question of whether the concept of LS can be extended or not to the time domain has been addressed. In optical resonators, the notion of extended system has to be reformulated. While for spatial localized structures (SLS) the relevant size of the system is the transverse section of the resonator, for temporal localized structures (TLS) the critical size is the resonator length. More precisely, the temporal equivalent of large aspect-ratio reads that the cavity round-trip must be much larger than the bulk system timescales τ_m, which, somehow, fix the width of the smallest temporal structure that the system can generate. Accordingly, the high aspect-ratio condition in the time domain may be reformulated as $\tau_m \ll \tau_c$.

The first experimental observation of a TLS was done by Leo and coworkers by using a Kerr medium, *i.e.* exploiting an instantaneously responding medium ($\tau_m \to 0$) [Leo, 2010]. They used a silica fiber cavity of 1.85 μs round-trip, driven by a CW beam (see Figure 1.9 a)). The fiber, due to Kerr effect, exhibits bistability between a stationary background emission and an upper branch modulationally unstable due to the interplay

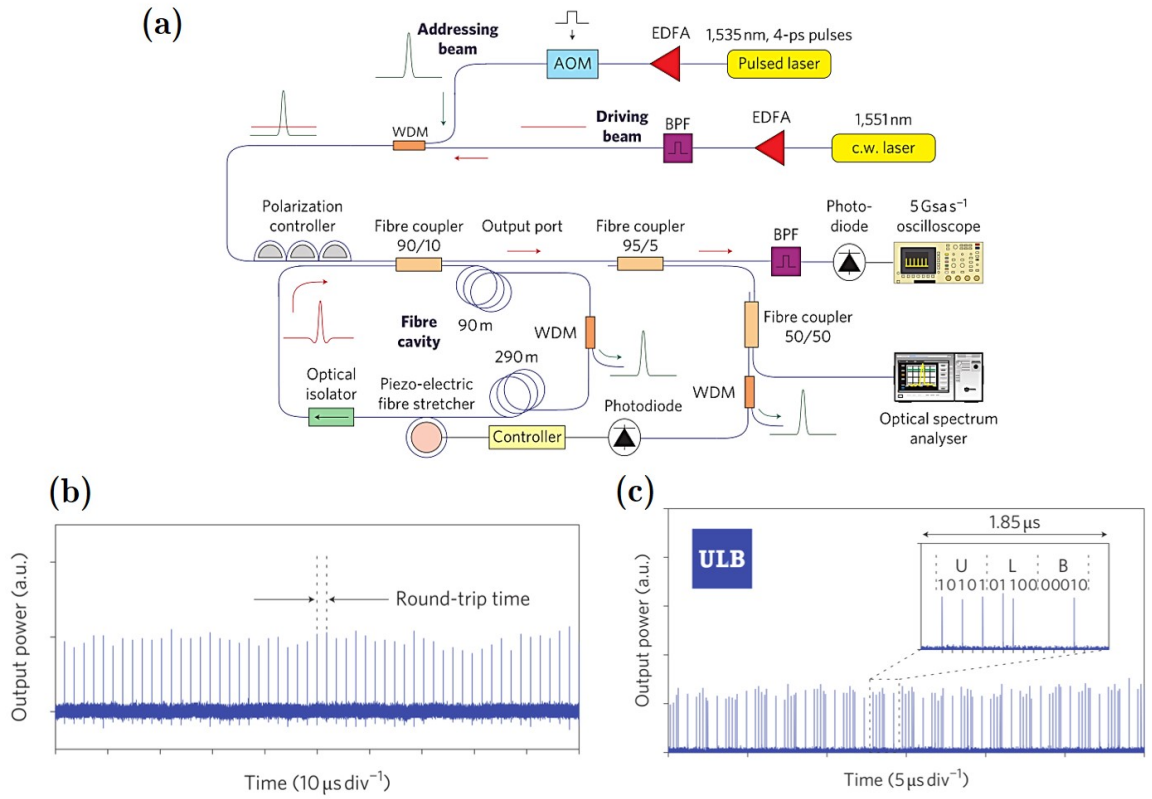

Figure 1.9. (a) Set up used for generating TLS in a Kerr fiber resonator. (b) Temporal trace of the fundamental solution. (c) Example of an all-optical buffer, where the pulses were used as bits of information [Leo, 2010].

between the GVD and the Kerr effect. This instability leads to a pulsating state which can be considered as the equivalent, in the time domain, of the pattern state underlying to SLS. Accordingly, each pulse forming the pulsating solution can be individually addressed exactly as each element of the pattern could be addressed in the spatial case. When a writing pulse laser of 4-ps pulses is sent with a repetition rate equal to the free spectral range (FSR) of the cavity, it generates a pulse which keeps traveling back and forth in the fiber resonator, even after the perturbation is removed (1.9b). Furthermore, when a pattern of addressing pulses is sent to the cavity, a corresponding pattern of TLS is created in the cavity. Accordingly, as shown in figure 1.9 c), they were able to store in the cavity a bit stream encoding the name of the university. This was a clear demonstration of all-optical buffer operation based on TLS. Besides the similarities with SLS, one striking difference is that TLS are immune to material inhomogeneities, which results in great advantage when storing information. As a last remark, the localized state in this experiment came out from passive morphogenesis: the driving beam was responsible for the persistence of the pulse. Then, as for SLS, on may wonder if TLS can be obtained in the context of active morphogenesis *i.e.* in a laser system. This will be the

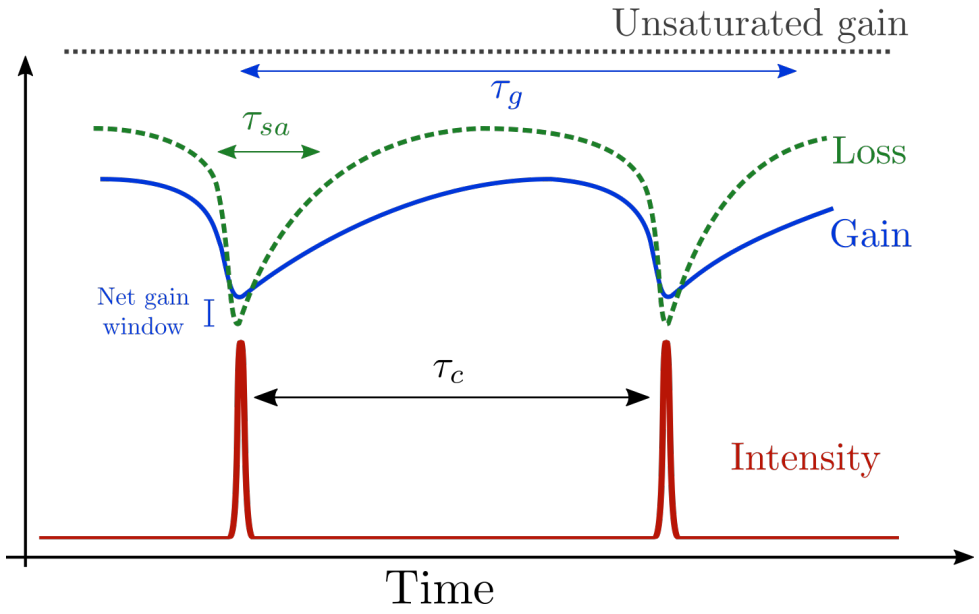

Figure 1.10. Gain and loss evolution during fundamental passive mode-locking mechanism (top) for a pulse generation (bottom).

matter of the next section.

1.3.1 Temporally LS in semiconductor lasers

Mode-locking in lasers is a very well known process for the generation of ultra short, high intensity pulses at a repetition rate corresponding to the cavity free spectral range [Ippen, 1994; Haus, 2000]. In particular, semiconductor mode-locked lasers have attracted attention due to their compact size and large repetition rate. Mode-locking can be obtained in an active or passive way. The first one is due to the modulation of an external parameter, at a frequency resonant with the separation between modes. For ultra-fast speed; the precision required is not easy to achieve, resulting then in a disadvantage. On the contrary, for *passive mode-locking* (PML) this external modulation is not required. Instead, mode-locking can be obtained by coupling a laser amplifier with an intracavity saturable absorber, which via modulation of losses favors a pulse emission against a CW operation [Tropper, 2004; Keller, 2006].

Figure 1.10 depicts the dynamics of gain, losses and intensity in a stable passive mode-locking regime. Between two consecutive pulses, the losses are larger than the gain which is recovering to a level of positive net gain. When eventually this occurs, losses decrease suddenly due to the saturation of the absorber and a pulse is emitted. Hence, the gain (blue curve) suffers a depletion and its recovery starts again [Paschotta, 2002; Lorenser, 2004]. The situation described in Fig.1.10 requires that saturable absorber recovery time is faster than the gain recovery time$\tau_{SA} < \tau_c$ for pulse shaping and that

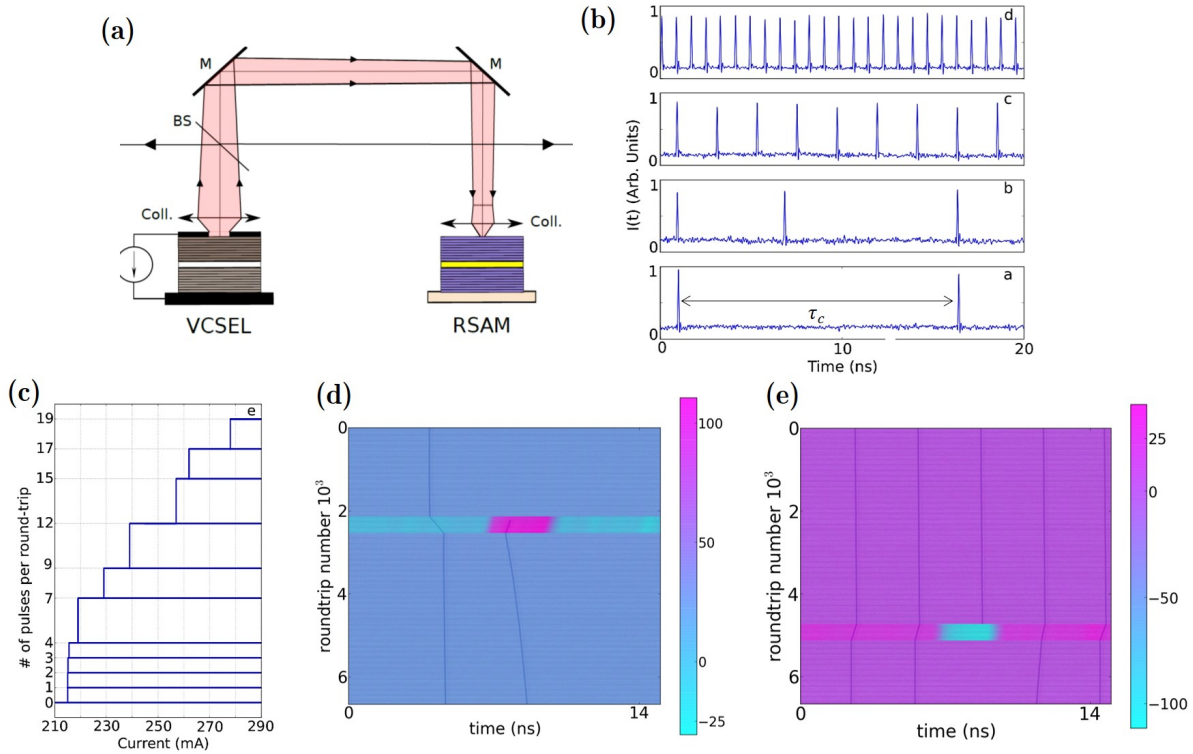

Figure 1.11. (a) Experimental setup: VECSEL and SESAM thermally stabilized, BS: output coupling beam splitters, M: mirrors, and Coll: aspheric lenses. (b) Different number of pulses for the same parameters of the system, revealing multiestability. (c) Staircase in terms N when changing the the current injection of the VCSEL [Marconi, 2014a]. Spatio temporal diagrams when a LS pulse (black lines) is (d) turned on and (e) off, via an electrical perturbation (colormap) [Camelin, 2016]

.

the cavity round-trip τ_c is shorter than the gain recovery time for avoiding the emission of another pulse in the cavity, which may destabilize the pulse emission. In conclusion, the condition

$$\tau_{SA} < \tau_c < \tau_g, \tag{1.3}$$

is necessary for the stabilization of the pulse train. Another important condition for mode-lock stability is that the ratio between saturation fluence of the gain medium over the one of the absorber should be larger than one.

In 2014 Marconi and coworkers demonstrate, experimentally and theoretically, that a VCSEL coupled to a resonant saturable absorber (RSAM) in an external cavity configuration, could lead to the generation of temporal LS in the limit of long cavity, thus fulfilling the condition for large temporal aspect-ratio

$$\tau_{SA} < \tau_g < \tau_c. \tag{1.4}$$

They show that, when the saturable absorber modulation depth is above a critical value, pulse emission occurs below the laser threshold.[1] In this condition several passive mode-locking solutions with different number of pulses per round-trip and different arrangement coexist in the parameter space together with the off solution. This general multi-stability in the time domain reminds of the general multi-stability of different patterns which underlies the formation of spatial LS. In this situation, passive mode-locking pulses become localized, *i.e.* they can be individually addressed [Marconi, 2014b; Marconi, 2015a].

Multistability was observed in terms of the number of pulses N inside the cavity. In Figure 1.11 b) different solutions coexisting all together with the off solution are shown. In panel c, the bifurcation diagrams of these pulsing states is disclosed as a function of the pumping current of the laser.

These experimental evidences, showing temporal TLS in a VCSEL coupled to a large contrast SESAM, added up to the results of Genevet showing existence of SLS in two broad-area VCSELs coupled, one operated as gain medium, the second one operated as saturable absorber. These results pave the way toward the realization of a laser devices capable of hosting spatio-temporal LS, also called dissipative light-bullets.

While in Genevet's set up temporal localization was impossible to reach because the timescales of the absorber and of the gain medium were too close and no stable mode-locking could be achieved, in Marconi's setup the fluences ratio between the VCSEL and the SESAM was not allowing stable passive mode-locking in self-imaging external cavity. These problems may be solved by using properly designed Vertical External-Cavity Surface-Emitting Lasers (VECSEL). These devices consist of a gain mirror (also called 1/2 VCSEL) coupled to an external cavity closed by a SESAM. They are typically operated in the passive mode-locking regime to generate pulses [Garnache, 2002] and the two media can be possibly designed properly for working in a self-imaging external-cavity.

1.3.2 Towards spatio-temporal localized states

Spatio-temporal solitons are a sort of *holy grail* for nonlinear optics since its origins. They are also called optical light bullets (LB), mainly because light is confined in both the three dimensions of space as well as in the time domain. It is well known that in conservative Kerr media they are unstable for higher cases than (1+1)D and collapse [Kuznetsov, 1986],

[1] Laser threshold is meant as the pumping level at which the off solution becomes unstable.

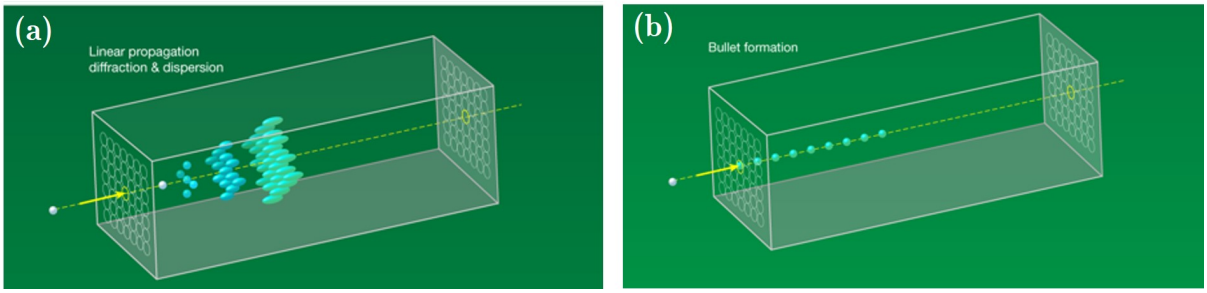

Figure 1.12. Minardi's experimental spatioemporal images for (a) low and (b) high input power of the injected beam. The creation of a single light bullet appears in the latter scenario [Minardi, 2010].

unless a saturation of the nonlinearity allows their stability [Edmundson, 1992]. However, they have been predicted and observed in quadratic nonlinear media ($\chi^{(2)}$) in the case (1+1)D [Liu, 1999]. Almost a decade after the first observation of 3D conservative light bullets was done by Minardi and coworkers [Minardi, 2010]. They used an hexagonal array of evanescent coupled single mode fiber, excited by a femtosecond pulse in the center. At low input power, light spreads to the neighboring waveguides and becomes broad due to anomalous dispersion (figure 1.12 a)). For higher values of the injected beam the light becomes localized in the original waveguide, as it is represented in figure 1.12 b). Noteworthy, the propagation distance of the bullet was just of few millimeters. This fact reduces possibilities for application such as telecommunications. So far, this is the only evidence of three dimensional light bullets.

On the other hand, dissipative systems are promising candidates for finding Light Bullets. Dissipative spatio-temporal localized states will gather all the properties of the spatial and temporal LS. They will be individually addressable pulses also localized in the transverse plane of the laser resonator. This could lead to a three dimensional buffering of data inside the cavity. If the transverse section allows creating an array of $N \times N$ spatial LS, and the longitudinal cavity allows storing M TLS, one may handle $M \times N^2$ bits in a single device using LB as bits of information 1.13. Semiconductor laser resonators are promising systems since spatial and temporal LS have been already obtained.

In 2017 Gustave and coworkers managed to mode-lock spatial localized structures in a VCSEL with frequency selective feedback [Gustave, 2017]. This experiment is similar as Tanguy's described in the previous sections. They show that a spatial LS, via amplitude modulation of its whole profile can generate a mode-locked sinusoidal signal. Figure 1.14 a)) shows the temporal traces at different time scales in the presence of one pulse per round-trip. Its corresponding spatio-temporal map is presented in panel b) with the

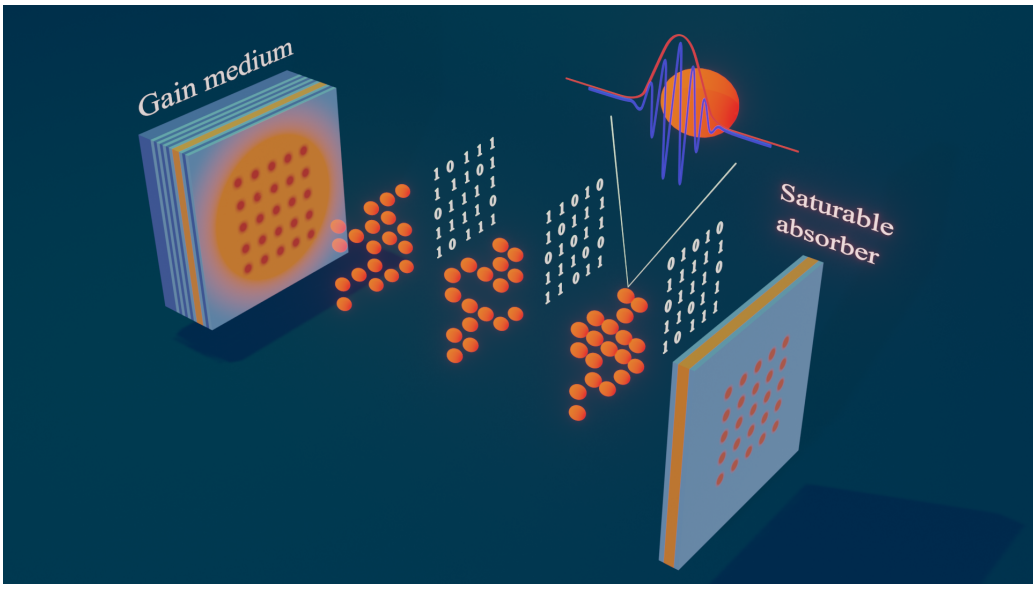

Figure 1.13. Scheme of a gain medium and saturbale absorber coupling, operated as an all-optical buffer of $M \times N^2$ bits of information using light bullets .

near field profile plotted in the inset. The last panel, c, shows the RF spectrum of the emission, revealing the peak at the FSR of the cavity. Their simulations show that the stabilization of the pulse solution was only for a short cavity. For $\tau_c > 1$ ns the dynamics became irregular. The addressing of these temporal SLS was not performed, mainly due to the experimental difficulties in perturbing the system at the cavity round-trip time. Noteworthy, this striking experiment paves the path to the possible existence of LB.

From the theoretical point of view, few years ago, researchers of Universitat des les Illes Balears (UIB) and Münster University, developed a model analyzing the effect of diffraction operator for the same set of equations that describe the formation of TLS in passive mode-locking obtained by Marconi [Javaloyes, 2016a; Gurevich, 2017]. Such model is a generalization of Haus partial differential equation (PDE), coupled to the carrier's diffusion of the gain and saturable mediums. They show the existence of stable 3D LB that can be individually addressed by an optical pulse perturbation in the cavity.

1.4 Motivation and contents of the thesis

This thesis is an experimental study of spatio-temporal phenomena in VECSELs, conceived for gathering both conditions for temporal and spatial localization. The experiments developed during my PhD were done at INPHYNI in Valbonne, under the supervision of Prof. Massimo Giudici. This work was funded by a French ANR project called BLASON (*Balles de lumiere dans les lasers a semiconducteurs*) in collaboration with

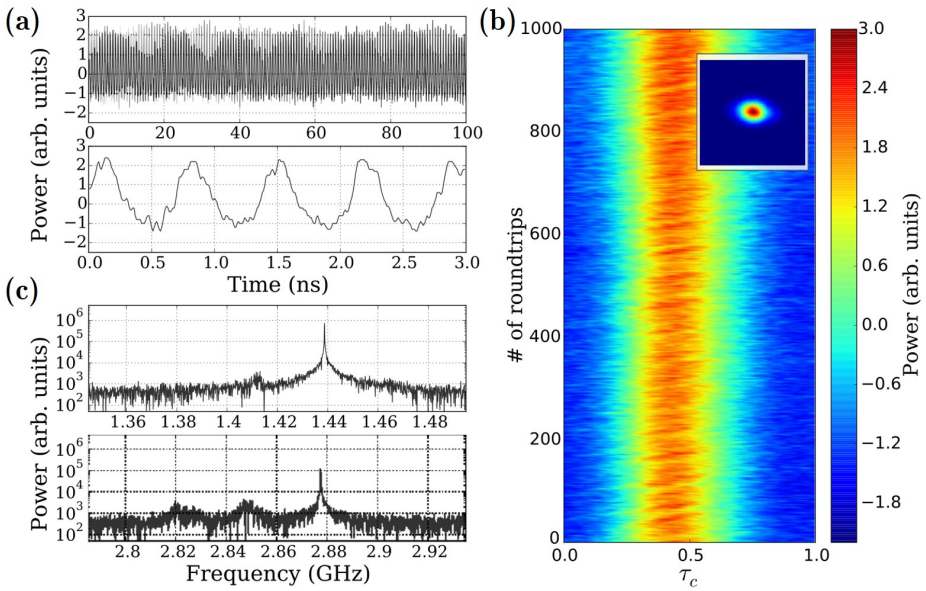

Figure 1.14. Experimental observation of a one pulsed mode-locked SLS. (a) Temporal traces with different time scales and (b) its corresponding spatio-temporal map. (c) RF spectrum showing these pulses have the same repetition rate as the cavity round-trip [Gustave, 2017].

the group at Institute d'Electronique et Systèmes (IES) from l'Université de Montpellier, the theoretical groups of the Universitat de les Illes Balears (UIB) in Spain and University of Münster in Germany, and the Centre de Nanosciences et de Nanotechnologies (C2N) in Paris.

In Chapter 2 we will discuss why VECSELs devices are a source of choice for the generation of spatial and temporal LS when the external cavity is closed by a SESAM. The main ingredients of a VECSEL for achieving LS are presented, taking account the gain and absorber characteristics, the external cavity and its optical components, as well as the optical pump. A study using the $ABCD$ matrix formalism for a 4-lenses self-imaging cavity is performed, and it unveils the importance of the thermal lens f_{th} effects induced by the pump on the self-imaging condition (SIC). The effects of this spurious lens need to be compensated by shifting the positions of some optical elements inside the cavity with respect to the positions calculated for obtaining SIC in the case of the cold cavity. The real optical elements parameters in terms of numerical aperture and aberrations are taken into account by using ZEMAX software analysis with the data provided by the manufacturer. The impact of these parameters on SIC is analyzed through this tool which gives hints for optimizing the cavity design and enables the characterization of its performances.

In Chapter 3 we show how a self-imaging external cavity VECSEL can be experimen-

tally obtained and how this condition can be verified. We describe the spatio-temporal emission obtained in this regime and how it depends on the elements of the round-trip propagation $ABCD$ matrix. Close to SIC spatial structures appearing are not self-transformed in the sense they do not present homothetic near field and far field. In addition, when the gain and absorption resonances are properly tuned, temporal localized emission is achieved. Hence, in the time domain, the spatial structures observed correspond to picosecond pulses which can be individually addressed: they are temporally localized patterns. In each situation the entire pattern is pulsating synchronously, and all the points of the near-field profile are correlated.

In Chapter 4 we study the manipulation of these TLS using optical feedback. An independent external cavity was set to send back the pulsating solution onto the gain mirror with a variable delay. The feedback arm τ_f was set to be close to a fraction τ_c/n. If the feedback delay is tuned slightly before the τ_c/n, the solution loss its stability and can jump to another branch with different number of pulses. On the contrary, when feedback delay is set after, the corresponding solution is reinforced and not affected. These experimental results were theoretically proven with the collaboration of UIB and Münster University.

The last Chapter presents a first step towards spatio-temporal decorrelation in our VECSEL. Even if the system does not emit in a decorrelated way spontaneously, we have induced it by overlapping to the main pump small pump beams that create hot spots on the section of the gain mirror. By controlling the gain level on each of these hot spots, we have induced gain-pinned temporally-localized pattern which are pulsing asynchronously. These hot spots have been also engineered directly onto the top facet of the gain mirror through deposition of Chromium absorptive mask. Accordingly, we have realized a proof of principle for the realization of multiplexed sources of TLS patterns into the same VECSEL.

CHAPTER 2

VECSEL as a source for localized structures

Contents

2.1 Introduction

My thesis work is devoted to the implementation of spatio-temporal localized structures (LSs) in a semiconductor laser. As described in Chapter 1 the results of [Genevet, 2008] and [Marconi, 2014a] were obtained in similar experimental schemes, namely a VCSEL coupled to a distant saturable absorber reflector. Nevertheless, as we have illustrated, the required conditions for stable passive mode-locking in a self-imaging cavity configuration, which is required for achieving spatial LS, were lacking both systems. In the former setup, where two identical VCSELs were used as gain section and saturable absorber, the time scale requirement between the recovery time of the

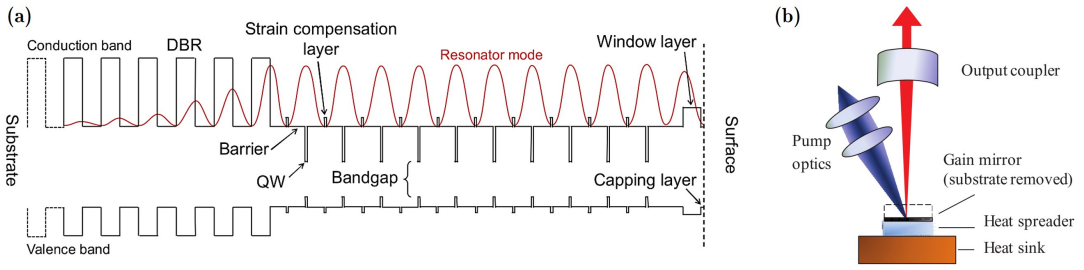

Figure 2.1. (a) 1/2 VCSEL structure. (b) Plano-concave VECSEL [Guina, 2017].

saturable absorber τ_{SA} and the gain τ_g: $\tau_{SA} < \tau_g$ was not matched. In the latter setup, the use of a VCSEL as a gain section was preventing to match the condition on saturation fluence ratio between the gain (F_g) and the absorber (F_s): $f_g/F_s > 1$. In order to solve these problems, the only solution is to design and to realize a laser device tailored for matching all the requirements for hosting spatio-temporal LS. This device is an optically-pumped Vertical External Cavity Surface Emitting Laser (VECSEL) where the gain mirror (also called 1/2 VCSEL) and the Semiconductor Saturable Absorber Mirror (SESAM) delimiting the external cavity have been developed in collaboration with the Institut d'Electronique et des Systèmes of Montpellier and realized by the technological facility Renatech at Centre de Nanosciences et de Nanotechnologies de Paris.

VECSELs have demonstrated their potential since the earlies 1990s as a high CW output power source, taking advantage of the external cavity and optical pumping techniques [Le, 1991; Kuznetsov, 1997; Lutgen, 2003; Chomet, 2018]. They can present a near diffraction limited low divergence circular beam quality, which has not been observed in any other type of waveguide semiconductor source. Nowadays they are relevant for several applications, such as intra-cavity frequency doubling [Jacquemet, 2007], tunable single-frequency ultra-low noise operation in the near and far infrared ranges [Laurain, 2010; Laurain, 2010; Ouvrard, 2005; Triki, 2008; Cocquelin, 2009], low noise dual-frequency operation for metrology, remote sensing, and communications applications [Baili, 2009; Mignot, 2009], gyrolaser operation for avionic/space and high sensitivity laser spectroscopy for gas analysis [Cermak, 2010]. VECSELs are usually optically pumped by a laser diode and closed by a concave mirror (see figure 2.1). Such configuration is always stable, and with the use of a SESAM, PML pulses can be achieved. This combination is nowadays one of the most versatile laser sources for ultrashort pulse operation, low noise, high output power, high brightness and compact form factor [Tropper, 2004; Guina, 2017].

In this chapter we aim to present the requirements a VECSEL should fulfill for the

appearance of LS, based on the previous experiments and theoretical models. These requirements span from the structure of the devices to the design of the external cavity. This latter is analyzed using the $ABCD$ matrix formalism, for understanding the stability of solutions for the fundamental Gaussian beam and for assessing self-imaging condition (SIC). Finally, ZEMAX calculations have been performed for cavity optimization in relation with the real parameters of the optical elements.

2.2 VECSEL design

On the base of the results described in Chapter 1, we have established a road map for the design and realization of a VECSEL capable of hosting spatio-temporal LS.

- ***Best spatial homogeneities in chip devices.*** Inhomogeneities in the growing process should be minimized. It has been shown that spatial LS are strongly affected by the presence of defects and inhomogeneities of the semiconductor sample which affect CS addressing [Hachair, 2004], positioning [Pedaci, 2006; Pedaci, 2008b] and guided shifting [Pedaci, 2008a]. Inhomogeneities are related to crystal quality and they can appear as i) surface defects during epitaxy (> μm size) and ii) interface dislocations in the quantum well layer due to strain relaxation. We have reduced the defects number i) to less than 10000/cm^2 by using state-of-the-art MOCVD machine for GaAs based nanostructure, while we have controlled defect ii) by using strain balanced layers. Moreover, the choice of optically pumping the structure, instead of electrical biasing, allows avoiding further processing of the crystal, thus preserving its quality in terms of homogeneity.

- ***Gain mirror for high losses level.*** In VECSELs gain is provided by a thin layer of active medium and it is usually less than 1%. Hence, there is a critical amount of optical losses that the VECSEL can stand. In conventional VECSEL design the external cavity losses are low, since this latter is closed by a high reflectivity polished concave mirror, which is the only optical element and from where a tiny portion of light is extracted out from the cavity. Because we are aiming at self-imaging external cavity, we cannot rely on this guided-mode geometry. Moreover, our cavity will be delimited by the gain mirror and the SESAM and we will need an intracavity beam-splitter for extracting the light. The problem of the external cavity losses can be managed by increasing the available gain from the 1/2 VECSEL. This is achieved

by controlling the micro-cavity finesse of the gain sample which determines the confinement factor Γ of the field in the gain section. The gain mirror microcavity is due to residual reflection from its top facet and its finesse can be varied by

- ***Fast SESAM response.*** SESAM response should be faster than the gain recovery time ($\tau_{SA} < \tau_g$) for stable PML. Carrier recombination time of the SESAM should be below 0.1 τ_g (typically lower than 100 ps). On the other hand, the same issue of device homogeneity expressed for the gain mirror concerns the SESAM. Because SESAMs faster than 10 ps are usually fabricated at low temperature with a dramatic increase of surface defects, we will prefer high temperature fabricated SESAM with recombination time in the range of 10-100 ps.

- ***SESAM modulation depth.*** Another important parameter is the difference between saturated and unsaturated reflectivity of the SESAM (modulation depth). This modulation depth needs to be larger than 5% for ensuring bistability between the on- and off-PML solution [Marconi, 2014a; Javaloyes, 2016a]. At the same time, this modulation should not be too large for avoiding that threshold value for the VECSEL become out of the gain range. Moreover, the amount of non saturable losses in the SESAM should be minimized.

- ***External cavity.*** As pointed out several times, the external cavity setting is crucial for observing spatial and temporal LS. The latter demands a long cavity for achieving $\tau_g < \tau_c$. For typical values of τ_g we know that the cavity length should be larger than a half meter. Meanwhile, self-imaging configuration (SIC) is required for achieving high Fresnel number, as required by spatial LS. Self-imaging condition should be fulfilled in a full round trip, but it is also required that the gain mirror and SESAM should be in conjugate planes for enabling SESAM saturation.

- ***Efficient saturation of the SESAM.*** For achieving stable mode-locking the ratio between saturation fluences of the gain and absorber should be $s = F_G/F_{SA} \gg 1$. Saturation fluences depend on parameters that cannot be varied once the samples are fabricated (as it will be explained in the next section). Nevertheless, this ratio can be effectively changed experimentally by playing with the magnification factor of the imaging one-way cavity. If $\mathcal{M}$ is the magnification factor between the SESAM plane and the gain mirror plane, the ratio between the saturation fluences s increases by a factor of $\mathcal{M}^2$.

- ***Improvement of the optical elements.*** For building long and self-imaging external cavities as required above, a two lenses 4f arrangement would require lenses with long focal length. Their numerical aperture would be too small for our purposes. Accordingly, external cavity should contain at least 4 lenses, similar as in [Genevet, 2008]. These lenses should be of the best quality with the minimal amount of aberrations and perfectly AR coated for avoiding spurious back reflections and increasing the losses. Finally, light extraction from the cavity needs to be considered because neither the gain mirror nor the SESAM enable transmission.

- ***Pump size and shape.*** Once the external cavity is set in the self-imaging condition, the transverse size of the system depends ultimately on the pumped section of the gain mirror. Then, the pumped profile should be the largest and the most homogeneous as possible. However, since the pump power P_p cannot exceed 1 W because of thermal management problems in the gain section, the pump size cannot be increased arbitrarily. For conventional use, VECSELs are pumped by a Gaussian profile pump. Unfortunately, for our purposes, this profile is not homogeneous enough for taking advantage of the whole pumped region. A flat-top pump profile appears more convenient for our purposes. Commercial high power flat top pumps based on high power laser diodes which are coupled into a large core optical fiber turn out to be too inhomogeneous for our purposes. Hence, we have built a flat top pump based on a single-transverse mode diode laser.

2.2.1 Gain and SESAM structures

The devices used in this project were designed and optimized by the group of IES in Montpellier and manufactured at C2N in Paris. The chips are based on multi-layers

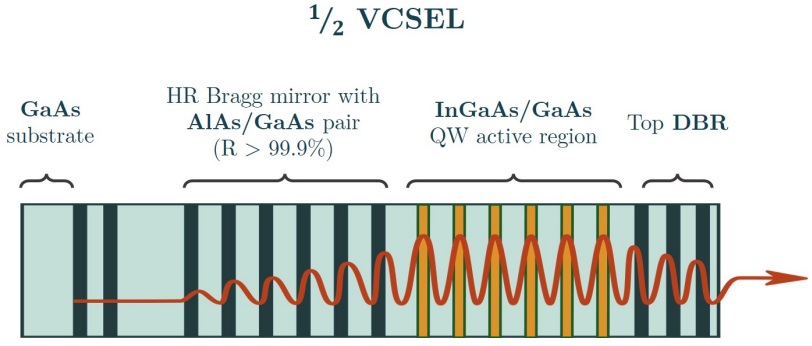

Figure 2.2. General scheme of the structured multilayer device

pairs of AlAs/GaAs for the DBR and InGaAs/GaAs for the quantum wells. The gain medium was designed for being optically pumped at ~ 800 nm and emit at ~ 1060 nm. A scheme of these structures is depicted in figure 2.2.

Two runs of gain mirrors were mainly used in this thesis. They are labeled as **GaAs-861** and **V0450**. The first one has an active region composed by 6 strain-balanced InGaAs/GaAsP QWs of 8 nm. Its bottom high reflectivity mirror (99.99 %) consists on 31 pairs of AlAs/GaAs. On the top facet, 3 pair of AlAs/GaAs were added for increasing the micro cavity confinement factor, which is the field enhancement inside the micro cavity, and goes up to $\Gamma = 12$. Its Fourier transform infrared spectrum (FTIR) is shown in figure 2.3 a). We can estimate the micro-cavity bandwidth to $\Delta\lambda_G = 3.5$ nm (FWHM). Saturation fluence goes above $F_G = 10\ \mu\text{J/cm}^2$, and the gain level at maximum pumping is 20%. Carrier life time (τ_g) goes up to 0.5 to 2 ns depending on the pump level.

On the other hand, V0450 consist of 12 QWs with photoluminescence peaked at 1040 nm and 25.5 pairs of AlAs/GaAs for the Bragg reflector. On the top facet 3 Bragg's pairs

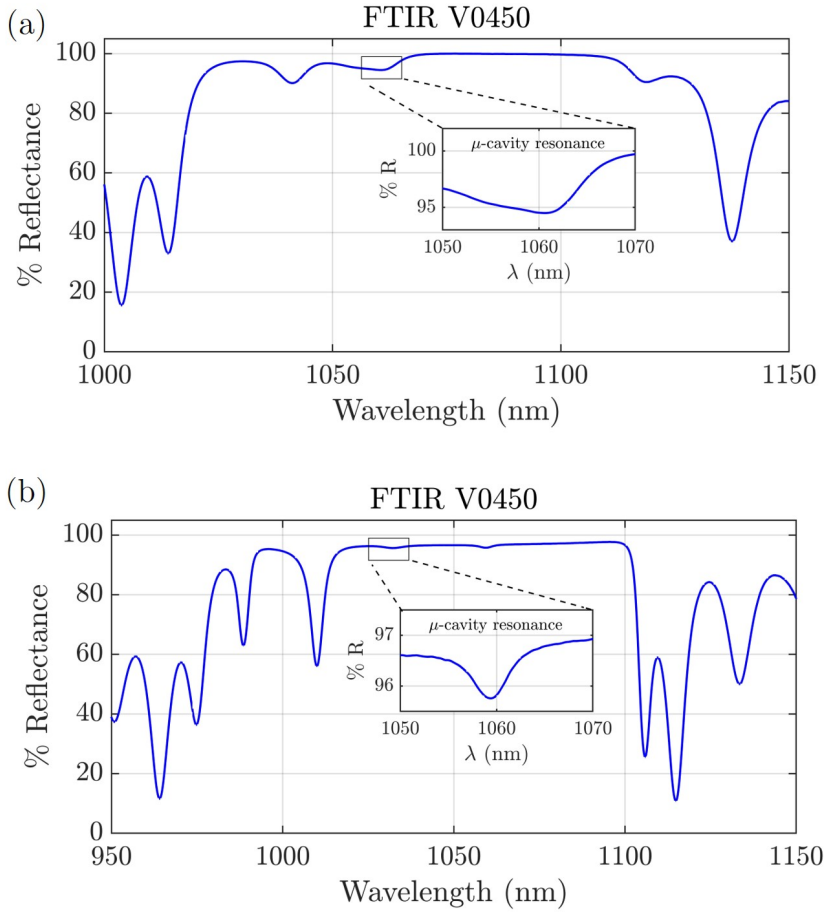

Figure 2.3. Fourier transform infrared spectrum for the gain mirrors (a) GaAs-861 and (b) V0450. In the former, the photoluminescence of the QW s plotted in dashed line, with a peak at 1040 nm. Micro-cavity resonance is around 1060 at room temperature for both devices.

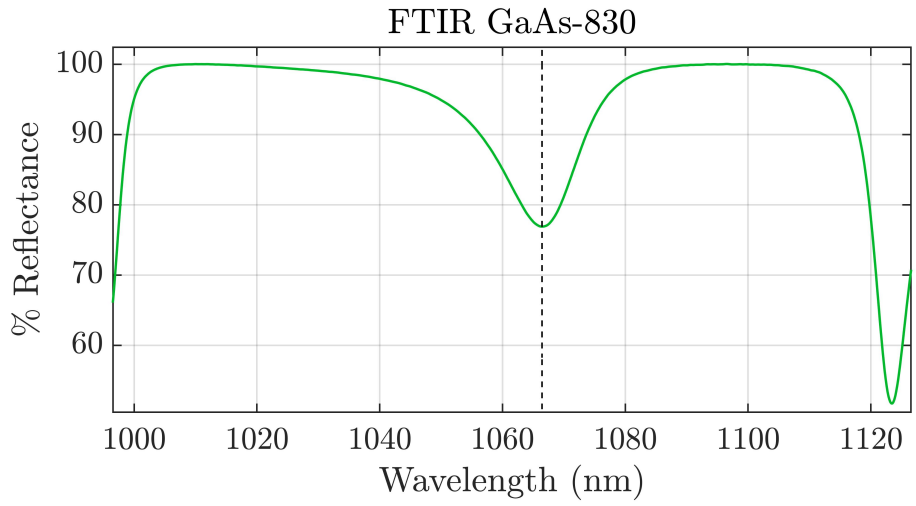

Figure 2.4. FTIR of the saturable absorber. It's maximum amount of losses is close to 22% at $\lambda_B = 1066.5$ (dashed vertical line).

were added, thus increasing $\Gamma = 4$. The micro-cavity bandwidth is $\Delta\lambda_G = 9$ nm, the saturation fluence goes above $F_G = 25\ \mu\text{J/cm}^2$ and the gain level at maximum pumping of 15%. Its FTIR is shown in figure 2.3 b).

The SESAM, **GaAs-830**, consist of only one InGaAs/GaAs QW at 2 nm from the external surface. This enables a fast recombination rate, up to 50 ps, together with high crystal homogeneity. This recombination rate is two orders of magnitude faster than the gain. Modulation depth was enhanced by adding a top dielectric Bragg mirror formed by a pair of SI/SiN layers. Its corresponding FTIR is shown on 2.4, where the gray vertical line marks the resonance is at 1066.5 at room temperature. The micro-cavity bandwidth is of $\delta\lambda_B = 15$ nm (FWHM). It's saturation fluence is $F_{SA} \sim 2\,\mu\ \text{J/cm}^2$. Unsaturable losses are less than one percent and the modulation depth at resonance is 22 %.

Both devices were temperature controlled independently. This enables to vary the position of the gain mirror micro-cavity resonance (λ_G) with respect to the one of the absorber (λ_{SA}). Hence, the detuning $\delta\lambda = \lambda_G - \lambda_{SA}$ is an experimentally accessible parameter and it enables control of the modulation depth experienced by the intracavity field.

2.2.2 First step for LS in VECSELs

INPHYNI's group started to explore the combination of GaAs-861 and GaAs830 in 2018, and realized the first observation of TLS in a PML VECSEL [Camelin, 2018]. The 4-lenses external cavity configuration, shown in figure 2.5 a), was set close to self-imaging condition. The gain mirror was pumped by a @780 nm elliptical laser diode

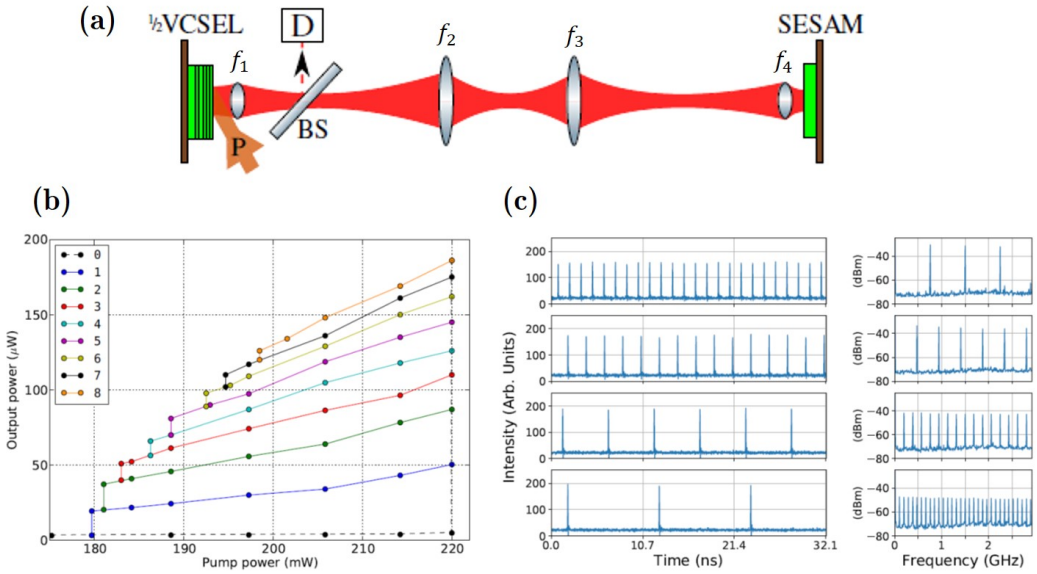

Figure 2.5. (a) 4-lenses VECSEL configuration. They light is extracted by a beam sampler (BS) of 2% of losses. (b) Bifurcation diagram of the pulse emission below threshold. (c) Time traces and its power spectra for different coexisting solutions [Camelin, 2018].

at the Brewster angle. After projection, such pump has a circular Gaussian profile of 50 μm diameter in the gain facet. Cavity length was set at $\tau_c \approx 10.7$ ns. By controlling the device's temperature, the detuning $\delta\lambda = \lambda_{SA} - \lambda_G$ was set to fix the modulation depth larger than 10%. In this parameter range the VECSEL emits several coexisting mode-locked pulsating states. The number of pulses N ranges from 0 (trivial solution) to 8. In figure 2.5 b) it is shown the bifurcation diagram of these states, when decreasing the pump current from lasing threshold. Panel c shows the temporal traces (left) and its corresponding RF spectrum (right) for multiple scenarios of coexisting mode-locked states.

From the spatial point of view, despite an external cavity configuration was set close to SIC, this system was emitting only on a fundamental Gaussian mode (15 μm waist). Several reasons explain this behaviors. First of all, as we will demonstrate in the following chapter, the positions of the optical elements were calculated for obtaining self imaging condition in the cold cavity. We will show that optical pump induces a thermal lens on the gain mirror which affects significantly the SIC. Hence, these positions for SIC are significantly different from the ones calculated when taking into account the pumped VECSEL. Another reason is related to the Gaussian profile of the pump which introduces a strong inhomogeneity in the transverse plane, thus favoring axial emission. The third reason is related to the fact that the lenses in the cavity were not used in a telecentric configuration but at distances significantly different from their focal lengths.

This setting increases significantly the aberrations and decreases the numerical aperture of the external-cavity, as we will show in section 2.4 through simulations with ZEMAX.

We have built on the results of Camelin concerning the temporal localization. Hence, we have maintained similar cavity length with a four lenses scheme and we have used similar values for the detuning between micro-cavity resonances. On the other hand, for implementing the large aspect ratio condition, we introduced several changes. First of all, we used a telecentric configuration for the external cavity, where distances between optical elements is given by the sum of their focal length. This configuration takes advantage of the full numerical aperture of the lenses and reduces the aberration impacts. Another important improvement is the possibility of introducing a magnification factor ($\mathcal{M}$) in the image of the SESAM onto the gain mirror. This magnification factor increases the ratio between the saturation fluences of the gain and the SESAM, improving mode-locking stability. While $s = 5$ for the samples used in Camelin's experiment, this ratio is increased by a factor of M^2 if magnification is introduced in the external cavity.

Accordingly, we propose to work with a 8-f 4-lenses cavity in a telecentric configuration, by keeping the same collimators as before ($f_1 = f_2 = 8$ mm). As a first step, we experimentally explored the case of $f_2 = f_3 = 150$ mm, for which $\mathcal{M} = 1$. Nevertheless, in such condition, no lasing operation was achieved close to SIC. Then the question is: how much the magnification needs to be increased to reach stable mode-locking in a self-imaging external cavity? In fact it is important to point out that large values of $\mathcal{M}$ challenge the numerical aperture of the collimator placed near the SESAM which will receive optical rays at an angle $\mathcal{M}$ times larger than the angle at which these rays leave the collimator placed near the gain mirror. It turns out that $\mathcal{M} = 2$, obtained with $f_2 = 100$ mm and $f_3 = 200$ mm, leads to a stable mode-locking emission for reasonable values of pumping power. At the same time, the cavity length is 632 mm, long enough for satisfying the condition for temporal LS. The experiments results reported in this thesis were obtained in this configuration. Section 2.3 will focus on the analysis of such cavity in the self-imaging condition.

2.2.3 Optical pump shaping

For the large aspect-ratio condition it is necessary to pump the largest area on the gain mirror. The limitation in total power that can be sent to the sample, forces us to take advantage of the full pumped area. By using a Gaussian pump profile, as in conventional VECSELs, only the central part of the profile can be considered sufficiently

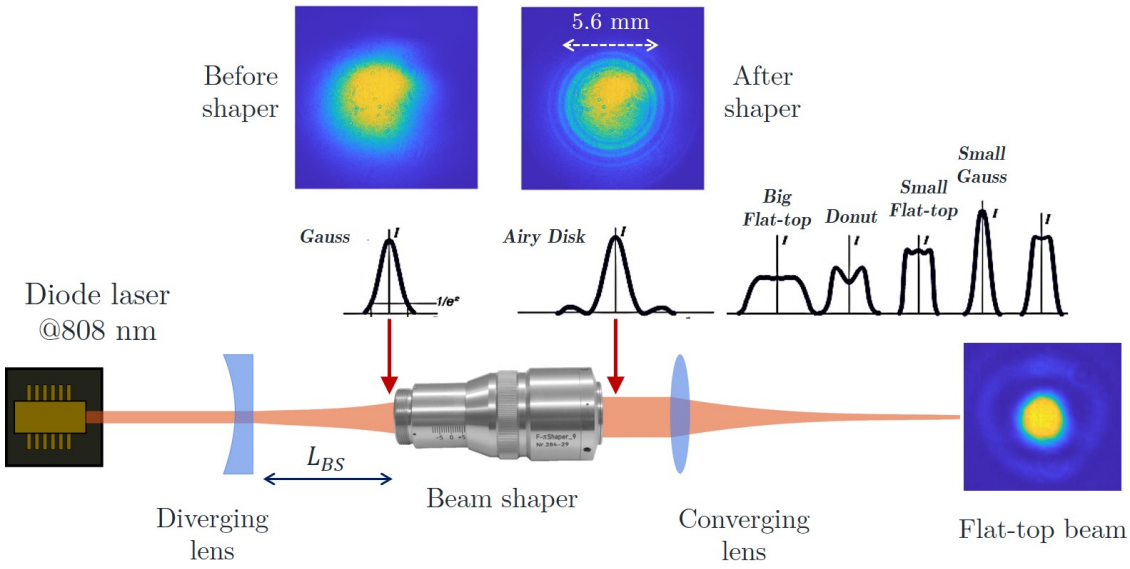

Figure 2.6. Scheme of the setup used for shaping the initial beam into a flat-top profile. (b) Spontaneous emission of the flat-top beam after the projection on the gain.

homogeneous to be exploited for generation of spatial structure. Instead, a flat-top pump profile allows to exploit the entire pumped area for generation of spatial structure. Besides this profile decreases the thermal and electronic lensing effect that we will described in the next subsection.

We use a single mode @808 nm laser from Eagleyard Photonics, that can emit up to 1 W of output power, and beam quality of $M^2 = 1.2$. The initial beam size is about 0.6 mm diameter, with a divergence of 37 mrad. For transforming it into a flat-top beam, the *Focal-πshape*r from Adl-Optica [Laskin, 2015] was used. This optical element converts a Gaussian beam into an Airy disk, as it is shown in figure 2.6. This beam propagates in a converging lens and diffraction creates different profiles at different distances with respect to the focus of this lens.. At the focal point a flat top beam appears. A distance η before the focal point we encounter a small Gaussian beam. Further distance $\eta/2$ gives an small flat-top. Another distance $\eta/2$ appears a donut. And finally, one more $\eta/2$ gives a big flat-top distribution. The parameter η is characterized by the laser used and the focusing lens. This is

$$\eta = \frac{8\lambda f_c^2 M^2}{\pi D^2}, \tag{2.1}$$

where D is the diameter (at $1/e^2$) of the shaper's output. Furthermore, the shaper requires a wide beam, between 5 to 6 mm diameter in the entrance, and with divergence below ± 5 mrad for its optimization. Since it's sensible to aberrations and misalignments,

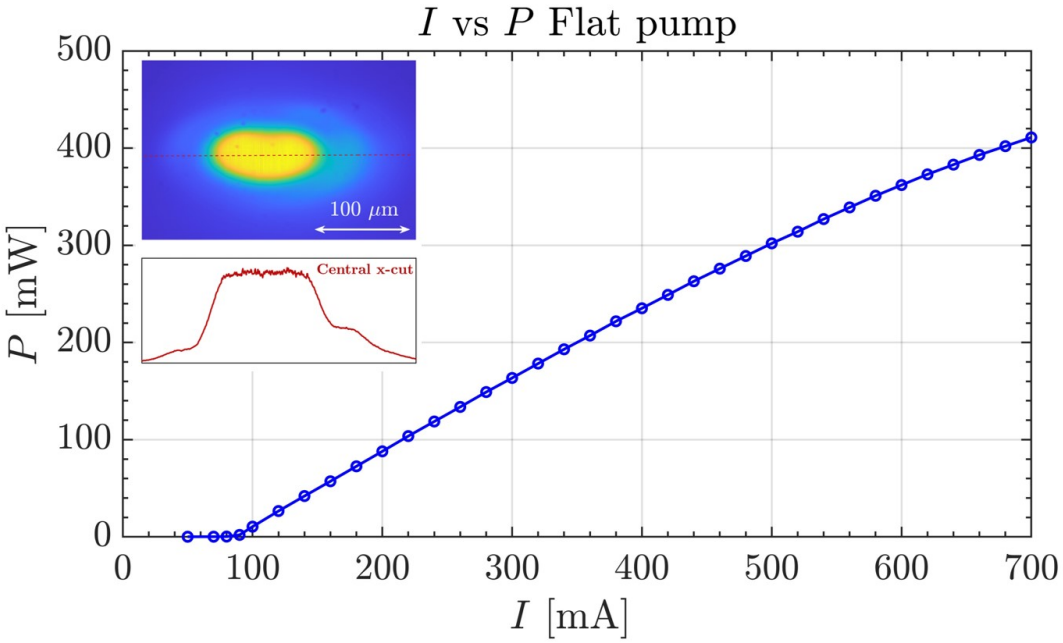

Figure 2.7. Output power vs current of the pump, measured after all its pass through the shaping setup. The inset shows the profile after the projection.

the manufacturers recommend tu use a diverging lens (f_d) for expanding an small beam. We used a plano-convex divergent lens of 25 mm focal length, for expanding the initial beam after a distance L_{BS} = 1400 mm. After such distance, the diameter measured was of 5.6 mm and a divergence of ~ 3 mrad, which is in the range of working of the shaper.

This beam is projected into the gain mirror, close to the Brewster angle, with a 200 mm focal length. In the gain, it appears as an elliptical flat-top of 95×55 μm (inset of 2.7). The P vs I curve was measured just after arriving to the gain, and its plot is presented in figure 2.7.

2.2.4 Thermal lens impact

Pump spot onto the gain mirror facet creates a thermal and electronic profile on the facet which impacts the refraction index of the semiconductor. Carrier profile induces a diverging lens while thermal profile induces a converging lens which dominates on electronic one [Laurain, 2009]. When the pump has a Gaussian profile, this effect can be approximated by a thin lens of focal length f_{th}. Focal length can be estimated as a function of the pump waist w_p (at FWHM) and its power P_p as [Yariv, 1991]

$$f_{th} \approx \frac{w_p^2}{2 \ln 2 \Gamma_g L_\mu} \left(R_{th} P_p \frac{dn}{dT} \right)^{-1}, \tag{2.2}$$

where Γ_g is the confinement factor, $L_\mu \sim 3\ \mu$m the size of the microcavity, R_{th} the thermal impedance and dn/dT the change on the refractive index with temperature. For GaAs and InGaAs structures, $dn/dT \approx 2.4 \times 10^{-4}$ K^{-1}. The thermal impedance is around 60 K/W when the wavelength operation is 1060 nm. The typical values of pump power we use are around 200 to 300 mW. Then it is expected to have a thermal lens from $\sim$ 55 to 35 mm, respectively. As we will show in the next section the presence of this spurious lens affect deeply the self imaging condition of the external cavity.

2.3 $ABCD$ matrix analysis for a self-imaging cavity

In an optical resonator with spherical components a Gaussian beam is the fundamental transverse mode. It is a solution of the paraxial wave equation for the scalar electric field of the form $E(\mathbf{r}) = A(\mathbf{r})\exp(-ikz)$ [Saleh, 2019]

$$\Delta_T A(\mathbf{r}) - i2k\frac{\partial}{\partial z}A(\mathbf{r}) = 0, \tag{2.3}$$

where $\mathbf{r} = (x, y, z)$, $\Delta_\perp = (\partial^2/\partial^2 x + \partial^2/\partial^2 y)$ the transversal Laplacian, k is the wave number.

The solution of equation 2.3 is the so-called spherical wave

$$A(\mathbf{r}) = \frac{A_0}{q(z)}\exp\left(-ik\frac{\rho^2}{2q(z)}\right), \tag{2.4}$$

with A_0 a constant, $\rho^2 = x^2 + y^2$. The q-parameter is $q(z) = z + iz_r$, where $z_r = 2\pi\omega_0/\lambda$ is known as the Rayleigh range. For separating both the phase and amplitude in the real and complex components, we can write it as

$$\frac{1}{q(z)} = \frac{1}{R(z)} - i\frac{\lambda}{\pi w^2(z)}, \tag{2.5}$$

and by substituting into 2.4 then

$$E(\mathbf{r}) = A_1\frac{w_0}{w(z)}\exp\left[-\frac{\rho^2}{w^2(z)}\right]\exp\left[-ikz - ik\frac{\rho^2}{2R(z)} + i\xi(z)\right], \tag{2.6}$$

with $A_1 = A_0/iz_r$, w_0 the minimum waist value at $1/e^2$ and

$$w(z) = w_0\sqrt{1+\left(\frac{z}{z_r}\right)^2}, \tag{2.7}$$

$$R(z) = z\left[1+\left(\frac{z}{z_r}\right)\right], \tag{2.8}$$

$$\xi(z) = \tan^{-1}\frac{z}{z_r}, \tag{2.9}$$

$$w_0 = \sqrt{\frac{\lambda z_r}{\pi}}. \tag{2.10}$$

Here w corresponds to the beam width at a distance z with a curvature radius R. The third term is known as the Gouy's phase shift, due to the delay of the wavefront in relation to a plane wave.

On the other hand, with the matrix formalism we can describe how a ray changes after passing an optical element. If the initial ray has position r_1 and angle θ_1, it is changed as

$$\begin{pmatrix} r_2 \\ \theta_2 \end{pmatrix} = \begin{pmatrix} A & B \\ C & D \end{pmatrix}\begin{pmatrix} r_1 \\ \theta_1 \end{pmatrix}. \tag{2.11}$$

where r_2 and θ_2 are new position and angle, respectively. This description of optics is only valid for both small distances off-axis and angles. So we can rewrite the matrix as

$$\begin{pmatrix} A & B \\ C & D \end{pmatrix} = \begin{pmatrix} \frac{\partial r_2}{\partial r_1} & \frac{\partial r_2}{\partial \theta_1} \\ \frac{\partial \theta_2}{\partial r_1} & \frac{\partial \theta_2}{\partial \theta_1} \end{pmatrix}. \tag{2.12}$$

Then, A and D play the role of spatial and angular magnification, respectively. B measures the spatial offset for a given initial angle. If $B = 0$, rays emitted at different angles will have the same offset. Finally, C is the focusing power, *i.e.*, if $C = 0$ the rays will remain parallel after the transmission. These parameters will depend of each component of the system, and follow $AD - BC = 1$. The most common matrices are,

$$\begin{pmatrix} 1 & d \\ 0 & 1 \end{pmatrix} \qquad \textit{Free space propagation} \tag{2.13}$$

$$\begin{pmatrix} 1 & 0 \\ 0 & 1 \end{pmatrix} \qquad \textit{Planar mirror reflection} \tag{2.14}$$

$$\begin{pmatrix} 1 & 0 \\ -1/f & 1 \end{pmatrix} \quad \textit{Thin lens} \tag{2.15}$$

$$\begin{pmatrix} 1 & 0 \\ 0 & n_1/n_2 \end{pmatrix} \quad \textit{Refraction of a planar interface} \tag{2.16}$$

$$\begin{pmatrix} 1 & 0 \\ -2/R & 1 \end{pmatrix} \quad \textit{Reflection on a curved mirror} \tag{2.17}$$

For a system with multiple elements, we can write a total transfer matrix as $\mathbf{M} = M_l M_{l-1} \cdots M_1$, where l is the total number of elements.

An optical resonator is a periodic system, where the light passes through the total matrix $\mathbf{M}$ an infinity of round-trips. Then, this system can be analyzed by finding the eigen values κ of

$$\mathbf{M} \begin{pmatrix} r \\ \theta \end{pmatrix} = \kappa \begin{pmatrix} r \\ \theta \end{pmatrix}, \tag{2.18}$$

which has solutions $\kappa_\pm = m \pm \sqrt{m^2 - 1}$, with $m = (A + D)/2$. For a stable resonator, light comes back with the same vector (r, θ) after each round-trip. This only happens when [Siegman, 1986]

$$m^2 < 1, \tag{2.19}$$

For a Gaussian beam, Kogelnik's law relates rays optics with the q parameter of equation 2.5. That is, the initial q_1 will change as

$$q_2 = \frac{Aq_1 + B}{Cq_1 + D}. \tag{2.20}$$

In an optical resonator, q replicates itself after each round-trip, *i.e.*, $q_1 = q_2$. The former equation can be solved for $1/q$, obtaining

$$\frac{1}{q} = \frac{D - A}{2B} - i\frac{\sqrt{4 - (A + D)^2}}{2B}. \tag{2.21}$$

Comparing the real and imaginary parts of this expression with 2.5, we obtain

$$R = \frac{2B}{D - A}, \tag{2.22}$$

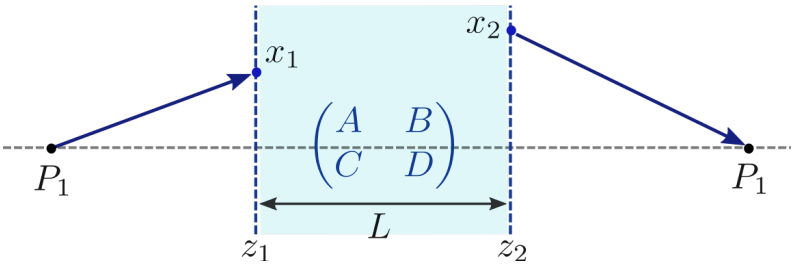

Figure 2.8. Scheme of the propagation through an $ABCD$ system, from plane z_1 to plane z_2.

$$w = \sqrt{\frac{\lambda B}{\pi}} \left(1 - m^2\right)^{-1/4}. \tag{2.23}$$

That is, expression in 2.23 represents the waist for the Gaussian solution, whose stability will be determined by the condition 2.19.

For a system characterized by the $ABCD$ matrix, we can write the generalized Huygens-Fresnel integral describing wave propagation from one point x_1 to a point x_2 whose plane are separated by a distance L (see Figure 2.8). In one dimension the transformation of the wavefunction U_1 to U_2 is [Siegman, 1986; Palma, 1997]

$$U_2(x_2) = e^{-ikL} \int \int \hat{K}(x_1, x_2) U_1(x_1) dx_1, \tag{2.24}$$

where $\hat{K}$ the Huygens kernel in one dimension given by

$$\hat{K}(x_1, x_2) = \sqrt{\frac{i}{B\lambda}} \exp\left[-i\frac{\pi}{B\lambda}\left(Ax_1^2 - 2x_1x_2 + Dx_2^2\right)\right]. \tag{2.25}$$

The middle term can be reduced as:

$$Ax_1^2 - 2x_1x_2 + Dx_2^2 = A\left(x_1 - \frac{x_2}{A}\right)^2 + \left(D - \frac{1}{A}\right)x_2^2, \tag{2.26}$$

and by using $AD - BC = 1$, then

$$U_2(x_2) = \sqrt{\frac{i}{B\lambda}} e^{-ikL} \exp\left[-i\frac{\pi C x_2^2}{\lambda A}\right] \int \int U_1(x_1) \exp\left[i\frac{\pi A}{\lambda B}\left(x_1 - \frac{x_2}{A}\right)^2\right] dx_1. \tag{2.27}$$

We note that B is homogeneous to a distance, C to the inverse of a distance, A,D are without dimensions. This expression can be compared with the Fresnel transformation in the free-space

$$U_2(x_2) = \sqrt{\frac{i}{\lambda l}} e^{-ikL} \int \int U_1(x_1) \exp[i\frac{k}{2l}(x_1 - x_2)^2] dx_1. \tag{2.28}$$

to see that the wave propagating in an $ABCD$ systems experiences diffraction as if it was propagating in free space on a distance equal to the value of B/A and that the term containing C adds a quadratic phase mask, *i.e.* a wavefront curvature given by C.

2.3.1 4-lenses telescopic cavity

We aim at realizing a self-imaging cavity, which corresponds to an unitary round-trip matrix. As discussed in the previous chapter, we have chosen a 4-lenses telecentric cavity where the mirrors planes are conjugate planes. Moreover we have a magnification factor $\mathcal{M} = 2$ between the SESAM plane and the gain section plane. The cavity is presented in figure 2.9, with L_1 and L_4 being aspheric, large aperture collimators ($f_1 = f_4 = 8$ mm), while L_2 and L_3 are low aberration achromatic lenses with $f_2 = 100$ mm and $f_3 = 200$. Cavity length is in total $L = 632$ mm. In this telescopic configuration, the magnification M defined above is given by the ratio between f_3/f_2. According to the experimental procedure for reaching SIC we can vary the position of the SESAM with respect to L_4, *i.e.* the distance d_5, we define $x = d_5 - f_4$, i.e. the shift with respect to the telecentric configuration. Then, the one way matrix can be written as

$$\begin{pmatrix} A & B \\ C & D \end{pmatrix} = \begin{pmatrix} 1 & f_4 + x \\ 0 & 1 \end{pmatrix} \cdots \begin{pmatrix} 1 & f_1 + f_2 \\ 0 & 1 \end{pmatrix} \begin{pmatrix} 1 & 0 \\ -1/f_1 & 1 \end{pmatrix} \begin{pmatrix} 1 & f_1 \\ 0 & 1 \end{pmatrix} = \begin{pmatrix} 1/\mathcal{M} & \mathcal{M}x \\ 0 & \mathcal{M} \end{pmatrix}. \tag{2.29}$$

As shown in the previous section, x fixes the value of B coefficient, *i.e.* diffraction. In this cold cavity imaging condition between the two mirrors and, consequently, SIC on the round-trip matrix is obtained for $x = 0$. However, when the gain section is optically pumped it is necessary to take account the impact of the thermal lens (f_{th}) induced by the pump whose (positive) focal length is tens of millimeters. This thermal effect can be approximated by a concave mirror of radius f_{th}. Its corresponding matrix is

$$\begin{pmatrix} 1 & 0 \\ -1/2f_{th} & 1 \end{pmatrix}. \tag{2.30}$$

Then expression 2.29 becomes

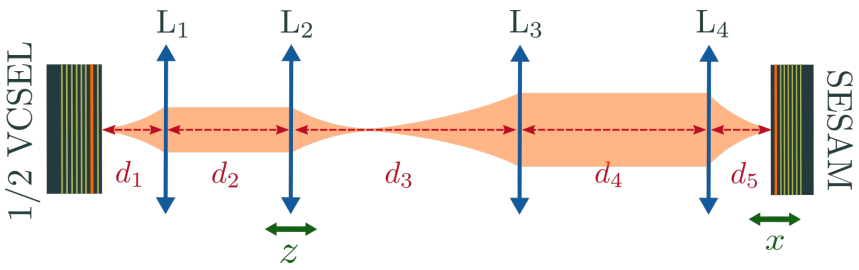

Figure 2.9. Ideal linear 4-lenses cavity in telescopic configuration, and magnification factor $\mathcal{M} = 2$

$$\begin{pmatrix} A & B \\ C & D \end{pmatrix} = \begin{pmatrix} 1/\mathcal{M} - \frac{\mathcal{M}x}{2f_{th}} & \mathcal{M}x \\ -\mathcal{M}/2f_{th} & \mathcal{M} \end{pmatrix}. \tag{2.31}$$

In the latter expression, $x \to 0$ leads to $B \to 0$. Nevertheless, C value is affected by the thermal lens and it cannot be set to zero just by changing the position of the SESAM. Hence the presence of thermal lens makes impossible to have imaging condition between the gain mirror and the the SESAM in a telecentric cavity, just by controlling x. This becomes possible by adjusting the position of a lens in the cavity and, for practical experimental considerations, we have chosen to vary the position of L_2. Accordingly, we introduce a new parameter $z = d_2 - (f_1 + f_2)$ which gives the position of L_2. The one way transfer matrix now reads as

$$\begin{pmatrix} A & B \\ C & D \end{pmatrix} = \begin{pmatrix} \frac{1}{\mathcal{M}} + (\frac{f_1^2 z}{\mathcal{M} f_2^2} - \mathcal{M}x)(\frac{1}{2f_{th}} + \frac{z}{f_1^2}) & \mathcal{M}x - \frac{f_1^2 z}{f_2^2 \mathcal{M}} \\ \mathcal{M}(-\frac{1}{2f_{th}} - \frac{z}{f_1^2}) & \mathcal{M} \end{pmatrix}. \tag{2.32}$$

The total round-trip matrix reads

$$\mathbf{M} = \begin{pmatrix} 1 + 2BC & 2DB \\ 2AC & 1 + 2BC \end{pmatrix}. \tag{2.33}$$

For a given value of f_{th}, imaging conditions between mirrors and identity round-trip matrix (which requires $A = 1/\mathcal{M} = 1/D$, and $C = 0 = B$) is obtained for:

$$z = z_0 = -\frac{f_1^2}{2f_{th}}, \tag{2.34}$$

$$x = x_0 = -\frac{f_1^4}{2\mathcal{M}^2 f_2^2 f_{th}}. \tag{2.35}$$

The bigger the thermal effect, the more important the variation of the positions with

respect the telecentric cavity. One of the most critical issues for achieving self-imaging condition is to establish an experimental protocol that may assess its fulfillment. In fact, both the presence of a pump dependent lens on the gain section and the precision requirement on the positions of the optical elements make impossible to achieve SIC just by placing them at the calculated positions. A reliable protocol has been identified by analyzing the waist of the fundamental Gaussian mode when the positions of L_2 and the SESAM are tuned around the SIC ($x = x_0$ and $z = z_0$). By introducing deviation from SIC, $\Delta x = x - x_0$ and $\Delta z = z - z_0$, we can rewrite 2.32:

$$\begin{pmatrix} A & B \\ C & D \end{pmatrix} = \begin{pmatrix} \frac{1}{\mathcal{M}} + \frac{(\Delta z)^2}{\mathcal{M}^2 f_2^2} - \frac{\Delta x \Delta z}{f_1^2} & \mathcal{M}\Delta x - \frac{f_1^2 \Delta z}{f_2^2 \mathcal{M}} \\ -M\frac{\Delta z}{f_1^2} & \mathcal{M} \end{pmatrix}. \tag{2.36}$$

The total round-trip matrix can be calculated using 2.33. Then, with the use of 2.23, we can obtain the beam waist as a function of x, z and f_{th}. In addition, the stability condition for the cavity 2.19 is $-1 < BC < 0$, *i.e.*

$$-1 < -\mathcal{M}^2 \frac{\Delta x \Delta z}{f_1^2} + \frac{(\Delta z)^2}{f_2^2} < 0. \tag{2.37}$$

We can see that for small deviation of z from the SIC (small values of Δz), the term in $(\Delta z)^2/f_2^2$ can be neglected. Thus the total round-trip matrix can be written as

$$\begin{pmatrix} A_{RT} & B_{RT} \\ C_{RT} & D_{RT} \end{pmatrix} = \begin{pmatrix} 1 & 2\mathcal{M}^2\Delta x \\ -2\frac{\Delta z}{f_1^2} & 1 \end{pmatrix}. \tag{2.38}$$

This latter expression is similar as the study developed in references [Taranenko, 1997] and [Noblet, 2012], where the self-imaging condition was assessed as well in a laser cavity. Accordingly, the stability condition requires $\Delta x > 0$ when $\Delta z > 0$ and $\Delta x < 0$ when $\Delta z < 0$.

Let's take an example for a fixed thermal lens, for instance f_{th}= 40 mm. In figure 2.19 a) it's presented the map for $w(x, z)$ in such condition. The pump small axis (55 μm) constrains the maximum value of $w_{max} \sim 30$ μm. So, $w > w_{max}$ are neglected in this analysis. The first thing to point out is that the SIC is not at $(x, z) = (0, 0)$, but at $(x_0, z_0) = (-1.3, -800)$ μm. The bigger the thermal effect, the more it will be shifted the point where $B = C = 0$. Second, we see that z_0 is of the order of few millimeters, while x_0 will be of few microns since $f_2 >> f_1$. Hence, by adjusting z and x we can reach SIC for any value of f_{th}. When SIC is approached by z, that is $|\Delta z| \to 0$, the waist

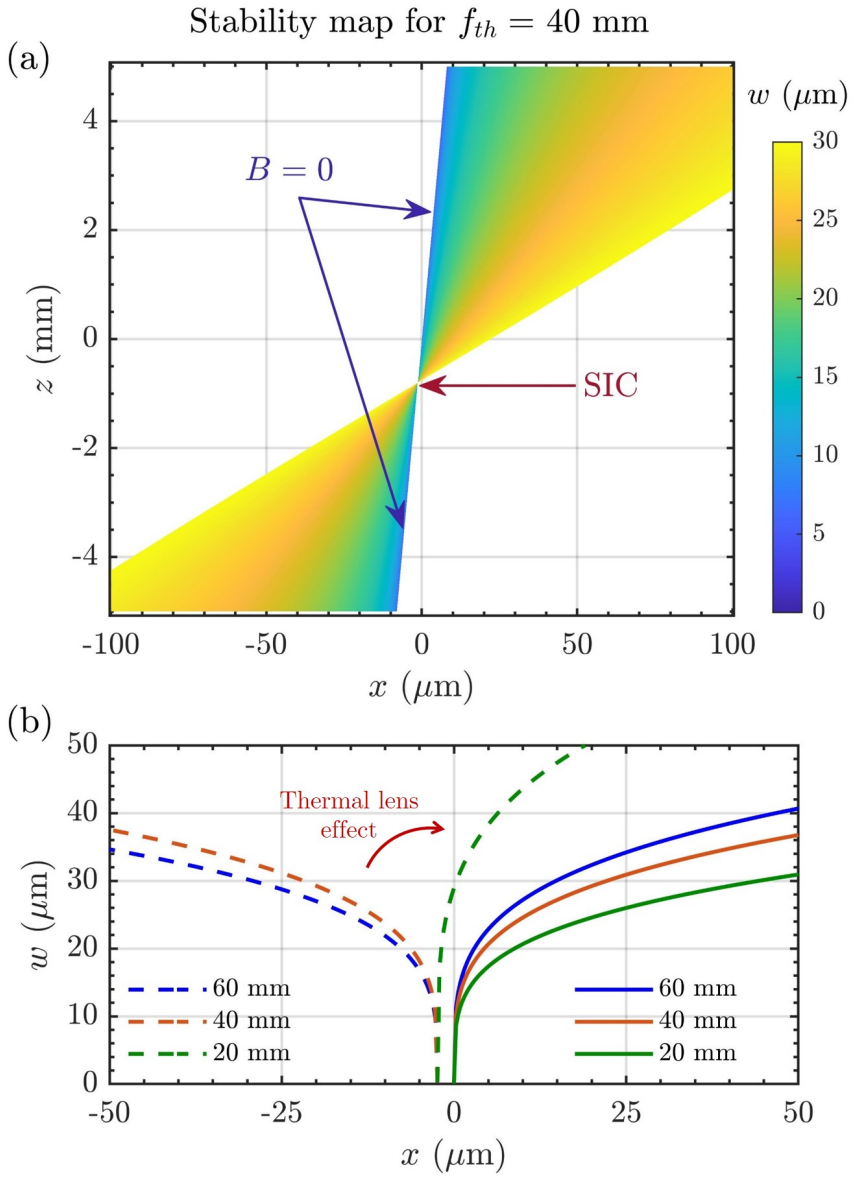

Figure 2.10. (a) Stability map for the fundamental Gaussian solution when a thermal lens of 40 mm, as function of x and z- (b) Waist evolution as function of x for different values of f_{th}. Dashed lines correspond to $z = -1.5$ mm and solid $z = 0$.

of the Gaussian solution as a function of x goes to zero. The slope of this behavior depends on the sign of Δz. For the negative case, w decreases conforming x does. That is, the SESAM position moves away from L_4, increasing the cavity length. The opposite behavior is obtained when $z < 0$. Finally, the map is divided in two regions depending of the sign of C. Left side corresponds to $C > 0$, while the right one for negative. The effect of thermal lens for a given value of z is now presented in panel b of figure 2.10. The dashed lines correspond for $z = -1.5$ mm, that is $C < 0$. When the thermal effect increases, that is, smaller values of f_{th}, the stability moves towards the right. Then, for critic value, it is possible to jump from one region to another, as it is seen in the case of

$f_{th} = 20$ mm. On the other side, the solid lines are for $z = 0$. The same effect appears, flattening its shape more and more, when f_{th} decreases.

2.4 ZEMAX characterization

Self-imaging condition, ideally, is a singularity where degeneracy of solutions of the Hermite-Gauss and Laguerre-Gauss basis appear [Arnaud, 1969]. Then, it is important to understand how accessible in real life this condition is and what are the limitations we could face with an optical system. For instance, the numerical aperture of the optical elements constrains the minimum spot size of the transverse plane and the depth focus of our image system. For example, an spot with 5 μm diameter ($\lambda = 1060$ nm) has a Rayleigh range of ~ 18 μm, then the question is whether is possible to have access and control of a longitudinal window of this size in real life. In the case, could we really conclude the self-imaging condition is achieved? Furthermore, aberrations and astigmatism arise due to the use of spherical components, especially for conditions far from the optical axis, as it could be an off-axis solution or a high numerical aperture mode. These solutions are for great interest in our desired system, since for spatial localization, we expect to have more than one emitting spot in a wide area, not necessary close to the optical axis.

A numerical tool that calculate the performances of a real optical system is the software ZEMAX. This software is a design platform for optical elements, and operates by modeling the ray propagation through a certain object. It considers all the actual important features, such as material refractive index, thickness, curvature and coating. Enterprises as Thorlabs, provide a ZEMAX file for most of its components. Therefore, it's possible to find, for instance, the optimal actual focal point of a lens measured from one of its surfaces at a given wavelength and numerical aperture. Moreover, in complex systems, as it would be a resonator, it allows to extract the amount of aberrations and astigmatism after one round-trip.

In this section we present an analysis of the passive VECSEL using ZEMAX software, in order to estimate how feasible is to achieve the SIC in a 4-lenses system. Even though in section 2.2.2 we present the motivation of using a telescopic cavity, we developed the analysis for the cases for $\mathcal{M} = -1$ as in Camelin's results, and our new proposition for $\mathcal{M} = 2$, in order to understand the impact of using an 8-f system and evaluate the SIC condition.

2.4.1 Cavity with $\mathcal{M} = -1$

We analyzed first the cavity of Camelin's work, where the configuration for $\mathcal{M} = -1$ was obtained using lenses with focal lengths $f_1 = f_4 = 8$ mm and $f_2 = f_3 = 150$ mm. The distances values of d_j $(j = 1 \ldots 5)$ were obtained by imposing $d_1 = d_5$, $d_2 = d_4$, and $\sum_j d_j = 1600$ mm, in such a way that the one way $ABCD$ matrix fulfills

$$\begin{pmatrix} A & B \\ C & D \end{pmatrix} = \begin{pmatrix} -1 & 0 \\ 0 & -1 \end{pmatrix} \tag{2.39}$$

.

The solutions are $d_1 = d_5 = 8.14$ mm, $d_2 = d_3 = 589$ mm and $d_3 = 404$ mm. Noteworthy, none of these distances correspond to the focal lengths of each lens.

The optical elements used in this work were two 8 mm focal aspherical collimators (C240TMD-B, with NA=0.5) in front of each sample, and two plano-convex lenses (LA1433-B) of 150 mm focal length. The coating of these elements have a reflectance of 0.33% and 0.29%, respectively. Light was extracted by a beam splitter (BSF10-A) placed between L_2 and L_3 at 45°, with a transmission of 99.33%, thus, inside the cavity light pass through a tilted element. The total losses of the system are ~ 3.78%.

Our analysis start with the imaging system optimization, where thermal effects are neglected. ZEMAX works by placing an *Object* (r_{ob}, θ_{ob}) in the initial plane. For us, this corresponds to the gain position. By default, its full transmission through one or more optical elements is observed in an *Image* plane, which for us is the SESAM plane. Telecentric and paraxial conditions are imposed into the calculations. For rays

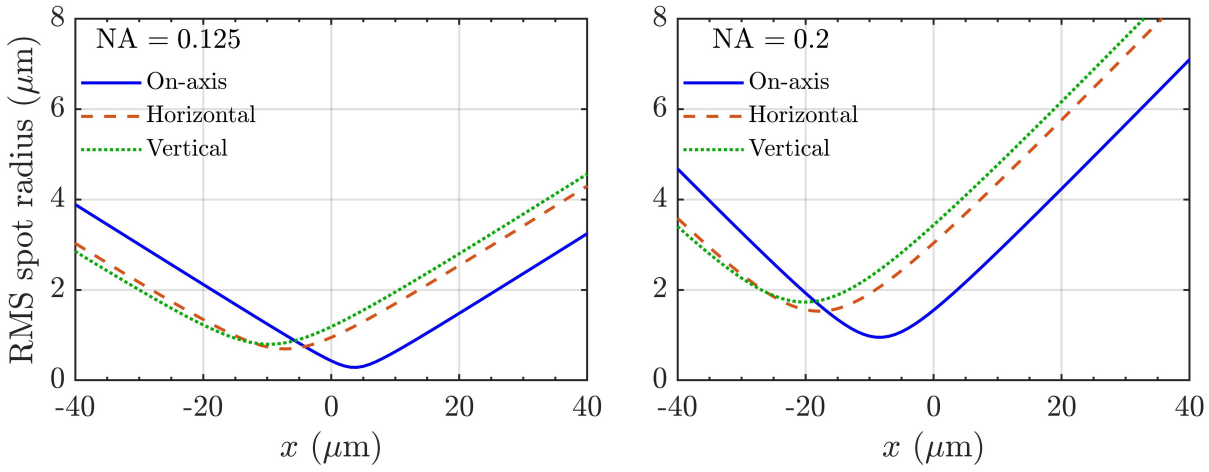

Figure 2.11. RMS spot radius as a function of the x position of the SESAM plane for $\mathcal{M} - 1$, when (a) N=0.125 and (b) NA=0.2.

Image Space NA	:	0.2007001
Object Space NA	:	0.2
Stop Radius	:	1.23291
Paraxial Image Height	:	0.0996366
Paraxial Magnification	:	-0.996366
Entrance Pupil Diameter	:	4.082483e+009
Entrance Pupil Position	:	1e+010
Exit Pupil Diameter	:	9.926145
Exit Pupil Position	:	24.25354

Figure 2.12. ZEMAX data sheet of the full pass with the values $d_1 = d_5 = 6.04$ mm, $d_2 = d_4 = 590$ mm and $d_3 = 409.6$ mm.

propagation, it is necessary to define a numerical aperture in the object space. The maximum numerical aperture of the system is defined by the collimators, NA=0.5. However, since the values of d_1 and d_5 does not correspond to the actual focal of the collimator (8 mm), this maximum value is reduced up to NA$\sim$ 0.4. Then, a reasonable option to choose would be half its size, NA=0.2. We used the ZEMAX data of elements mentioned and optimized the effective distances measured from each lens surface, for achieving the magnification of $\mathcal{M} = -1$. These distances are $d_1 = d_5 = 6.04$ mm, $d_2 = d_4 = 590$ mm and $d_3 = 409.6$ mm.

It is possible to obtain the root-mean-square (RMS) radial size. For that, the distance between each ray and the reference point is squared, and averaged over all the rays. After, the square root is taken. RMS provides a rough idea of how the rays spread. However it is important to recall these values does not correspond to the Gaussian beam size. In figure 2.15 it's presented the evolution of the RMS spot radius as a function of the x position of the Image plane. This position corresponds to the detuning x the SESAM from the position of the collimator $d_5 = 6.04$ mm. The best focus position spot is dependent on the NA chosen. That is, the focus is dependent on the beam divergence, which is defined by the beam size. We also observe an increase on the minimum spot size when NA increases, which is a result of the spherical aberrations of the system. In addition, because of the beam splitter has a tilted element, the spot radius presents different behaviors for a ray off-axis in the vertical or horizontal direction. That is, this system is anisotropic.

In the system data sheet it is provided the spatial magnification (see figure 2.12). That is $A = -0.99$. The value of D can be obtained by the ratio of the numerical aperture of the image space and object space. Then $D = -1$. Both results are quite close to the ideal

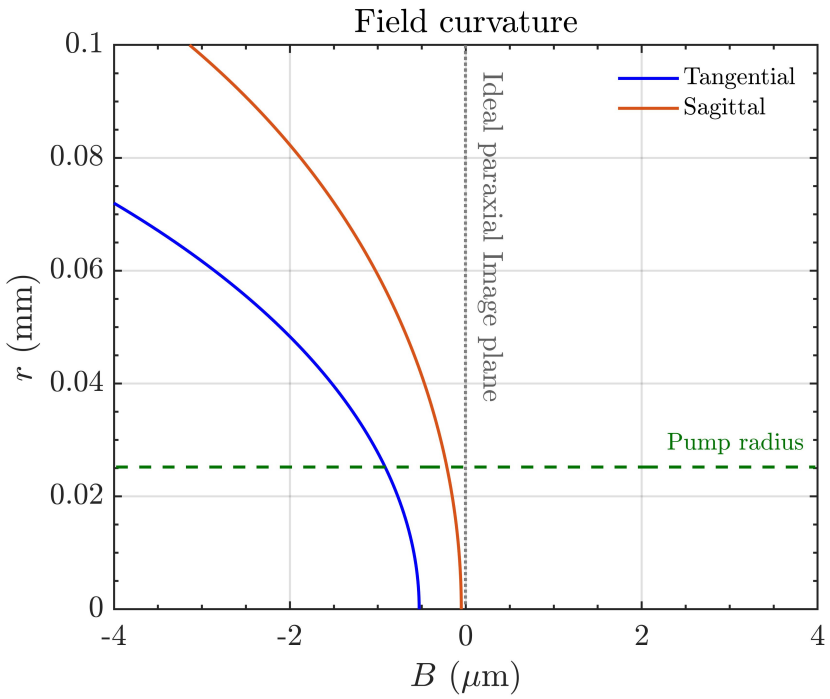

Figure 2.13. Field curvature after the full optical path for both tangential and sagittal conditions. The parameter B is quantified as the offset distance from the paraxial image plane and the actual image plane.

case. B and C, however, have to be estimated indirectly.

B can be obtained by measuring the field curvature after the full path of the system. In the look for spatial localization we are interested that several solutions, not necessary on-axis, are stable. Then with the field curvature it is possible to evaluate how big is the window where the resonator behaves a planar-planar cavity. For an ideal spherical system, any initial ray (r_{ob}, θ_{ob}) will arrive into the same plane at its focal plane, *i.e.*, the paraxial plane. In practice, such plane is curved due to aberrations. A given r_{ob} generates a chief ray with an incident angle into the $ABCD$ system, and will focus at an offset distance from the paraxial plane. In figure 2.17 are the calculations for both tangential an sagittal cases, where the pump window area is marked with dashed lines. Then, it is assumed the curvature is a quadratic function, so

$$B_{T,S} = b_{T,S} r^2, \tag{2.40}$$

where the subindex depends whether is tangential or sagittal. Fitting both curves we obtain that $b_T = 730\ \mu\text{m}^{-1}$ and $b_S = 300\ \mu\text{m}^{-1}$. However, again we observe a detuning between the solutions for the tangential and sagittal plane, which means the ideal paraxial plane is different between them. This difference is about 0.5 μm, and comes

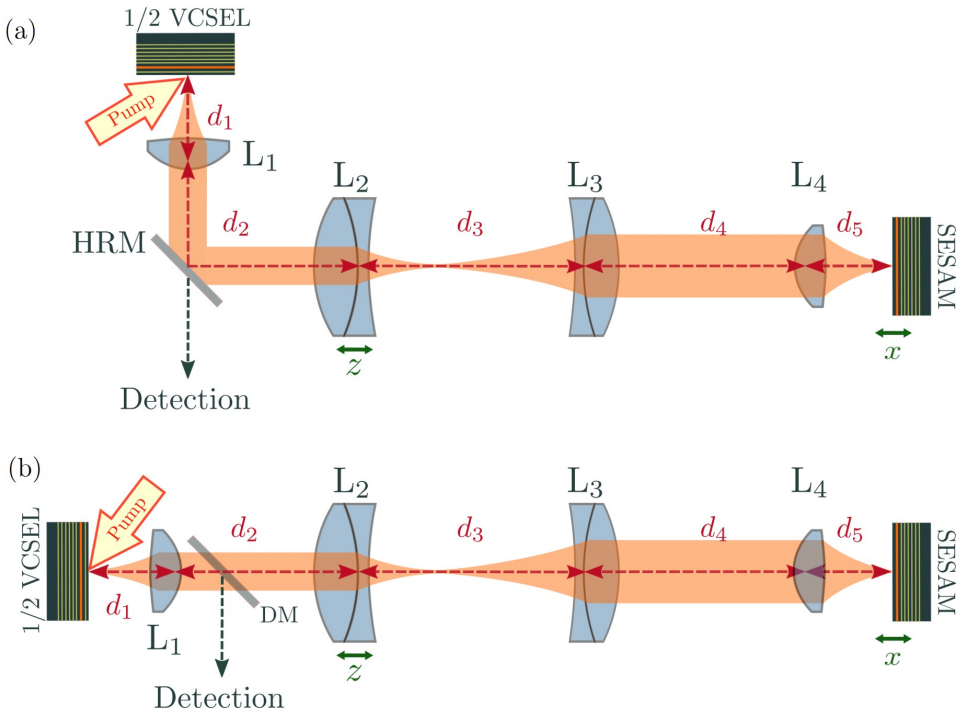

Figure 2.14. (a) L-shape configuration, where the light is extracted by through a high reflectivity mirror (HRM). (b) Straight cavity where a dichroic beam sampler mirror (DM) is used for light extraction.

from the fact that rays passing through the splitter are not parallel. Such solution is not favorable in the case we would like to have an array of spatial solutions separated by a distance of few microns. For instance, the solution with two spatial LS of 10 μm separated by the same distance, will not be possible.

Finally, the value of C can be rewritten with the use of the definitions on 2.12 as

$$C = \frac{\theta_{im}}{r_{obj}}, \tag{2.41}$$

where θ_{im} is the incident angle of the ray in the image plane. For this case, due to the anisotropy, we obtained two values depending on the transverse direction the ray is sent with the offset. In the horizontal plane $C_h \sim 50\ \mu\text{m}^{-1}$, while $C_v \sim 40\ \mu\text{m}^{-1}$ for the vertical.

2.4.2 Cavity with $\mathcal{M} = 2$

Regarding the optical elements used in this work, they were chosen making a balance between optical quality, in terms of aberrations, and the amount of cavity losses were are able to deal with. These last ones, were reduced by choosing elements with specific coating for enhancing transmission at 1060 nm. In front of each sample an 8 mm aspheric

Lens	Effective focal (mm)	Frontal focus (mm)	Back focus (mm)
1	8	5.90	7.9
2	100	90.22	105.8
3	200	192.86	199.86
4	8	5.88	7.9

Table 2.1. Position obtained with ZEMAX of the full system in the paraxial telecentric condition.

collimator was used (∅ 0.5 inches) with reference C240TME-1064 from Thorlabs catalog. Its numerical aperture is NA = 0.5, and the reflectivity at 1064 is around 0.1%. For L_2 and L_3, achromatic doublets were chosen with effective focal lengths of 100 mm and 200 mm, respectively (∅ 1 inch). Coating reflectivity is close to 0.2% (AC254-XX-C series). The use of doublets improves beam quality at focus in comparison to common plano-convex lenses. For extracting the light, two different configurations were considered. The first one is an L-shape cavity, where the emission was taken out through a high reflectivity wedged mirror (HRM) with 99.5 % of reflection at 1060 nm. Its Newport reference is 10QM20HB.12. It allows high reflection for visible wavelengths, resulting an advantage for alignment purposes. In a total round-trip, the system will have ∼ 3.4% of losses, just by the optical elements. In this case, the light inside the cavity does not pass through any tilted element, and then can be considered as linear. The second option is a straight cavity, using a longpass dichroic mirror (DM) at 45°, with reflectance of 1.75% at 1060 nm (DMLP90). In this case the total losses increase up to 5.9%. In comparison with the previous configuration, light does pass through a tilted element. An scheme of both configurations is presented in the figure 2.14

Since $\mathcal{M} = 2$, the maximum NA possible of the system is half the collimator's one, $\mathrm{NA}_{max} = 0.25$, which also defines the maximum divergence angle of a beam in the object space $\theta_{max} = 14.4°$. Therefore, it is practical to fix NA below this limit. For instance 0.125. Lenses, due to their geometry and width, have different focal distances depending on the side light enters. In comparison with the previous system, we look for a telescopic system, therefore, we take advantage of the tool for optimize the minimum spot imposing telecentric condition and NA=0.125. We call frontal focus to the distance the lens is optimized to use for focusing, and back focal for the collimating side. Then the process goes in chain by adding one by one the lenses, in a way the best focus condition is preserved. The final *Image* plane corresponds to the position of the SESAM.

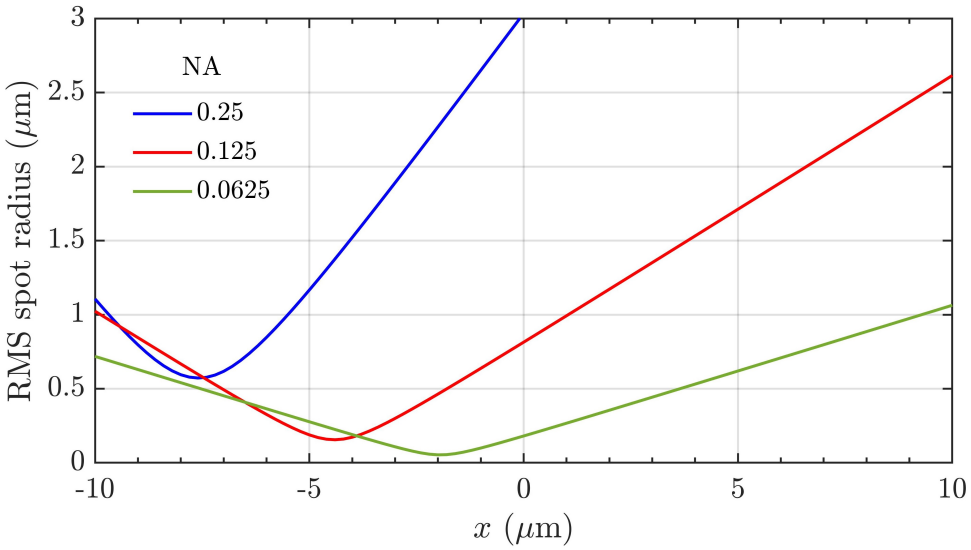

Figure 2.15. RMS spot radius as a function of the x position of the SESAM plane.

The values obtained are in Table 2.1.

In figure 2.15 it is presented the evolution of the RMS spot radius as a function of the x position of the Image plane. This position corresponds to the detuning x from the position of the collimator 5.9 mm (Table 2.1). Again, the best focus position spot is dependent on the NA chosen, and the minimum spot size increases when NA does it. However, due to the absence of the tilted element, anisotropy does not appear.

In the system data sheet it is provided the spatial magnification (see figure 2.16). That is $A = 0.5$. The value of D can be obtained by the ratio of the numerical aperture of the image space and object space. Then $D = 1.96$. Both results are quite close to the ideal case.

Figure 2.17 presents the field curvature for estimate the value of B. We can note that both curved planes start at the same point, in comparison to the previous case. Fitting both curves we obtain that $b_T = 130\ \mu\text{m}^{-1}$ and $b_S = 50\ \mu\text{m}^{-1}$. These values are about five

Image Space NA	:	0.2443053
Object Space NA	:	0.125
Stop Radius	:	-0.02383326
Paraxial Image Height	:	0.0500073
Paraxial Magnification	:	0.500073
Entrance Pupil Diameter	:	2.519763e+009
Entrance Pupil Position	:	1e+010
Exit Pupil Diameter	:	27.48239
Exit Pupil Position	:	-54.54164

Figure 2.16. ZEMAX data sheet of the full pass with the values of Table 2.1

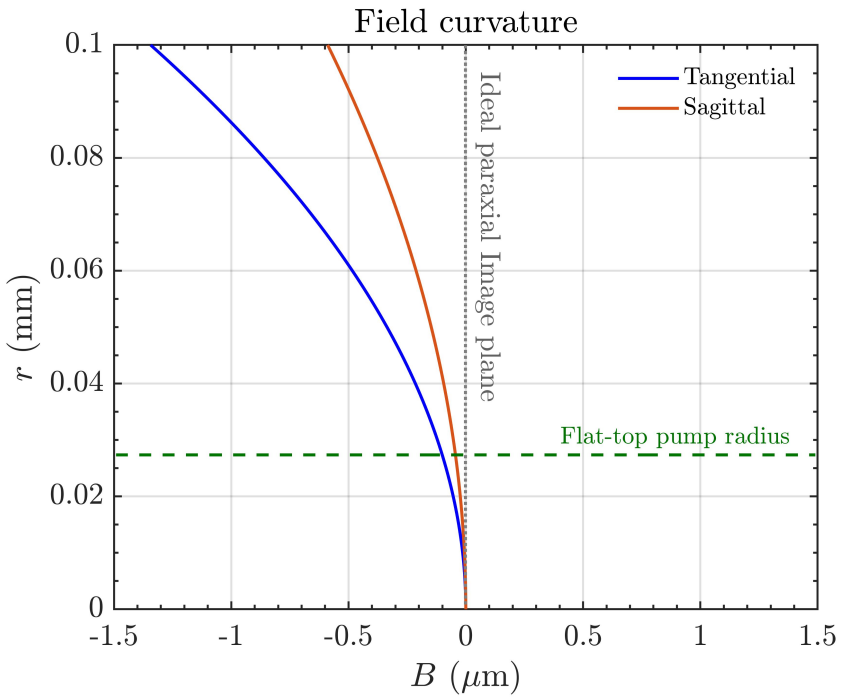

Figure 2.17. Field curvature after the full optical path for both tangential and sagittal conditions. The parameter B is quantified as the offset distance from the paraxial image plane and the actual image plane.

times lower than the case of $\mathcal{M} = -1$. The affection of the curved plane for a solution within the pump area, is below 0.1 μm for both tangential and sagittal cases. Hence, the planar condition could be achieved and solutions with more than one spot inside the pump is feasible and will not be limited by the optical system. We could say that a Gaussian-like spot between 5 to 30 μm, whose Rayleigh range is much larger than the planar-planar condition presented in 2.17, can be considered a spot emitting in the self-imaging condition.

From the analysis developed in section 2.3, we introduced the parameter z for tuning the position of the second lens L_2 from L_1. The behavior of C is presented as a function of z in figure 2.18 a). It's minimum is $C_{min} \approx 0.3 \times 10^{-4}$ mm^{-1} at $z = 0$. This point correspond to the position of $L2$ at its back focus, 105.8 mm (see Table 2.1). Noteworthy, two regions are identified depending on the slope of the curve.

The wavefront aberrations give us an indicator of how the beam is focusing (or defocusing) depending on the z tuning. ZEMAX by default uses a virtual exit pupil of diameter d_p, where the beam has a clear defined edge in the *Image* plane (SESAM position). A reference sphere is created with radius d_p located in the Image space. Consequently, a ray from the Object space is traced all way through the system up to

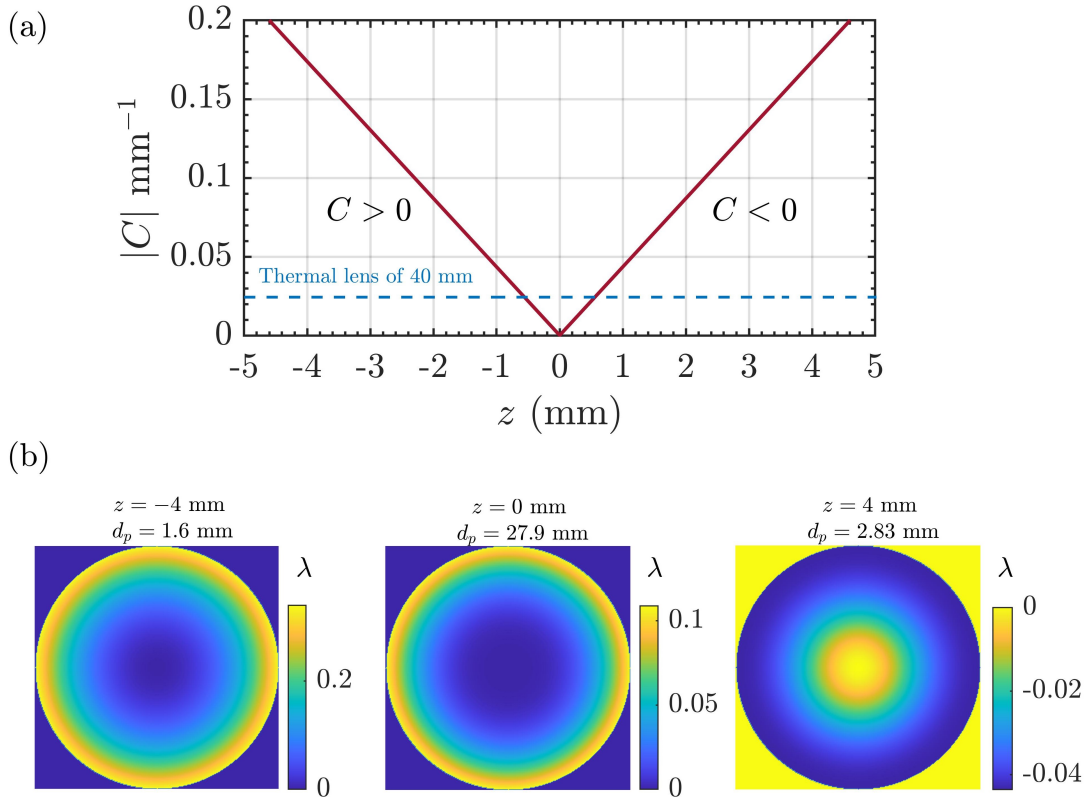

Figure 2.18. (a) Evolution of C parameter when detuning L_2 a distance z from L_1. (b) Wavefront error in wavelength for different positions z of L_2 respect to L_1.

the Image (r_{im}), and traced backwards to the reference sphere. Is sent back again to the Image, r'_{im}, and the *optical path difference* between r_{im} and r'_{im} is the physically significant phase error.

In figure 2.18 b) are the wavefront errors for different z. When $z = 0$ (middle panel), the virtual pupil chosen has diameter of 27.9 mm, and there is a wide central transverse area about few mm^2 where phase error is minimum. This is a result of the *planar-planar* system we have built, as close to SIC possible. The error starts to appear with positive phase close to the edge of the pupil, that for our case is far from the optical axis. For $z < 0$ (left panel) the pupil size has diminished for one order of magnitude. In few μm^2 the phase error is present with almost double the magnitude of the previous case. Since this error is positive, the rays are defocusing and then $C > 0$. Finally, when z is positive (right panel), there is a sign inversion on the phase and the central part is more affected. Therefore $C < 0$, since a focusing condition is present. It is important to remark that the phase error comes from the Spherical aberrations of the total system.

The Seidel coefficients S_i can be obtained for the full path. The first three are presented in Table 2.2. As we can see, the main contribution to spherical aberrations comes from

Lens	Surface	Spherical (S_1)	Coma (S_2)	Astigmatism (S_3)
1	f	5×10^{-4}	-7 $\times 10^{-5}$	-1.1 $\times 10^{-5}$
	b	-3.87 $\times 10^{-4}$	8.2 $\times 10^{-5}$	2.7 $\times 10^{-5}$
2	b	7×10^{-6}	-1.2 $\times 10^{-5}$	2 $\times 10^{-5}$
	f	-6 $\times 10^{-6}$	7 $\times 10^{-6}$	-8 $\times 10^{-6}$
3	f	-1.2 $\times 10^{-5}$	-6 $\times 10^{-6}$	-3 $\times 10^{-6}$
	b	1.5 $\times 10^{-5}$	1.2 $\times 10^{-5}$	9 $\times 10^{-6}$
4	b	-6.42 $\times 10^{-3}$	-3.4 $\times 10^{-4}$	2.4 $\times 10^{-5}$
	f	8.1 $\times 10^{-3}$	3 $\times 10^{-4}$	-9 $\times 10^{-6}$
Total		1.79 $\times 10^{-3}$	-2$\times 10^{-5}$	5 $\times 10^{-5}$

Table 2.2. Seidel coefficients (in mm) for each surface pof the optical elements, in order from Object to Image space for $z = x = 0$.

the second collimator due to the magnification $\mathcal{M}$. The system total spherical aberration is of the order of 10^{-3}, then it is expected to have an influence in the spatial emission when we detune x and z far from the SIC.

Finally, we analyze the configuration inserting the DM into the cavity. Since light passes through a tilted element the imaging condition becomes anisotropy, as it was shown before for $\mathcal{M} = -1$. However, this time this anisotropy cannot be seen in the field curvature, since L_1 is placed in order to collimate the NF of the gain, and hence all rays are parallel. On the contrary, the strongest impact is reflected in the parameter C, that has different values for X and Y directions. The figure 2.19 is presented the $|C|$ as a function of z, where $z = 0$ corresponds to the paraxial imaging point (like in figure 2.18 a)). C_{min} difference between one axis and the other is about half a millimeter. The optimum value C' instead is when both curves cross each other. Nevertheless, C' goes up to 10^{-2}, which is two orders of magnitude compared to the L-shape case.

2.5 Conclusions

In this Chapter we have presented the road map we have followed for the design of a VECSEL source in order to obtain localized structures. Such road map is based on the results on the works of Genevet and Marconi, where a gain medium is coupled to a saturable absorber, and spatial and temporal localization were obtained, respectively.

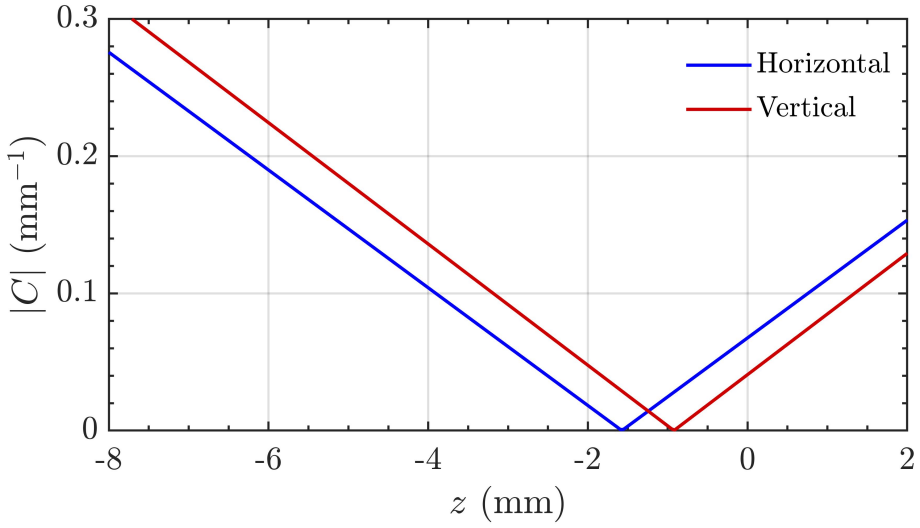

Figure 2.19. (a) Evolution of C parameter when detuning L_2 a distance z. (b) Wavefront error for different z in wavelength.

In collaboration with the groups of IES and C2N, two gain mirrors were designed, GaAs-861 and V0450. By adding the top Bragg mirrors during the process of fabrication, confinement factor Γ_g was increased up to 12 and 4, respectively. A SESAM structure was built as well, in order to achieve PML solutions. The first combination, GaAs-861 plus SESAM, was successfully used by Camelin for obtaining TLS with a Gaussian profile. We have improved this set up for achieving large aspect ratios. First, we build a pump with a flot-top profile in order to take advantage of the whole pumped region on the gain mirror. Second, we have analyzed the impact of the thermal lens effect due to this pump, expecting values of f_{th} between 20 to 60 mm, depending on the pump power. The ABCD matrix analysis allowed us to identify the role of the parameters in the $ABCD$, where A and D are the paraxial and angular magnification, respectively, whereas parameter B controls the diffraction on the system and C introduces a wavefront mask that produces a focusing effect. This analysis reveals the impact of thermal lenses on SIC, and we have realized that it is possible to obtain SIC by tuning the positions z of L_2 and the position x of the SESAM from L_2. By observing the evolution of the waist w of the fundamental Gaussian beam as we scan x, we can identify the lens positions for SIC and quantify C parameter. Finally, our ZEMAX study was performed considering most of the features of our optical elements and we were able to evaluate the quality of SIC for the passive external cavity. We developed a comparison between the cavity schemes with $\mathcal{M} = -1$ and $\mathcal{M} = 2$, where this latter was achieved in a telecentric condition, showing the advantages from one over the other. In general, parameters

A and B are mostly dependent on the ratio of L_2 and L_3 effective focals. However, we determine that B and C are not zero, and are strongly affected by the aberrations and numerical aperture of the system. The use of a beam sampler for extracting the light from the cavity, produces anisotropy in the imaging system. For $\mathcal{M} = -1$ this effect impacts the field curvature, splitting the tangential and sagittal planes, with an offset of $\sim 0.5\ \mu$m, whereas for $\mathcal{M} = 2$ this effect is present on the parameter C, where planar-planar conditions are not the same for the horizontal and parallel directions. In addition, when the light is extracted with the dichroic mirror, C is even more affected due to the tilted element. This encourage us to decide for the L-shape configuration for most of our experiments.

CHAPTER 3

Time-localized patterns

Contents

3.1 Introduction

This Chapter presents the experimental results we have obtained in large aspect-ratio VECSEL operated in the regime of temporal localized structures, i.e. in the limit where the external cavity round-trip is larger than the internal bulk timescales (gain and absorber recovery times). For achieving the large aspect-ratio condition the external cavity has been set in self-imaging condition (SIC) with the gain mirror and the SESAM placed in conjugate planes. Moreover, a large area (an elliptical area of 50X90 micron) of the gain mirror has been optically pumped with a flat top pump profile.

As we have shown in Chapter 2, thermal lensing effect strongly affect the self-imaging condition and it requires to adjust properly the position of the cavity lenses. Hence, self-imaging condition cannot be obtained simply by calculating the position of the optics in the cold cavity situation. Moreover, the lens positioning at absolute distances (even when the reference planes are known thanks to ZEMAX) can hardly be realized with a precision better than the millimeter. Hence, the assessment of self-imaging condition requires an observational protocol, *i.e.* an experimental procedure that evaluates the effects of the tuning of the lens position on the elements of the cavity round-trip $ABCD$ matrix and that establish a criteria for converging to the self-imaging condition. This observational protocol, which has been introduced in chapter 2, will be implemented into the experiment in this Chapter 3. We show that it enables to identify unambiguously the external cavity setting which unlocks the occurrence of spatio-temporal structures not imposed by cavity boundaries but rather by system nonlinearities. Hence, when approaching self-imaging condition, the fundamental Gaussian mode gives way to patterns which do not self-transform in the Fourier space. These patterns cannot be interpreted in terms of guided modes as Hermite-Gauss or Laguerre-Gauss which exhibit homothetic near and field profiles. As described in the previous Chapter, the approaching to SIC is realized by tuning the position of the SESAM (which controls mainly the B parameter of the $ABCD$ matrix) and the position of L_2 in the cavity (see figure 2.10) which control mainly the C parameter of the $ABCD$ matrix.

We will show that the characteristics of the patterns observed depends strongly on the sign of the parameter C. In the positive case, off-axis tilted waves appear in an annular symmetry, which suggest the cavity is degenerated azimuthally. In this case, their transverse vector $\vec{k}_\perp$ is a function of B parameter and increases as $B \longrightarrow 0$. Such behavior is ruled mainly by the aberrations of the system. On the other hand, when $C < 0$, the patterns consist of a combination of an axial plane-wave with a set of tilted waves having a nearly hexagonal arrangement in the Fourier space. These plane waves are locked in phase and their interference gives birth to a honeycomb profile in near-field. When $C \sim 0$, the spatial emission presents degeneracy, showing coexistence between different patterns. Finally, in the time domain the observed patterns are temporally localized mode-locked pulses having a duration around ten picoseconds, and we demonstrate how they can be addressed individually by short pump pulses. We have performed interferometric studies for estimating the pulse coherence time and for evaluating the correlation of distinct points in the emitted patterns.

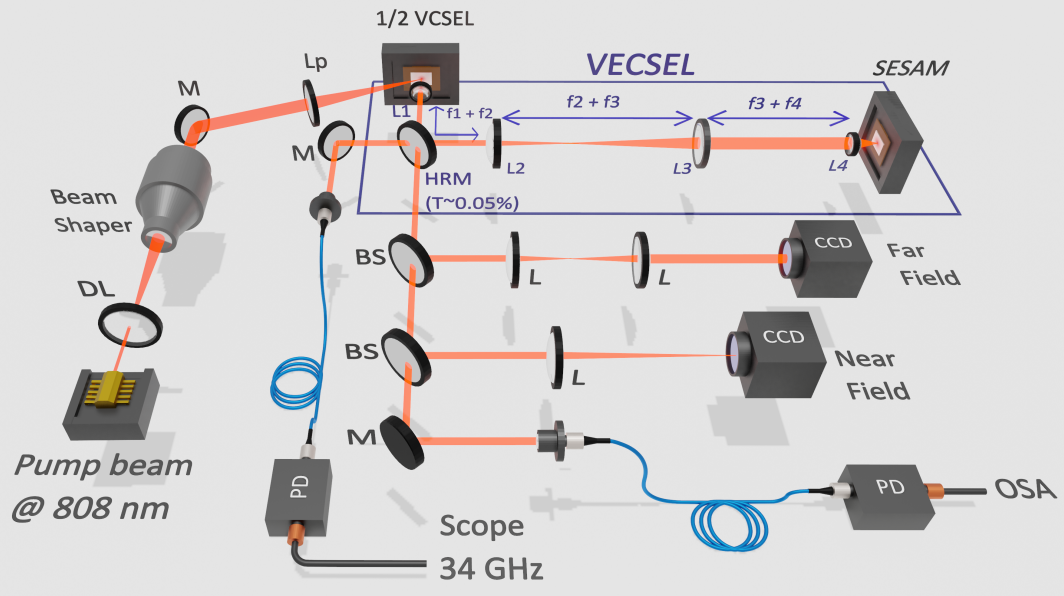

Figure 3.1. Experimental setup scheme of the VECSEL and its spatio-temporal detection.

The results presented in this Chapter were obtained with the L-shape VECSEL described in section 2.4, figure 2.14 a). Most of these results were obtained with the gain mirror sample V0450. Nevertheless, very similar results were obtained with the sample GaAs-861 as well. The latter was used during the first two years of my thesis, while the former was available in the last year. Few experiments have been performed with the GaAs-861 and were not repeated with sample V0450. In these cases, we will point out that the gain mirror sample is the GaAs-861. The length of the cavity used is around 632 mm, giving a round-trip time of $\tau_c \approx 4.3$ ns. Spatial averaged images were analyzed by two silicon CCD cameras, one in the near field of the gain, and one in its far field. For studying the temporal behavior of these patterns, the output signal was collected by optical fibers connected to 9 GHz photo detectors (Thorlabs series PDA8GS), and sent to a 4 channels 34 GHz Oscilloscope (Tektronix DPO73304d). Furthermore, a spatio-temporal resolved detection was developed by sending the output signal to an array of 8×8 optical fibers, where 4 of them were connected to the Oscilloscope. This fiber array enables spatial resolved detection at high bandwidth, and it is extremely useful to characterize the spatio-temporal dynamics. A scheme of the full setup is presented in figure 3.1.

3.2 Self-imaging condition assessment

In the previous Chapter we have developed a study of a 4-lenses self-imaging cavity in presence of the thermal effect induced by the pump. We analyzed the waist (w)

evolution of the Gaussian solution as a function of the position of the SESAM expressed by x, that quantifies the shifting on the distance d_5 between L_4 and the SESAM, with respect to the telecentric arrangement $x = d_5 - f_4$. The variation of x allows to control the value of B and, accordingly, the value of the fundamental Gaussian waist w (see equation 2.23) and, as $B \to 0$, $w \to 0$. While the cold cavity situation SIC can be achieved when $x = 0$, in presence of pump induced thermal lens SIC cannot be achieved simply by varying x. Accordingly, we have considered to vary also the distance d_2 between L_1 and L_2, where we have called z the shift of this distance with respect to the telecentric arrangement $z = d_2 - (f_1 + f_2)$. This additional degree of freedom allows to compensate the thermal lens effect and achieve the SIC. For a fix f_{th}, SIC is located at $(x, z) = (x_0, z_0)$ (defined in equation 2.34). Around SIC, in section 2.3 we have studied the evolution of w as a function of $\Delta x = x - x_0$ and $\Delta z = z - z_0$. As shown in figure 2.10, we identified two regimes for the evolution of the waist, depending on the value of d_2. If d_2 is larger than the sum of the focal lengths, $\Delta z > 0$ and $C < 0$, the waist w goes to zero when x decreases. On the opposite, when d_2 is shorter than the sum of focal lengths, $\Delta z < 0$ and $C > 0$, w goes to zero when x increases.

Based on these observations we have implemented an experimental analysis of the waist for the fundamental Gaussian mode as a function of micrometer longitudinal displacements (x) of the SESAM around the SIC. This translation is performed by using a sub-micron precision (minimum step of 0.5 μm) translation stage for large displacements and with a piezo-electric controller that enables 1 nm step, for fine resolution. The waist w is measured onto the gain mirror facet (near field emission profile). This evolution has been obtained for different position of L_2 around SIC. Experimentally the translation of L_2 is realized by a 0.5 micron precision translation stage with a full range of 2.5 cm.

In agreement to the analysis performed in Chapter 2, two scenarios have been found experimentally depending on the sign of Δz, and Figure 3.2 reports an example of it. For a pump value of 200 mW ($f_{th} = 55$ mm), the SIC position is located at $z = z_0 = -0.58$ mm. We have fixed d_5 few millimeters shorter than $f_1 + f_2$ and we have measured the evolution of $w(x)$, plotted with green circles on 3.2. We notice that w decreases by increasing x, *i.e.*, when the distance between SESAM and L_4 increases. We can fit these results with the formula of 2.23 from Chapter 2, and this enables to determine the value of $\Delta z = -2.74$ mm plotted with the orange solid line. In terms of $ABCD$ matrix, this situation correspond to $C = 0.086\,\text{mm}^{-1}$. On the other hand, if we fix d_2 larger than

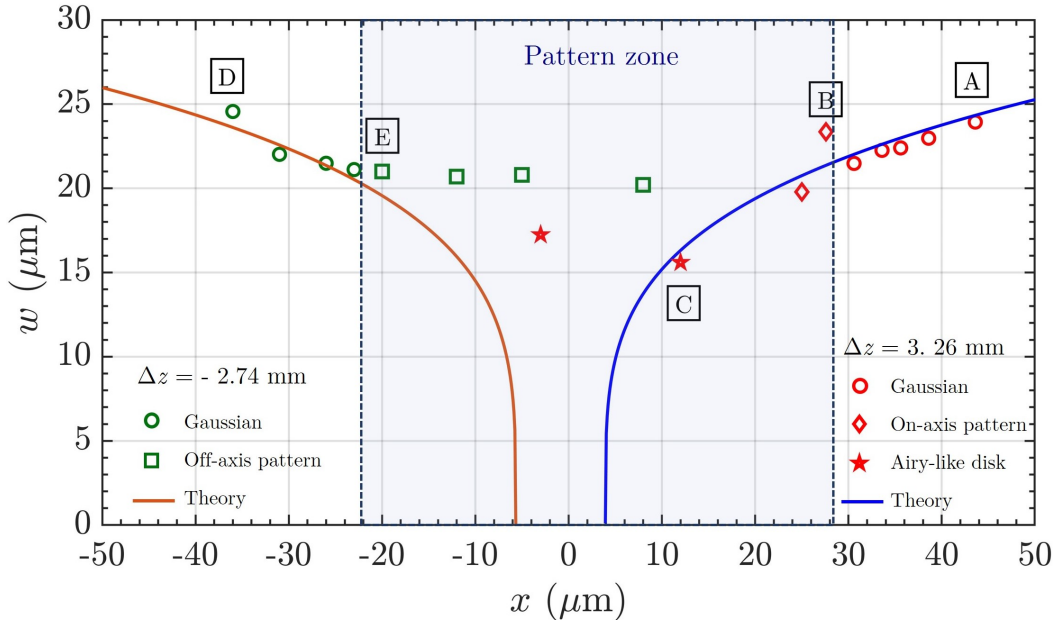

Figure 3.2. Experimental (markers) and theoretical (solid line) waist evolution as a function of the SESAM position x. Circle markers depicts the waist of the fundamental Gaussian mode, while the rest for pattern solutions. For $\Delta z > 0$, the pump value was 260 mW (f_{th} = 40 mm) and for $\Delta z < 0$ P_p = 200 mW (f_{th} = 55 mm).

$f_1 + f_2$ for few millimeters, we obtained the evolution of the $w(x)$, plotted with red circles on 3.2. We have set the pump value at 260 mW (f_{th} = 40 mm) locating the SIC at $z = z_0 = 0.8$ mm. We observe that w decreases when the SESAM gets closer to L_4, and by fitting with 2.23 (blue curve) we determine $\Delta z = 3.26$ mm. This regime correspond to $C = -0.1\,\text{mm}^{-1}$.

In both situations, when $\Delta x \to 0$ patterns replace the Gaussian emission. These patterns do not exhibit homothetic near field and far field profiles and they cannot be interpreted in terms of transverse modes imposed by boundaries (as Hermite-Gauss or Gauss-Laguerre modes). Their characteristics depends on the sign of Δz, *i.e.* on the C value of the $ABCD$ matrix description. We also confirmed that no lasing is possible for positive (negative) Δx when Δz is negative (positive), as expected from the stability analysis presented in Chapter 2 (see figure 2.10 a)). In the following section we present a full spatial and temporal description of the regimes defined by the value of C. In addition, the case $C \sim 0$ will be presented as well.

3.3 Case $C < 0$

In section 3.2 has demonstrated the experimental evidence of two different regimes depending on the sign of C. Negative value of C is achieved by placing L_2 at a distance

d_2 larger than $f_1 + f_2$. In this section we present the study of the spatial lasing emission as a function the position x of the SESAM. Figure 3.3 shows the near field (top), central cut (middle) and far field (bottom) profiles of the gain mirror, for the three scenarios identified for different values of x increasing. These profiles were taken with the same conditions of the previous section ($\Delta z = 3.26$ mm), and are marked in the stability curve (figure 3.2), as a reference from the position of the Gaussian beam solution.

Starting from the largest distances x, we observe that, for $x > 27$ μm, the emission corresponds to the Gaussian mode solution, which was used for the characterization of the SIC (panel A). Its central cut presents the data profile and the typical fitting used for the SIC characterization. In the intermediate region ($x\epsilon[22, 27]$ μm), the patterns exhibit a hexagonal-like structure. This pattern cannot be interpreted as a mode imposed by

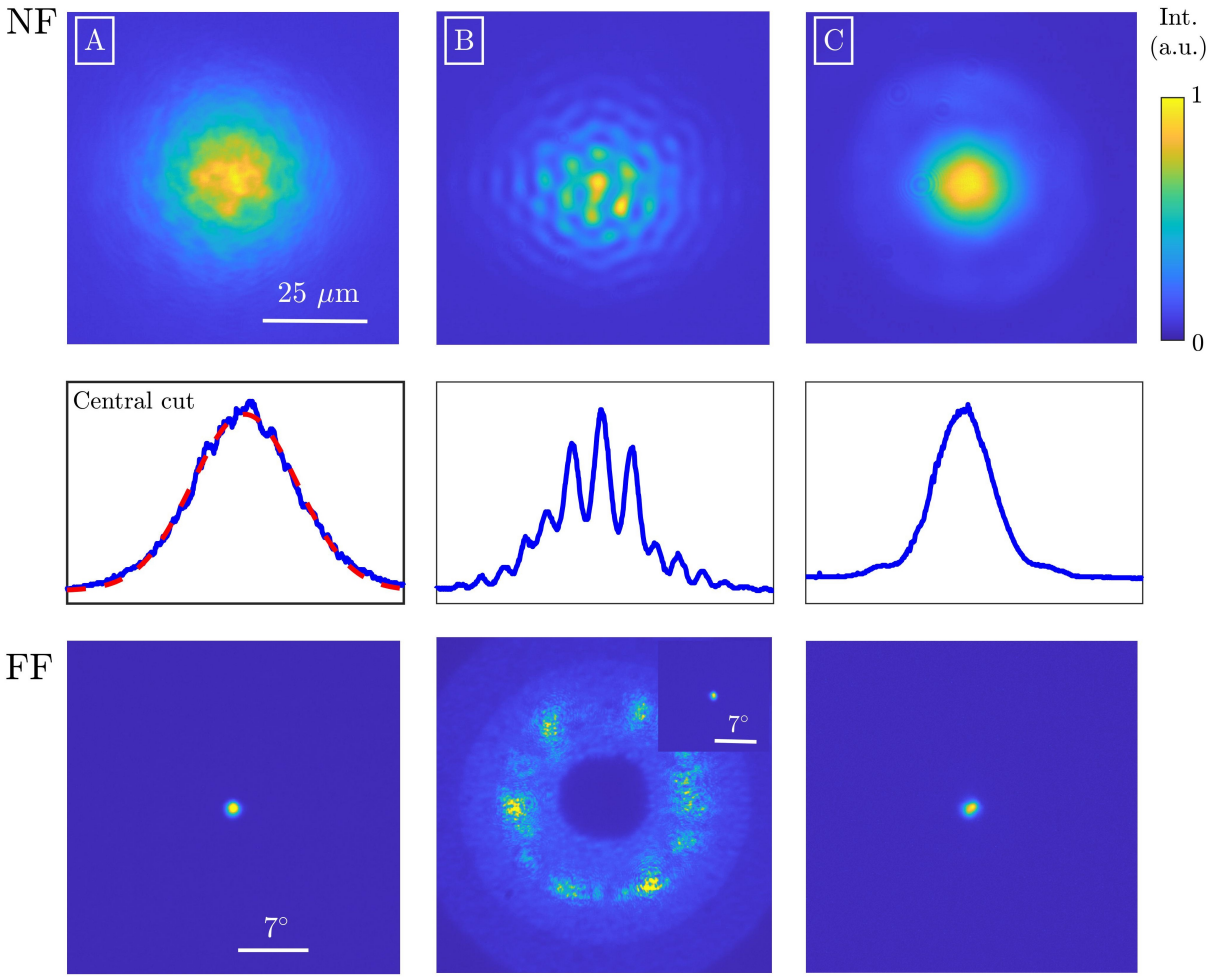

Figure 3.3. Spatial evolution for $C < 0$ ($\Delta z = 3.26$ mm) when x is decreased, for a pump value $P_p = 320$ mW. For $x > 27$ μm The VECSEL emission consists of the Gaussian fundamental solution which near-field profile is homothetic in far-field (A), For $x\epsilon[22, 27]$ μm a non homothetic pattern appears (B) and for $x\epsilon[-3, 22]$ μm, the emission consists an Airy-like disk (C). The FF in B was obtained by blocking the on-axis component in the detection, which contains 90% of the total energy. Its inset presents the full FF.

transverse boundaries of the resonator. While guided modes as Hermite-Gauss or Laguerre-Gauss self-transform in the Fourier space, thus leading to homothetic near and field profiles, the pattern shown in B, exhibits different near field and far field profiles. The far-field profile reveals a bright central spot surrounded by a nearly hexagonal arrangement of weaker spots. We evince that the VECSEL is emitting an on-axis plane wave together with a set of plane waves traveling at an angle of approximately 7° with respect the optical axis of the resonator. In the near field we observe an honeycomb like pattern with some brilliant spots. The regularity of this arrangement is affected by the presence of inhomogeneities on the gain section and SESAM used as it can be observed by shifting in the transverse direction the samples, as shown in Fig. 3.4. Finally, in the range $x\epsilon[-3, 22]$ μm, the near field profile consist of a central spot surrounded by a thin ring, similar to an Airy-disk (panel C). The corresponding far field exhibit a central spot and it is not homothetic to the far field profile. The size of the structures in B and C are also presented in figure 3.3, taking account its FWHM.

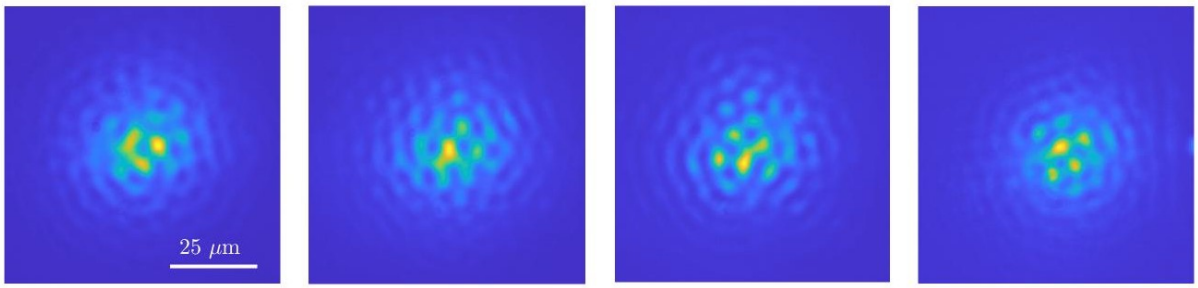

Figure 3.4. Variety of pattern distribution for different transversal positions of the SESAM.

We now focus on the hexagonal patterns shown in figure 3.3 B. This kind of pattern is observed in the range 0.1 mm $< \Delta z <$ 4 mm. and, as Δz is decreased, its existence range gets narrower in the range of x and it requires higher level of pumping. The spatial profile of the phase for this pattern has been performed using a phase profile sensor, with a *Phasics SID4* camera. This instrument is able to measure the intensity and phase of a beam simultaneously via interferometry and it calculates the Zernike's coefficients of an aberrated beam, enabling to remove some phase components such as divergence, coma, aberrations, tilting and so on. The output beam passes through several optical elements before arriving to the sensor, due to the imaging detection system we have developed. In order to observe its phase profile it is useful to remove the spurious phase components due to this. In figure 3.5 we show the near field (right) and phase profile (left) of two different patterns. As we know, in the near field the intensity profile

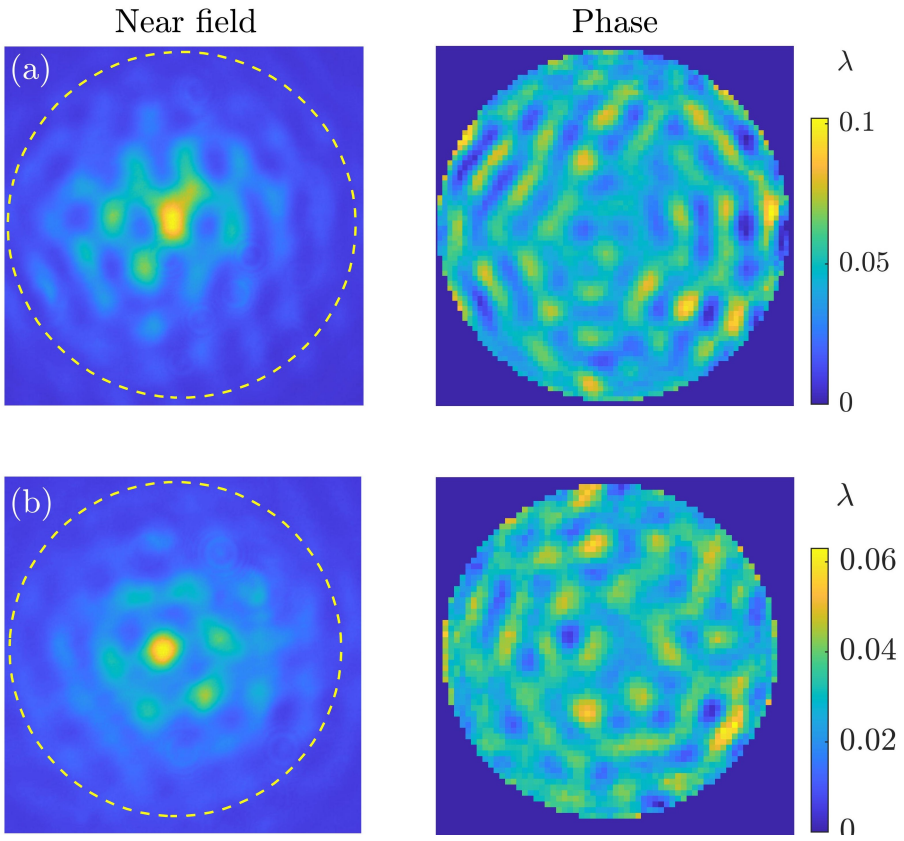

Figure 3.5. Near field and phase profile of different patterns, showing the inhomogeneities of the SESAM. The circled corresponds to the mask used for the Phasics calculations.

corresponds to an hexagonal modulation of the on-axis component. After removing the first Zernike's coefficients we observe the same modulation appears in the phase profile, with values that go about 0.1 wavelengths. This remaining phase follows the spots that appears on the pattern, and as we discussed previously, when the SESAM mirror is shifted transversely, the phase modulation as well. Therefore, the phase also follows the inhomogeneities of the SESAM facet.

In figure 3.6, we analyze the near-field profiles of the Fourier elements of the observed pattern. If we consider only the central spot in the far field, the corresponding near field profile has a Gaussian shape (panel b). This component brings 90% of the optical power of the pattern. If the central spot in the far-field is filtered out the near field profile obtained has a spatial frequency which is double with respect the one obtained without the filter, as can be observed in (c and d). This analysis indicate that the near-field profile is determine by interference between on-axis plane wave and the tilted waves which, accordingly, are phase locked. This cooperative effect has been already observed in the past in small Fresnel number cavities [Lugiato, 1988]. In addition, this result

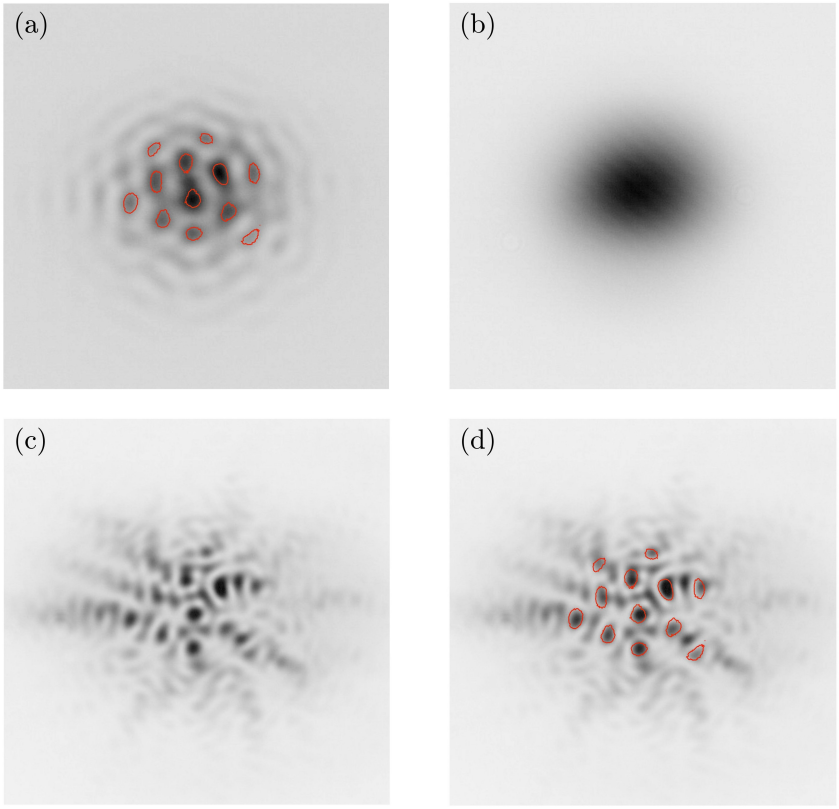

Figure 3.6. (a) Near field distribution with intensity peaks evidenced in color. (b) NF after filtering out the tilted Fourier components of the pattern and leaving only the central spot. (c) NF after filtering out the axial Fourier component of the pattern (central spot in FF). (d) Superposition of the (c) with the peaks of the total pattern identified in (a).

demonstrates also that the correlation length of the hexagonal pattern corresponds to the full extension of the pattern, and indicates that no signature of spatial localization is observed.

Hexagonal structures have been observed in systems where self-organization is mediated by diffraction and a lack inversion symmetry is presented. For example, pumped cavities, single-mirror feedback schemes and counterpropagating beams [Arecchi, 1999; Ackemann, 2001; Ackemann, 2021]. Due to Talbot effect, a phase modulation is transformed into a modulation in the amplitude with a defined period Λ and wave-number $k = 2\pi\Lambda$. This defines a continuous ring in the Fourier space for all the transverse wave-vectors with $|\vec{k}_\perp| = k$. The symmetry breaking allows the selection of only few modes with the same k. For instance, conventional three-wave interaction in a quadratic media, where the pattern defined by two wave-vectors $\vec{k}_1$ and $\vec{k}_2$, both with the same amplitude k, there is a nonlinear interaction between them where a third wave-vector $\vec{k}_3$ appears such that $|k_1| + |k_2| + |k_3| = 0$. A full theoretical model is on going in order to describe the origin of this effect in our system. As it is described in

the following section, aberrations play an important role in our system, then high order diffraction effects arise close to SIC that can lead to the nonlinear coupling with the SESAM allowing the modulation in the amplitude, as it was mentioned.

3.3.1 Time-localized patterns

The temporal behavior of these patterns depends critically on the tuning between the gain emission and the absorber, *i.e.* $\delta\lambda = \lambda_{SA} - \lambda_G$. For $\delta\lambda < 4.5$ nm the VECSEL does not reach lasing threshold at maximum pump power, due to the amount of saturable losses (more than 16%). In the range of $4.5\,\text{nm} < \delta\lambda < 8$ nm the VECSEL features, in a large range of pumping levels, multi-stability between a set of mode-locked pulsating states. For $\delta\lambda > 8$ nm, the pulsating solutions become unstable with appearance of pulses with random timing and peak intensity. In figure 3.7, we present the temporal

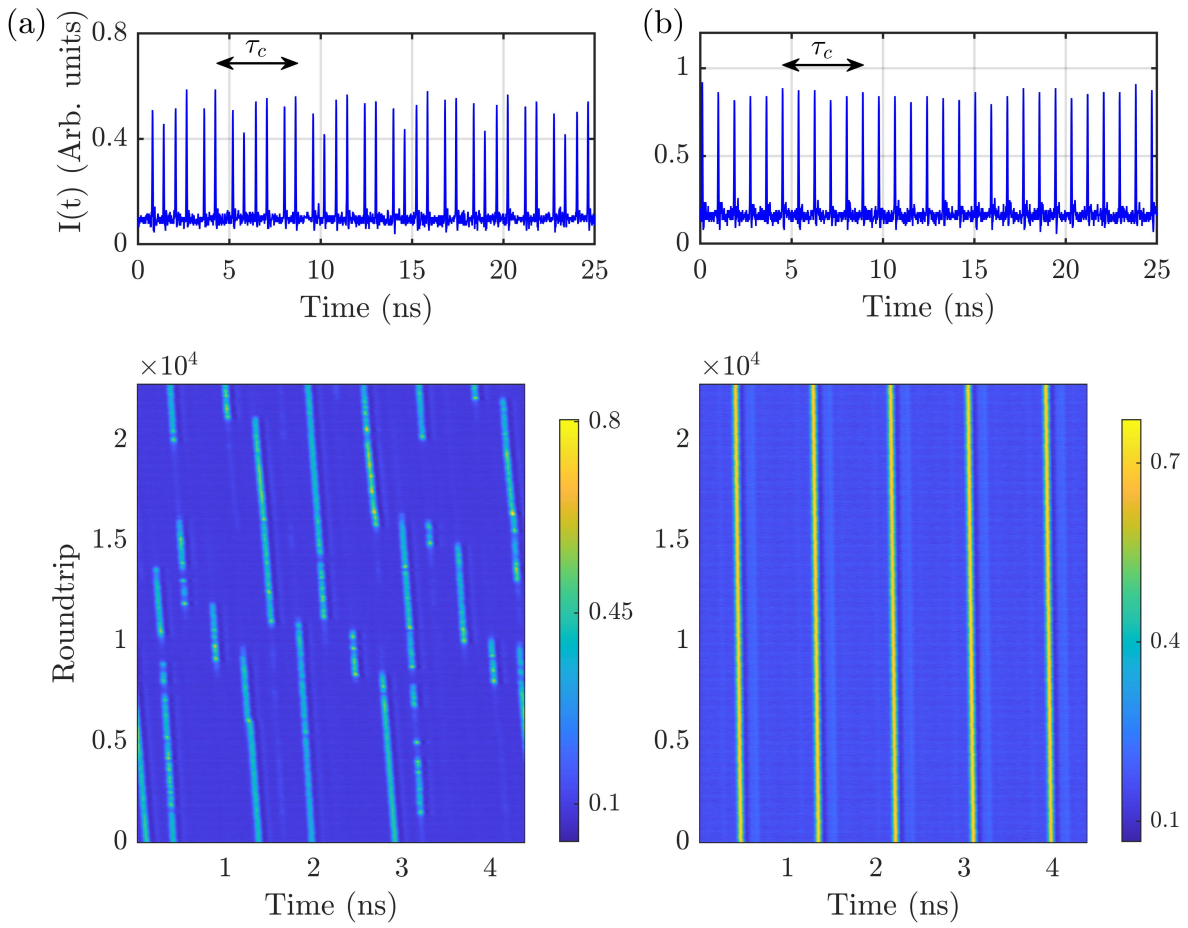

Figure 3.7. Temporal dynamics for (a) random and (b) PML pulses. The upper panels show the temporal traces for few round-trips. The lower ones are the spatio-temporal map in terms of the round-trip time.

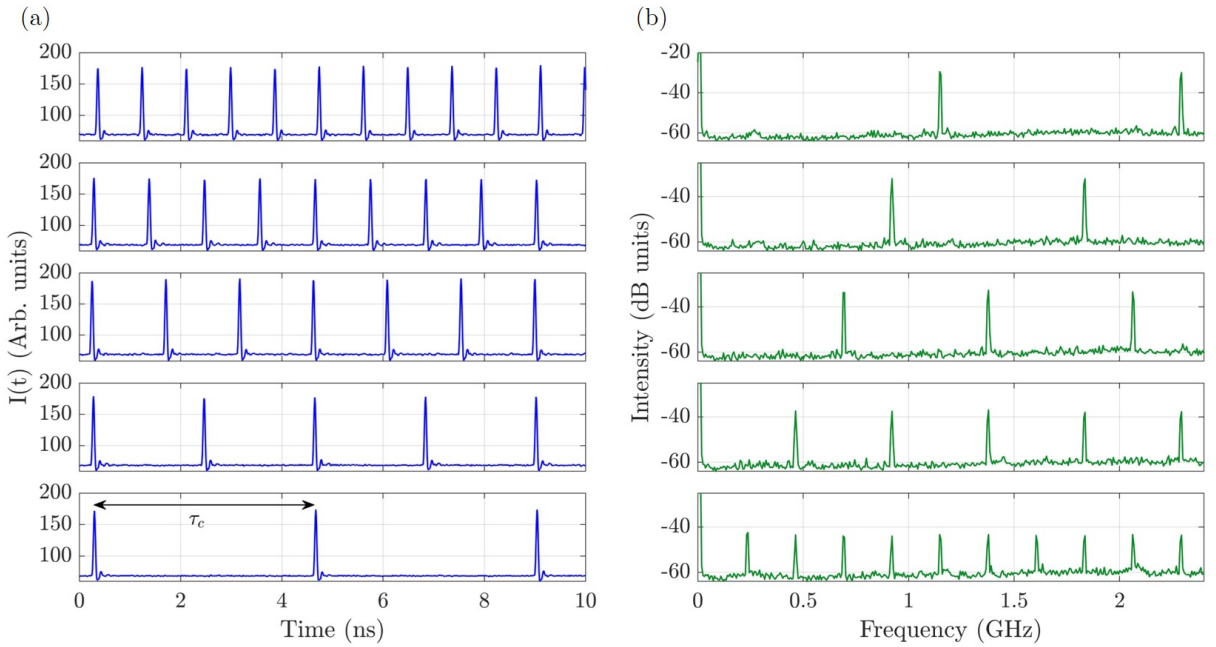

Figure 3.8. (a) Multistability of the pulsing states for the on-axis pattern when $P_p = 312mW$ and $\delta\lambda$=4.5 nm and (b) its corresponding power RF spectrum.

dynamics of the last two regimes. In the upper row, the time series are shown, while the lower row depicts the so-called space-time diagrams, where the time trace is transformed into a two-dimensional representation with a folding parameter equal to the cavity round-trip time τ_c.

In the multistable regime, there is a coexistence of solutions with different number of pulses per round-trip N ranging from 0 to 5. Figure 3.8 a) shows the time traces of coexisting solutions for a pump value of 312 mW. The off solution, not shown, coexists also with all of them. The time series shown in Figure 3.8 a) correspond to the temporal behavior of the pattern described in panel B of figure 3.3. In panel b we show the corresponding power RF spectrum of each trace. The cavity free spectral range is about $\Delta\nu = 230$ MHz, and defines the separation of the peaks in the power spectra when $N = 1$. This separation increases depending on the number of pulses in the cavity with $N \times \Delta\nu$. The power spectrum lines width is limited by the power spectrum analyzer resolution (1 kHz, FWHM).

We study the stability of each solution as a function of the pump power, as it is presented in the bifurcation diagram of 3.9a. We vary P_p from zero to the lasing threshold $P_t = 318$ mW, where the off solution losses its stability and jumps into a the $N = 5$ mode-locked state. Then when decreasing P_p, such state remains up to P_p =295 mW for jumping to the solution $N = 4$, which is seen as a drastic change in

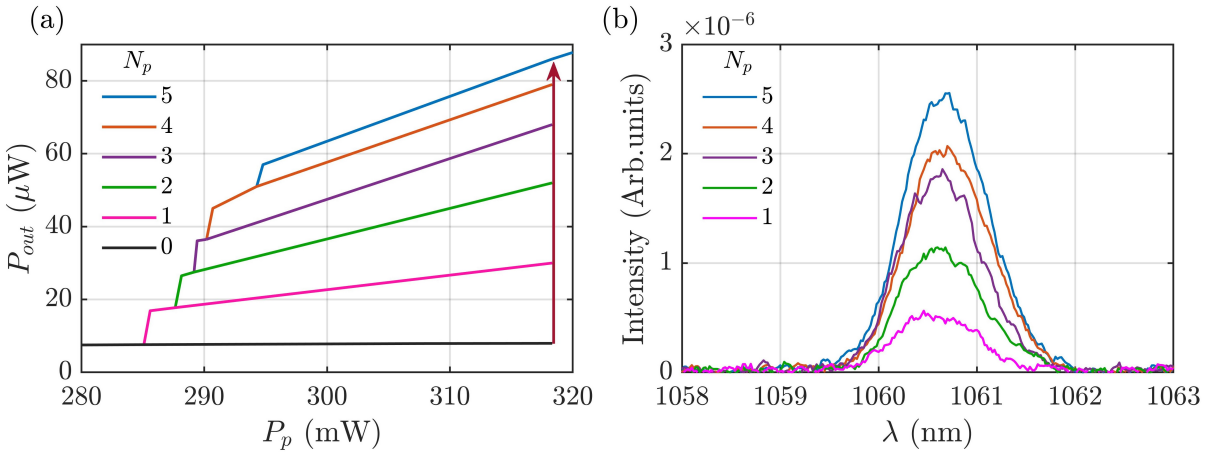

Figure 3.9. (a) Multistability of the pulsing states for the on-axis pattern when $P_p = 312mW$ and $\delta\lambda$=4.5 nm and (b) Bifurcation diagram showing the stability of each branch from $N = 1$ to 5 and (c) its corresponding wavelength spectrum.

the output power P_{out}. For this new solution, the pump power is increased up to P_t, and then decreased again until the solution losses its stability and jumps to the state $N = 3$. This process is repeated again until the off-solution is achieved at $P_{off} = 285$ mW. This multistability is an indication that the system is operated in a temporally localized mode-locked regime. For the solutions with 1, 2 and 3 pulses we observe the individual pulse energy remains the same, since the jumps between each branch are around the same value. For the solutions with higher number of pulses, the energy starts to be reduced, probably due to an incomplete gain recovery between pulses. The optical spectrum analyzer (OSA) indicates that the FWHM of the wavelength spectra remains the same for all the solutions, with a value of $\Delta\lambda \approx 1$ nm. These wavelength spectrums are presented in figure 3.9 b). An additional information to point out is that, when changing P_p changing the number of pulses per round-trip, the pattern emitted does not exhibit changes in its spatial distribution but only in intensity.

This general multistability is the signature of temporally localized structures (TLS); each one of the pulses circulating in the cavity may be addressed by a perturbation pulse in the optical pump, as we will demonstrate in follow.

3.3.2 Addressing of temporal localized states

Previous manipulation of TLS was realized in an electrically biased VCSEL [Marconi, 2014a; Camelin, 2016], and it was performed by adding a tailored electrical signal to the CW pumping current. The repetition rate of the perturbation needs to be strictly resonant with the cavity round trip time τ_c to avoid walk-off of the perturbation. The

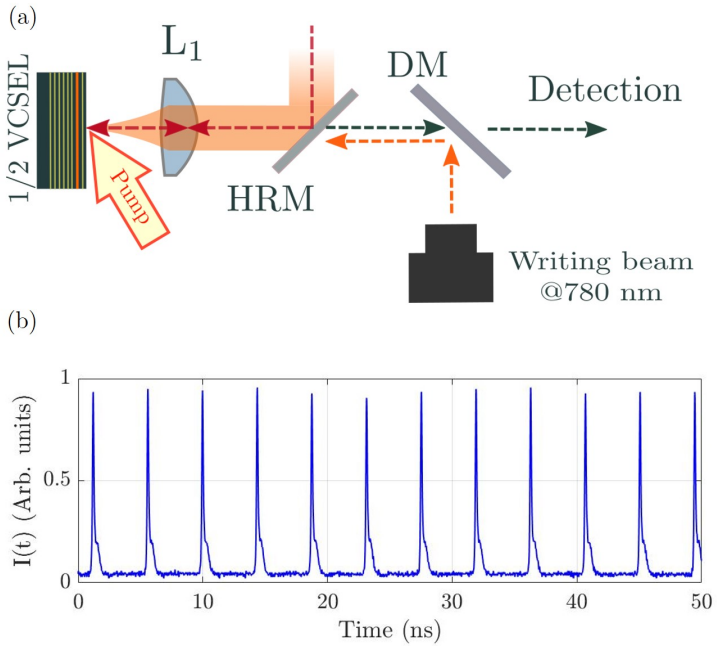

Figure 3.10. (a) Setup for writing beam injection. A small @780 small pump was sent to the gain facet via a dichroic mirror (DM), which does not filter the light coming out the cavity. (b) Optical pulses generated from the second @780 nm pump.

.

duration of the pulse needs to be shorter the gain recovery time to be able to target a single TLS. Finally, the perturbation was required to be applied for a few thousands of round-trips in order to switch on and off successfully a TLS.

Our VECSEL is an optically pumped system and the pump laser is not suitable for fast modulation. Hence, we use of an external optical perturbation generated by a single transverse mode, 780 nm diode laser mounted in a package allowing for fast modulation. The perturbation beam was injected onto the gain mirror through the HRM output coupler using a long-pass dichroic mirror (cut off > 980 nm) in the detection line (see scheme in Figure 3.10). Such beam exhibits on the surface of the gain mirror a Gaussian circular profile 13 μm waist (at $1/e^2$). The addressing pump laser was controlled by an electrical pulse generator which enables optical pulses of $\sim$ 120 ps duration at a repetition rate matching the external cavity round-trip time τ_c. We show in figure 3.10 b) a train of these addressing pulses.

The system is prepared in the multi-stable parameter region (285 mW $< P_p <$ 318 mW) where TLSs exist and the amplitude of the addressing pump pulse is chosen to be sufficiently large (pulse peak of 10 mW measured on the gain section) to bring the system locally above the upper limit of multi-stable region where only 5-pulses per round-trip solution is stable. Because the pump pulse is sufficiently short, a simple TLS

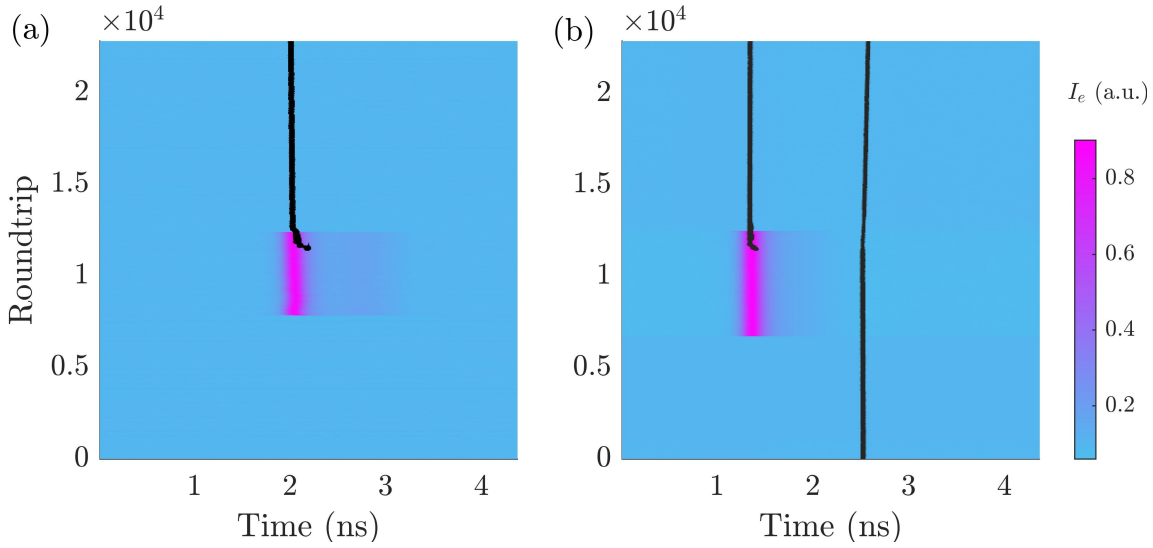

Figure 3.11. Spatio-temporal map of (a) the pulse creation (black) and remaining after the perturbation (color) is turned off, and (b) the creation and addressing of such pulse when a temporal LS is already existing in the cavity.

will be excited when the perturbation is applied. As expected, the TLS remains after the perturbation is removed. In figure 3.11 we illustrate the writing operation using a current pulse applied between round-trip $n_1 = 7800$ and round-trip $n_2 = 12500$. In panel 3.11a, we choose an initial condition where no LS is present inside the cavity before the addressing pulse. In panel 3.11b we repeat the operation with a LS already existing in the cavity before the addressing pulse. A second Ls is switched on after the addressing beam, while the first LS remains without being affected. Other initial conditions can be chosen with similar results, provided that the addressing pulse is separated in time from the preexisting LS of at least τ_g. Even when we did not perform a quantitative study, we observe that the perturbation needs to be applied for a minimum number of round-trips (few thousands at least) for a successful switching of a TLS. Moreover, it was not possible to decrease the size of the perturbation beam below 13 μm waist (at $1/e^2$) and maintaining a good control of the switching process.

3.3.3 Spatial correlation

Close to SIC, in presence of a broad-area flat top pump profile, we may expect the occurrence of spatially localized structures, possibly related to the observed TLS. For detecting the presence of these spatio-temporally localized structures, we have developed a spatio-temporal detection system by using an array of 8×8 fibers of 60 μm core diameter and 120 μm separation core to core. The array was placed in the conjugate plane of

the gain mirror on the detection path (scheme 3.12a), with a magnification that allows for monitoring the smallest area of the pattern compatible with the sensitivity of the detector used. For visualizing the position of these fibers receptors with respect to the gain mirror facet, a @1060 nm CW laser beam was coupled into the output facets of two neighbour fibers, fed back by the gain mirror facet and imaged onto the near field detection camera. Hence, the position of the fibers core on the gain mirror facet can be established together with the area of the pattern monitored by a single fiber ($\sim 5\ \mu$m, as shown in figure 3.12 b)).

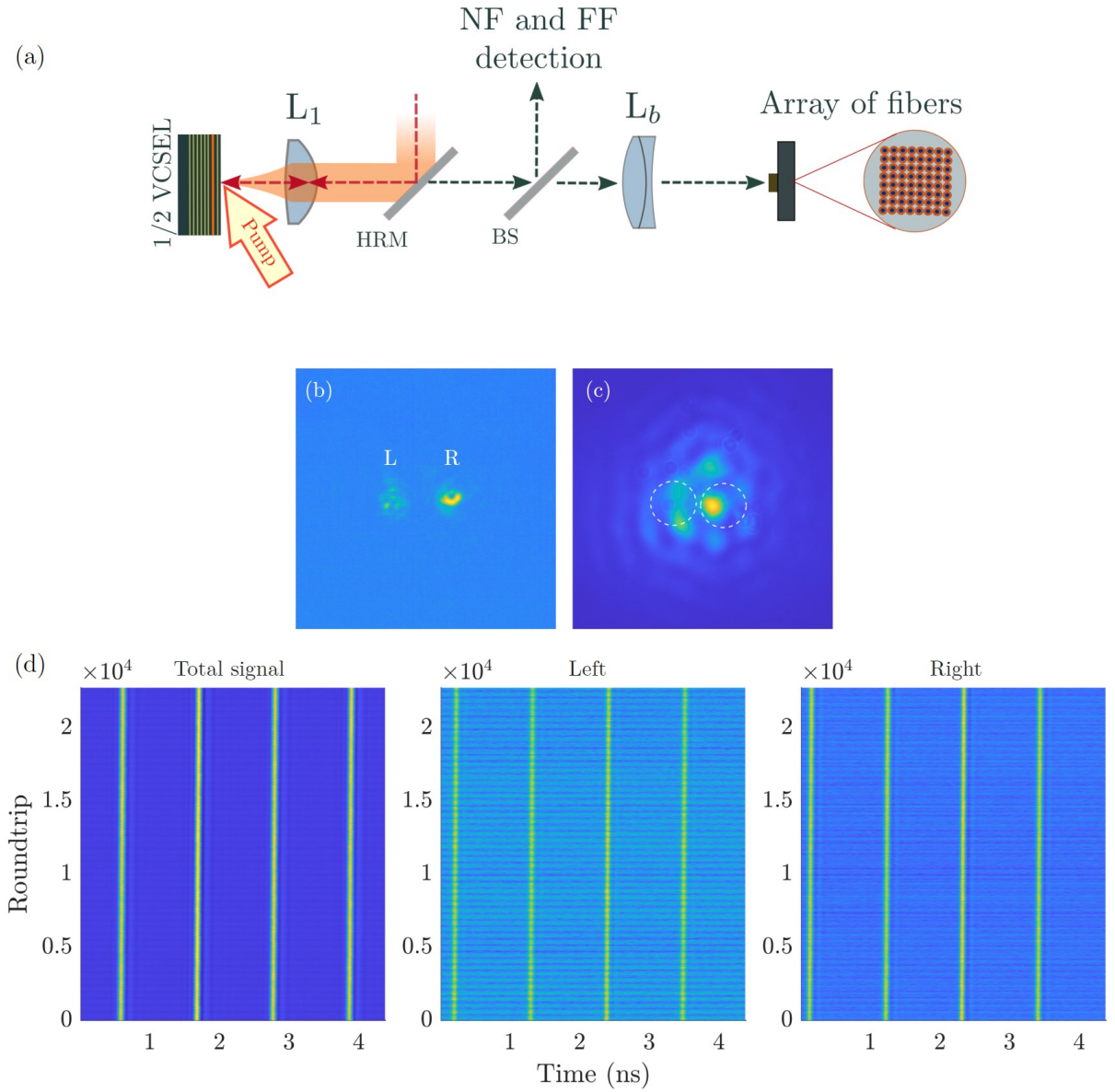

Figure 3.12. (a) Imaging system for the spatio-temporal resolved detection using an array of 8×8 fibers of 30 μm core diameter. (b) Image on the gain section of two different fibers of the array, when a @1060 nm laser is sent through them. (c) Pattern solution detected by two fibers (dashed lines). (d) Spatio-temporal maps of the total intensity, the left and the right fiber detection, showing the spatial correlation along the pattern.

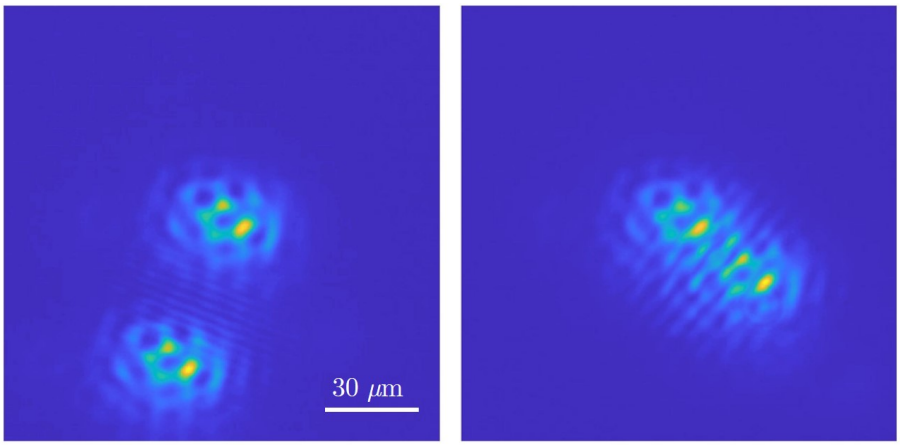

Figure 3.13. Emission profile at the output of a Michelson interferometer. a) The splitted beam profiles are not overlapped, b) the beam profiles are partially overlapped and they interfere.

The signal collected by these fibers was sent to the Oscilloscope with photo-detectors for the observation of their individual temporal dynamics. We have characterized the spatio-temporal emission of the VECSEL when operated in the TLS regime described above. In figure 3.12 c) we show the pattern emitted by the VECSEL with the position of the detecting fibers marked in dashed line. The temporal traces on the total signal and the two different fibers exhibit the same temporal dynamics, as it is presented in the spatio-temporal maps on panel 3.12c. We scanned all long the pattern, using different solutions of N, obtaining the same result. Therefore, we conclude our system is spatially correlated. This was also confirmed via an interferometric measurement of the pattern profile. The output beam was sent to a Michelson interferometer, splitted in two and then recombined overlapping distant parts of the patterns. Interference fringes appear, as shown in Fig. 3.13, thus indicating that spatial coherence is extended to the full pattern and that the field emitted exhibits a perfect correlation on the entire size of the emission.

3.4 Case $C > 0$

When our VECSEL is operated in the regime of $C > 0$ ($d_2 < f_1 + f_2$, then $\Delta z < 0$), Gaussian emission gives way to pattern emission when increasing the distance from the SESAM to L_4, as shown in fig. 3.2 In figure 3.14, the near-field and far-field profiles evolution of the emitted pattern is presented as a function of x, in the situation where $\Delta z = -2.74$ mm. For the smallest values of x, the system emmits the Gaussian mode solution (panel a-D), whose waist is marked in the curve 3.2. On the other hand, when

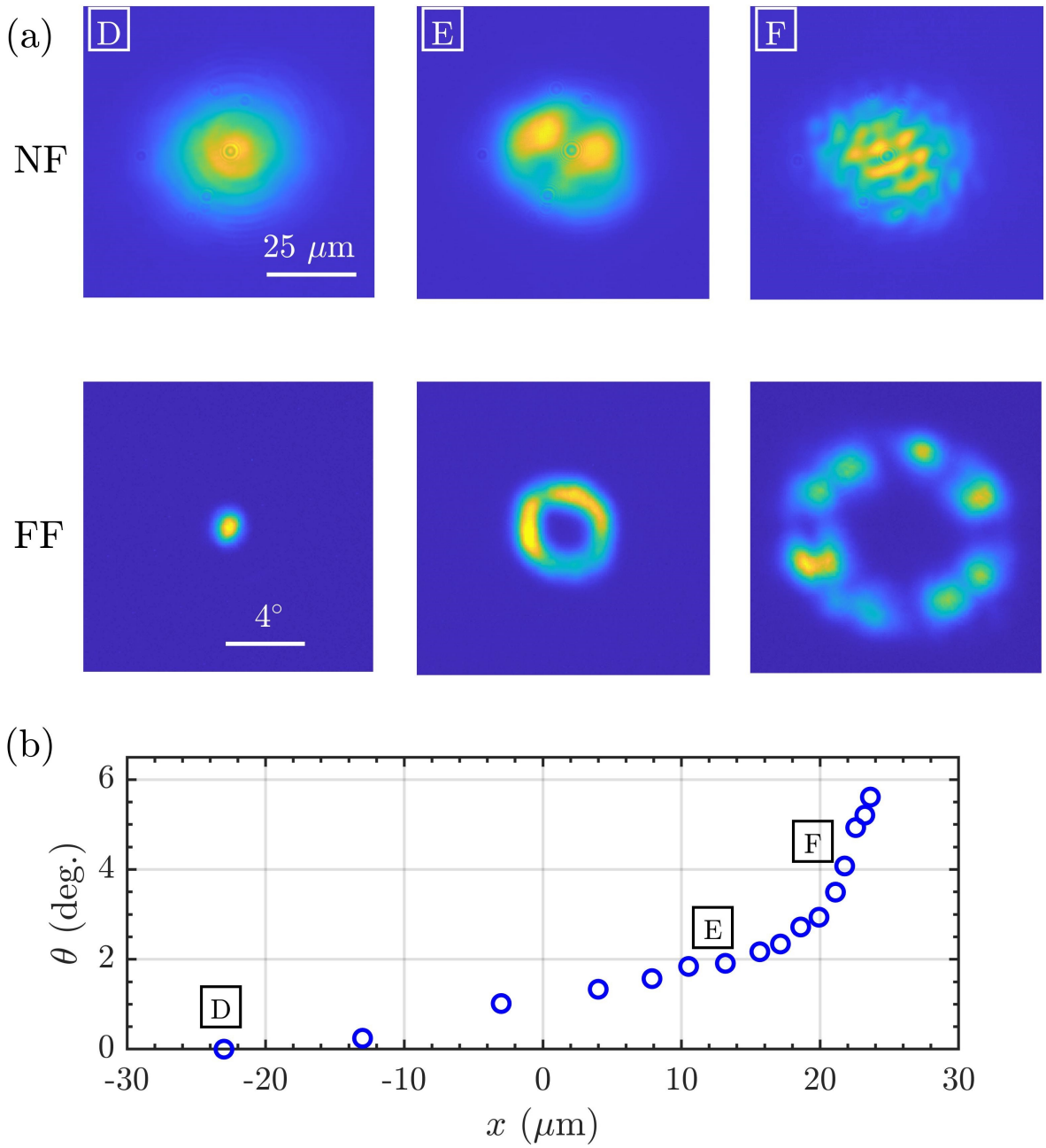

Figure 3.14. Pattern evolution as a function of x, when P_p = 202 mW. (a) The change on angle in the far field, versus the SESAM position. In (b) it is shown the averaged intensity profiles of the NF (up) and FF (low), for some cases marked with capital letters as a reference on (a)

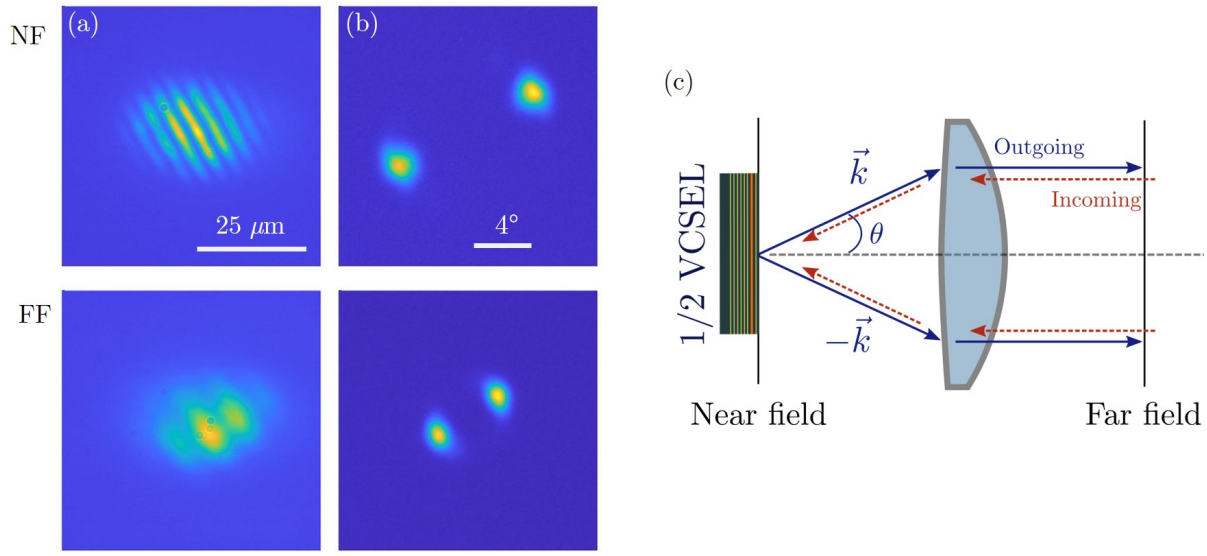

Figure 3.15. NF and FF of a pair of counterpropagating tilted waves for angles (a) 5° and (b) 3.5°. c) Conceptual scheme explaining the rolls observed in the near field generated by a pair of tilted waves with opposite transverse wave vector $\pm\vec{k}_\perp$.

$\Delta x < 20\mu$m the far-field profile indicate a transverse k- vector ($\vec{k}_\perp$) distribution in form of a ring (Fig. 3.14a) panels E, F), without any component in the direction of the cavity axis. The radius of this ring-like far-field, i.e. the modulus of $\vec{k}_\perp$, increases as $\Delta x \to 0$ (Fig. 3.14 b)) and, correspondingly, the spatial frequency of the near-field profile increases (Fig. 3.14a) panels E, F). Maximum angle observed is close to 6°, and correspond less than half the limit of the numerical aperture (θ_{max}). In addition, the ring observed is slightly elliptical, due to the ellipticity of the pump.

The system is emitting a set of tilted plane-waves $\vec{k}$ having transverse components in different directions but all sharing the same module. This circular symmetry is rather fragile and can be broken by inserting an anisotropic element in the set-up (as a glass window) or simply by slightly tilting the SESAM. Then, the circle in the far-field breaks up in spots (Fig. 3.14 a)) panels F) and, quite often, only two spots are left, as shown in figure 3.15. These spots in far field appear in pairs: each transverse wavevector $\vec{k}_\perp$ appears always together with the opposite transverse wavevector $\vec{k}_\perp$.

By blocking the component $\vec{k}_\perp$ in the cavity, the emission at $-\vec{k}_\perp$ is also removed. We conclude that the system is emitting two counterpropagating tilted plane-waves, each one leaving the gain section with a transverse wavevector, say $\vec{k}_\perp$, and coming back after traveling in the cavity with the opposite transverse wavevector $-\vec{k}_\perp$, as shown in Fig. 3.15 c)). These two waves interfere giving birth to fringes onto the surface of the gain section and of the SESAM (as shown in the near profiles of Fig. 3.15). The thickness of

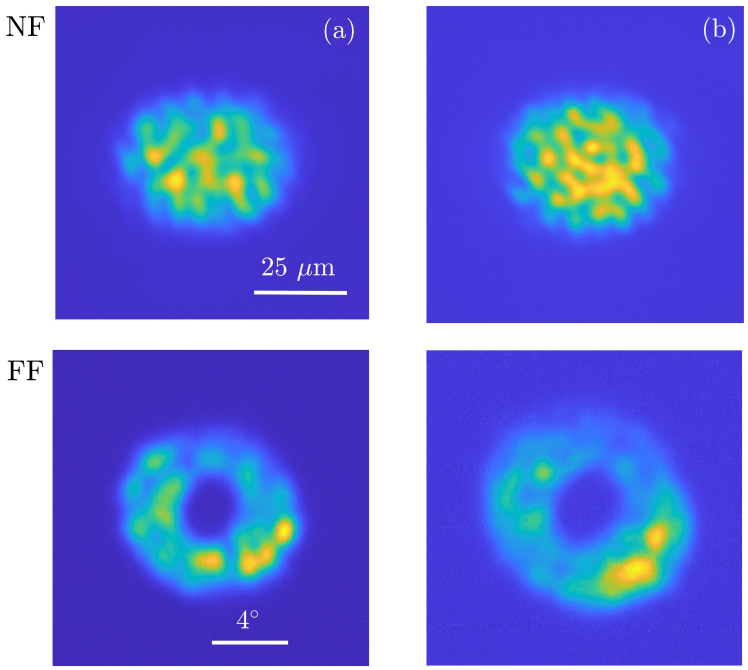

Figure 3.16. (a) and (b) correspond to patterns at high gain, $P_p = 235$ mW, and the density on the ring at the FF increases.

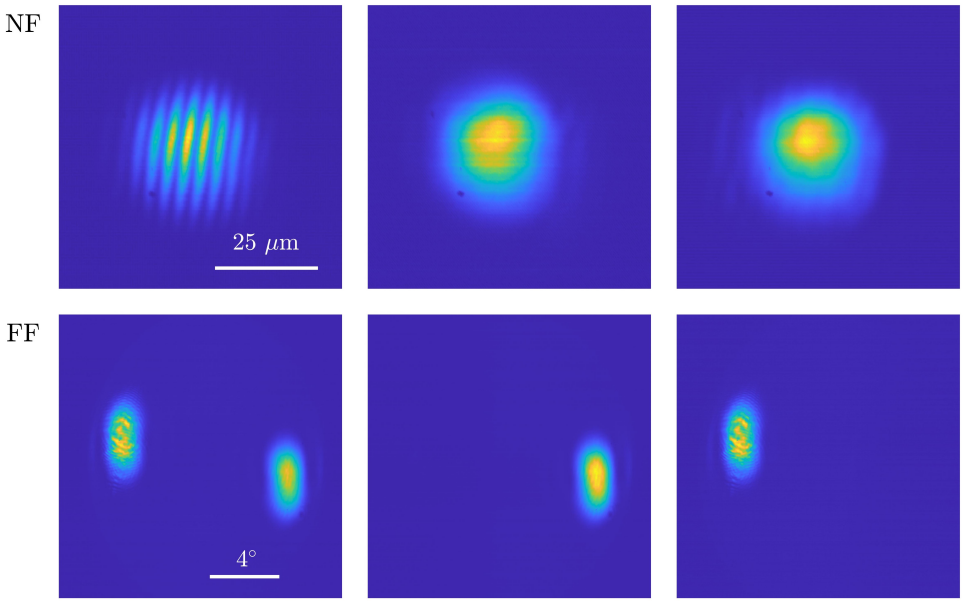

Figure 3.17. Far field filtering for a tilted wave of 4°. Panel (a) shows FF of a pair of counterpropagating titled waves and its Fourier transform (near field) In (b) and (c) the components with $\vec{k}_\perp$ and $-\vec{k}_\perp$ are blocked, respectively in the FF plane and the Fourier transform shows the near field of a single tilted wave.

the ring-like emission observed in the far field, i.e. the band of ($k_\perp$) emitted, increases with pump power as shown in figure 3.16 a)-b).

For examining the intensity profile of a single pair of tilted waves circulating in the cavity we may filter one of the two spots in a far-field plane in the detection path, as we did for the patterns observed in the case $C < 0$ (Fig.3.6). The transmitted beam is then imaged onto a CCD camera. The near and far field profiles of a single titled wave are presented in figure 3.17. In panel a the near field profile presents stripes due to the interaction of two tilted waves with an angle 5°. Panels b and c were obtained by blocking one of the tilted wave in the far field detection. The profile of the single tilted wave is Gaussian, exactly as on-axis Gaussian modes. This suggests the interpretation of the tilted wave emission in terms of an off-axis Gaussian beam following a loop around the optical axis, as we will show in the section 3.4.3.

3.4.1 Time localized Tilted Waves

As it was demonstrated in section 3.3.1, the temporal dynamics of these patterns will depend of the the detuning $\delta\lambda = \lambda_{SA} - \lambda_G$. The three different behaviors observed for the case $C < 0$, namely, no lasing, multistable mode-locking and unstable pulsating case, were observed as well for $C > 0$. Noteworthy, the value of the micro-cavities resonance

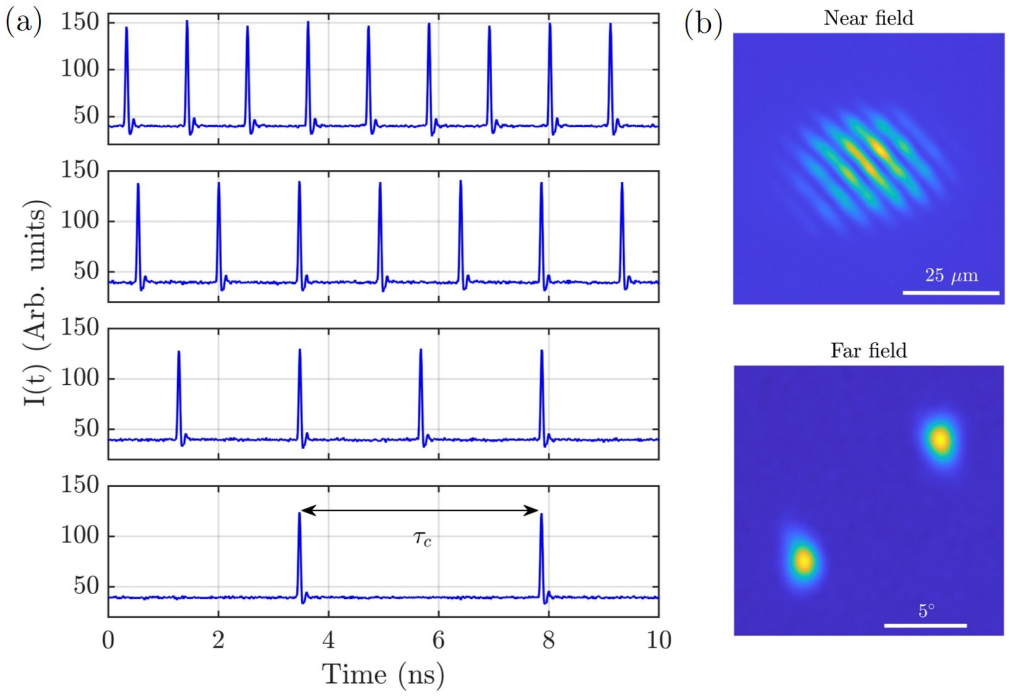

Figure 3.18. (a) Coexistence of multiple solutions $N = 4, \cdots, 0$ when $P_p = 175$ mW. (b) Near and far fields of the pattern structure.

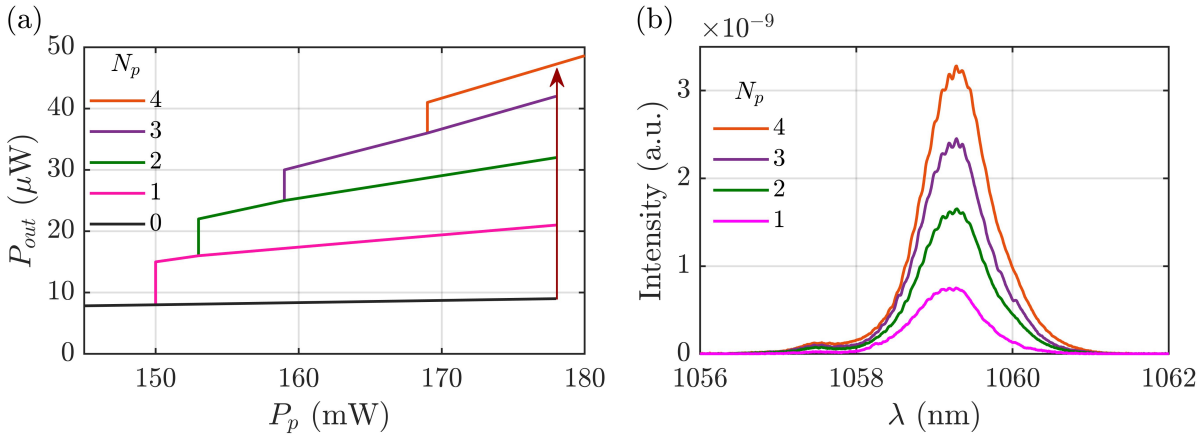

Figure 3.19. (a) Bifurcation diagram of the stability of each solution and (b) wavelength spectrum for each branch.

changes with the incidence angle according to

$$\lambda = \lambda_{\theta=0}\sqrt{1 - \frac{\sin^2\theta}{n^2}} \tag{3.1}$$

with n the effective refractive index of the SESAM. This implies that for the tilted waves situation there is a blue shift on the resonance of 0.03% (0.3 nm)for $\theta = 5°$ and 0.16% (1.6 nm) for $\theta = 10°$. Because of the magnification factor, the angle of incidence of the tilted wave onto the SESAM is the double of the one on the gain surface. A tilted wave with $\theta = 5°$ onto the gain will experience a net decrease of the detuning of 1.6 nm, implying the VECSEL threshold will be achieved for $\delta\lambda > 2.8$ nm.

We have operated the VECSEL in the range 5.5 nm $> \delta\lambda >$ 4 nm which allows to reach the threshold value within the power range of our pump ($P_p < 350$ mW) and, at the same time, it determines a wide multistability between different mode locked states having a number of pulses per round-trip ranging from $N = 1$ up to 4 (figure 3.18).

The stability of each solution can be obtain by tuning the pump power, and it's shown in the bifurcation diagram on figure 3.19a). We increase P_p from zero to the lasing threshold $P_t \sim 178$ mW and the solution with $N = 4$ pulses per round-trip appears. This remains for about 10 mW below the threshold and jumps into the solution with $N = 3$ pulses per round-trip appears. This is seen as a sudden jump in the output power (P_{out} of about 5 mW. For this new solution, the pump power is increased up to P_t and decrease again until it jumps to the solution with $N = 2$ pulses per round-trip appears. This process is repeated until achieve the off solution. This suggest that the system is operated in the regime of temporal localized structures, where up to 4 pulses per round-trip can be stored in the cavity. For $N = 1$ and 2, the individual pulse energy

remains the same, while for more pulses starts to decrease. Finally, the optical spectrum analyzer indicates that the FWHM span of $\Delta\lambda = 1$ nm, and this is independent from N (see figure 3.19 b)).

3.4.2 Controlling and addressing of time localized Tilted waves

Temporal localized structures can be independently addressed by sending perturbation pulses into the cavity. As we have done for the patterns observed in the case $C < 0$, we have repeated the operation for the temporal localized tilted waves observed for $C > 0$. As for $C < 0$ this beam was pulsed at a repetition rate equal to the cavity free spectral range an with a pulse width (FWHM) of ~ 120 ps. The peak power of the pulse measured inside the cavity is 10 mW. In figure 3.19, we show the addressing procedure of a pulse inside the cavity starting from the situation when no pulses are present. The process is represented by a spatio-temporal like diagram exactly as we did for the case $C < 0$. Here, the position in the gain mirror section targeted by the (narrow) address beam is important for a successful addressing. One must target the region where, at the switching, a bright fringe will appear in the near field as a result of tilted wave emission. This is shown in figure 3.20 a)) where we show the near field emission when perturbation is applied and after perturbation removal. The position of these fringes is fixed by the position of the optical elements which, as explained above, determines the angle of the transverse k-vector. If one targets the region in between two fringes no switching is observed. The perturbation pump beam is required to have a minimum waist comparable to the size of one of the fringes. In Fig. 3.20 the addressing process was possible with a 8 μm waist perturbation pump beam.

As for $C < 0$, for switching on the pulse into the cavity and for its survival after the perturbation pulse is removed, it is necessary to send the perturbation pulses for few thousands of round-trip (In Fig. 3.20 b)) between the round-trip $n_1 = 10800$ and $n_2 = 15400$). In Fig 3.20 b)) the perturbation is applied slightly asynchronously with the cavity round-trip and it experiences a walk off inside the space-time diagram. It is interesting to note how the localized pulse follows the perturbation and, once this is removed, it evolves with the timing imposed by the round-trip. In Fig 3.20 c)) a perturbation is applied for a limited number of round-trips (between $n_1 = 10900$ and $n_2 = 12000$), a localized pulse is generated but, between the round-trips $n_3 = 16600$ and $n_4 = 17700$ a second perturbation is applied at a different position. This perturbation generates a second localized pulse before the first one. The two pulses are too close and

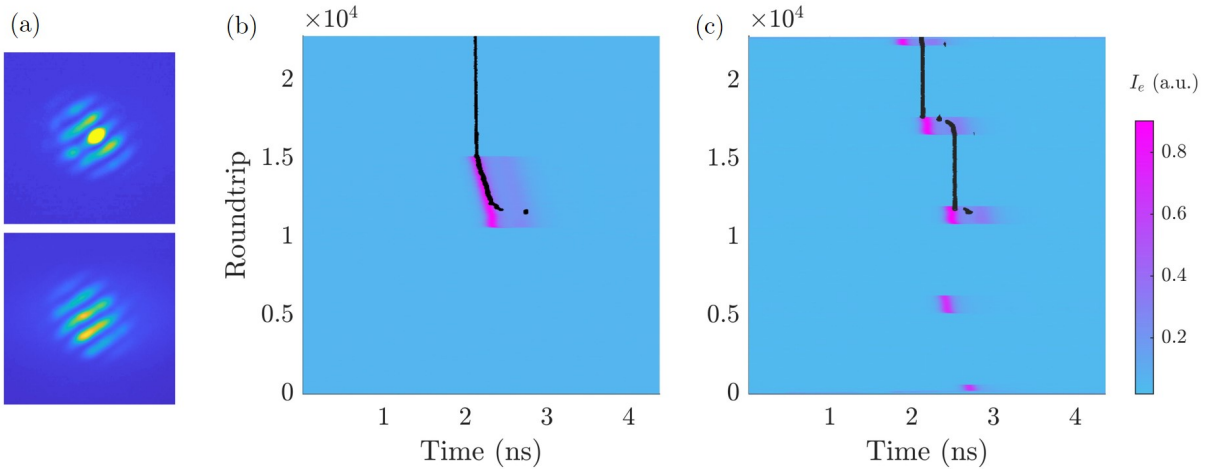

Figure 3.20. (a) NF of the stripped pattern when the perturbation, located in one of the stripes' maxima, is on (up) and (off). Spatio-temporal map of (b) showing how a TLS (black trace) in the cavity is turned on when the perturbation pulse is applied between the round-trip $n_1 = 10800$ and $n_2 = 15400$ and how it survive after perturbation removal, (c) perturbation pulses are sent in burst of few hundreds of round-trips. Perturbation drifts in the space-time diagram and at the burst at round-trip 16600 it appears before TLS, thus switching it off and making it appeared shifted within the cavity.

the first one eventually dies.

3.4.3 Origin of Tilted Waves

Tilted Waves have been observed in the past in laser systems with high Fresnel number. For instance in 1999, Hegarty and coworkers observe similar periodic structures in the surface of a native oxide confined VCSEL, whose far field correspond to equidistant off-axis spots [Hegarty, 1999]. According to models based on Maxwell-Bloch equations, the spatial emission depends on the detuning between the peak of the gain curve (ω_a) and the cavity resonances of the system, $\delta\omega = \omega_a - \omega_c$. For negative detuning, the VCSEL emits tilted waves with a transverse wavevector $\vec{k}_\perp$, for which $\vec{k}_\perp + \vec{k}_{axial} = \vec{k}$ and the wavenumber k is resonant with the gain curve while the axial component of the wavevector $\vec{k}_{axial}$ enables resonance with the optical cavity. The same tilted wave emission were observed by Hachair and coworkers, in a CW VECSEL composed by a one lens and a concave mirror, when tuning the parameters B and C [Hachair, 2008].

In our experiment, this explanation of tilted wave emission due to matter-wave interaction does not apply. Our external cavity (whose FSR is only 250 MHz) provides a dense set of modes which ensures axial resonance with any other frequency dependent response curve of our system as the gain curve (wider than 20 nm) or as the micro-cavities frequency filtering (the sharpest is the gain mirror one which is few nm wide,

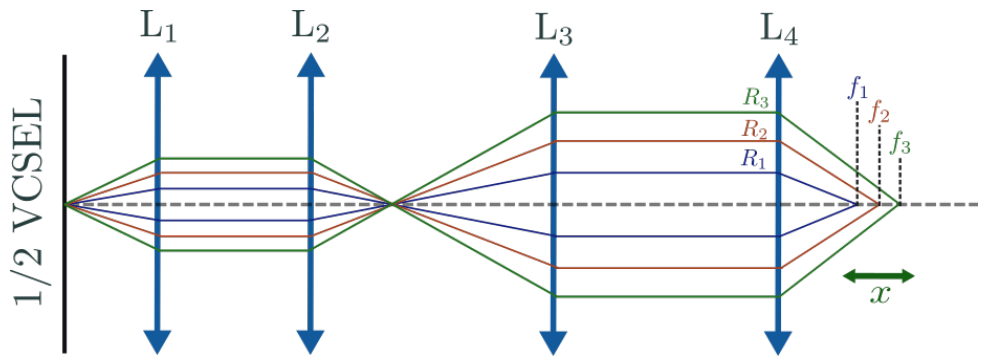

Figure 3.21. Off-axis closed loop scheme for different tilted waves. The focal point $f(R)$ of L_4 is a function of the off axis position R of the tilted wave chief ray.

i.e. few hundreds of GHz wide). Moreover, we have verified that the angle of the tilted waves emitted was not depending on any parameter of the active or passive media (temperature, pumping). As shown in Fig. 3.14, this angle depends instead on the distance between the SESAM and its collimator L_4.

In our system, the origin of tilted waves can be understood by considering spherical aberrations from our cavity imaging system. As shown in Figure 3.17, tilted waves emission corresponds to off-axis countepropagating Gaussian beam. Moreover, the angle of the tilted waves increases by increasing the distance d_5 between L_4 and the SESAM. The spherical aberrations of L_4 make its focal dependent on the distance R from the cavity axis at which an off-axis beam hits the collimator: $f(R) = f_0(1 + \alpha R^2)$. Accordingly, if $\alpha > 0$, for a range of distances d_5 larger than f_0 there is a set of off-axis Gaussian beams which is stable, as shown schematically in figure 3.21. Obviously, spherical aberration effect becomes evident in our set-up because we are close to SIC and spherical aberrations takes over diffraction[1].

A model including lens aberration, and the temporal dynamics, is under development for a rigorous justification of the origin of tilted waves. However, we can discuss here some arguments that support this interpretation and some relevant literature on aberration.

First, we would like to remember that, in the time domain, for describing the phase $\varphi(\omega)$ of a pulse in the z direction, the phase is expanded as Taylor series of the frequency

[1]At IES in Montpellier, they run similar experiment with a gain mirror, two lenses (two achromatic lenses similar to our L_2 and L_3) for a shorter SIC cavity closed by a mirror. They observe tilted waves emission but the angle of tilted waves increase as the distance between the last lens and the mirror is reduced. In their set up, the sign of α in the aberration function $f(R)$ is negative. These results, both for IES and us, are actually in contradiction with the ZEMAX data provided by Thorlabs. In fact, when looking at Figure 2.15 we were expecting a $\alpha < 0$ and a much weaker spherical aberration. The same discrepancy was concerning the achromatic lenses used in Montpellier. The problem with these specifications is probably related to the fact that these optics are optimally designed for a different optical wavelength. Concerning the Achromatic lenses used at IES, it was possible to obtain a characterization of the wavefront error in these lenses and the value shown were contradicting the ZEMAX data provided by Thorlabs, why they were confirming the estimation realized experimentally by IES.

ω around ω_0 as

$$\Phi(\omega) = \Phi(\omega_0) + \sum_{j=1}^{\infty} \frac{1}{j!} \left. \frac{\partial^{(j)}\Phi}{\partial\omega^{(j)}} \right|_{\omega_0} (\omega - \omega_0)^j, \tag{3.2}$$

with $\omega_0 = ck_0$, the first derivative corresponds to the group delay (GD), the second order is the group delay dispersion (GDD) and so on.

The same treatment applied to the wavefront of the field as the wave propagates longitudinally (z). The wavefront Φ can be expanded in power of the transverse spatial frequencies $k_\perp$. Then, we obtain that:

$$\Phi(k_\perp) = \Phi_0 + D_1(k_\perp) + D_2(k_\perp)^2 + D_3(k_\perp)^3 + ... \tag{3.3}$$

D_1 is related to tilting, D_2 is the diffraction term which, in an ABCD system, reads $D_2 = -B/2k$. In our system, close to SIC, $D_2 \approx -\mathcal{M}\Delta x/2k$ (see equation 2.36). D_3 is related to coma and D_4 represents spherical aberration contribution. For axial symmetry and no tilt, only the even terms are relevant. This development shows that, at SIC condition, spherical aberrations become relevant for the field profile.

We recall that, in paraxial approximation,

$$k_\perp \approx k\theta \tag{3.4}$$

Yoshida and coworkers developed a theoretical study for an off-axis beam passing through a lens L, which provides spherical aberrations [Yoshida, 1975; Yoshida, 1979; Yoshida, 1982]. They wrote the aberration function describing a lens as a function of the distance ρ of the beam respect from the optical axis.

Let's consider a rectangular coordinate system $(\tilde{x}, \tilde{y}, \tilde{z})$ in the image plane of the SESAM, where $(\tilde{x}, \tilde{y}) = (0, 0)$ correspond to the origin at the optical axis, as it is depicted in figure 3.22. We assume an incoming off-axis beam passes orthogonally to the lens L_4 and focuses at a distance d. As in the experiment, we will assume the beam focuses with an angle $\theta = \tan^{-1}(\tilde{y}/\tilde{z})$, at a distance d shorter than f_4. We define a normalize coordinate system, such as

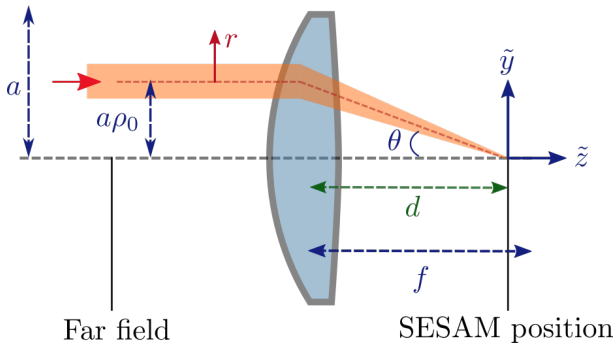

Figure 3.22. Scheme for an off-axis beam passing through a lens [Yoshida, 1982].

$$u = k\frac{a}{f}(\tilde{x}^2 + \tilde{y}^2)^{1/2}, \tag{3.5}$$

$$v = k\left(\frac{a}{f}\right)^2 \tilde{z}, \tag{3.6}$$

$$\psi = \tan^{-1}(u/v). \tag{3.7}$$

If the lens aperture is a, then we define a normalized radial coordinate ρ, such that $\rho = 0$ in the optical axis, and $\rho = 1$ at $\tilde{y} = a$. The incoming beam center is located at (ρ_0, θ_0) in such coordinate system. Let be (r, φ) the normalized polar coordinates reference at the center of the incident beam, and they relate with (ρ, θ) with the transformation

$$a\rho\cos\theta = a\rho_0\cos\theta_0 + ar\cos\varphi \tag{3.8}$$

$$a\rho\sin\theta = a\rho_0\sin\theta_0 + ar\sin\varphi \tag{3.9}$$

We assume that the beam transverse variation is small compared to the lens aperture $r \ll 1$, and since $\rho_0 < 1$, then $r\rho \ll 0$.

When the light passes through an aberrated lens, there is a deformation on the phase wavefront described by $\Phi(r, \varphi)$, called the aberration function [Born, 2013; Yoshida, 1982]. Then the Huygens-Fresnel integral of 2.24 is rewritten in polar coordinates as

$$U_2(u, v, \psi) = \int_0^{2\pi}\int_0^{\xi} \exp\left[ik\Phi(r, \varphi)\right]\hat{K}' U_1(r, \varphi) r\, dr\, d\varphi, \quad \text{where,} \tag{3.10}$$

$$\hat{K}' = \exp\left[-i\left(vr\cos(\varphi - \psi) + \frac{u}{2}(r^2 + \rho_0^2 + 2\rho_0 r\cos\varphi)\right)\right] \tag{3.11}$$

For longitudinal focal shift and astigmatism the aberration function is written as [Yoshida, 1978]

$$\Phi(\rho, \theta) = D\rho^2 + A\rho^2 \cos^2(\theta) \tag{3.12}$$

In our system, a given tilted wave having a transverse component in the Fourier space $k_\perp$ experience focal shift accordingly, with $\rho = d\theta = dk_\perp/k$. This aberration affects the second order term in the wavefront and it changes the condition for observing $B = 0$. Furthermore, we know from Chapter 2 the lens mostly contributing to aberration is L_4, which, because of the magnification factor, is challenged by beams at the largest distance from the optical axis. Hence, an off axis beam whose chief ray intercept L_4 at a distance from the axis $B = 0$ sees its SIC verified not for $\Delta x = 0$ but rather for a Δx value corrected by longitudinal focal shift. Hence, as shown in Fig. 3.21, there is a whole family of off-axis beam which is stable upon shifting of the SESAM.

The beam profile around each chief-ray hitting L_4 at ρ_0 experiences third-order spherical aberrations [Yoshida, 1976]:

$$\Phi_4(\rho) = S\rho^4 = \frac{S_{11}}{8}\rho^4. \tag{3.13}$$

where S is the third-order spherical aberration coefficient that can be expressed by Seidel coefficient $S_{11} = 8S$. With the transformations of 3.8, we can rewrite 3.13 as

$$\Phi_4(r, \varphi) = S\rho_0^4 + 4S\rho_0^3 r\cos\varphi + 2S\rho_0^2 r^2(2 + \cos 2\varphi) + 4S\rho_0 r^3\cos\varphi + Sr^4. \tag{3.14}$$

The first term is a higher order correction to the focal variation experienced by the off-axis chief ray. For axial symmetry the main contribution to spherical aberration is at $O(r^2)$, and corresponds to the defocus of the beam as a function of the θ. From the diagram 3.22, we know $a\rho_0/d = \tan\theta \approx \theta$ in the paraxial approximation. Then we can write

$$O(r^2) = 2S_{11}\left(\frac{\theta d}{a}\right)^2(2 \pm 1), \tag{3.15}$$

where + is for the saggital plane at $\varphi_{\tilde{x}} = \pi/2$ and − for the tangential plane $\varphi_{\tilde{y}} = 0$.

Then the matrix corresponding to L_4 "seen" by the beam profile around each chief-ray at ρ_0 can be rewritten as

$$\begin{pmatrix} 1 & 0 \\ -\frac{1}{f_4} + \frac{1}{\delta f(\theta)} & 1 \end{pmatrix} = \begin{pmatrix} 1 & 0 \\ -\frac{1}{f_4} + \delta C(\theta) & 1 \end{pmatrix}. \tag{3.16}$$

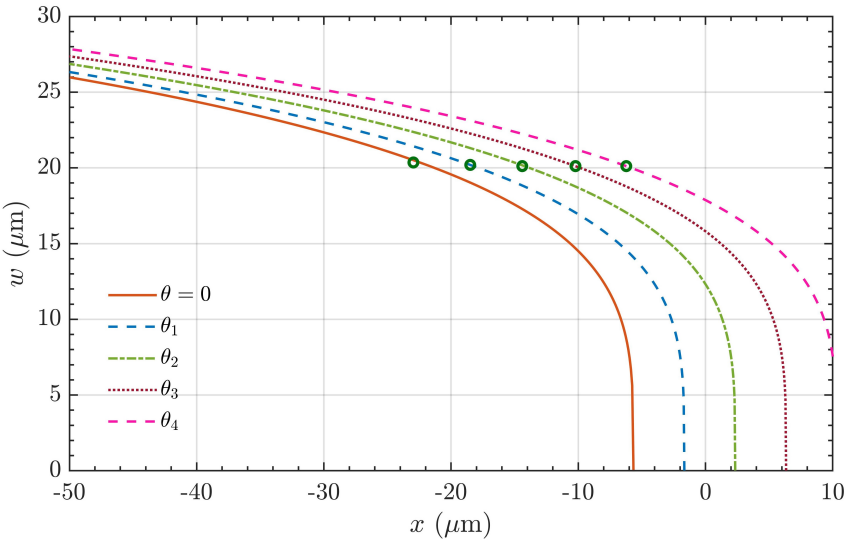

Figure 3.23. Waist evolution for different θ values, where $\theta_1 < \cdots < \theta_4$, for positive aberrations. The green markers depicts the waist value w_i for each x_i, where the ring cavity is closed.

For each θ, there will be a different focusing point, where its position is defined by $\delta C = 2S_{11}(\theta d/a)^2(2 \pm 1)$. That is, each angle will have their own $ABCD$ matrix and it's own stability. For positive aberrations, and for the typical values observed in the experiment (figures 3.2 and 3.14) the variation in x is of few microns. If $\Delta z < 0$, at $\theta = 0 = \theta_0$, the Gaussian waist follows the orange curve presented in 3.2. For increasing θ the stability curve is shifted to higher values of x. In figure 3.23 we present an example, taking the values of Figure 3.2, where $\delta z = -2.74$ mm, $f_{th} = 55$ mm, and considering $1/\delta C$ is of the order of few microns. The orange plot, relative to the on axis condition (θ_0), is presented as a reference. As the angle is increased: $\theta_0 < \theta_1 < \theta_2 < \cdots$, the waist evolution curve shifts to higher value x. Hence, as x is increased in the experiment, the emission from the VECSEL will "jump" from one curve to another, *i.e.*, increasing θ in order to match the pump waist of 20 μm.

3.5 Case $C \sim 0$

So far we have described the different spatial emission our VECSEL can provide when $|\Delta z| > 1$ mm. According to the analysis presented in Chapter 2, the longitudinal range in x where the Gaussian solution is stable becomes increasingly narrower as $C \to 0$ (see figure 2.10). In fact, in perfect SIC condition the cavity should present degeneracy of solutions of any basis [Arnaud, 1969]. In this situation, small variations of the pump

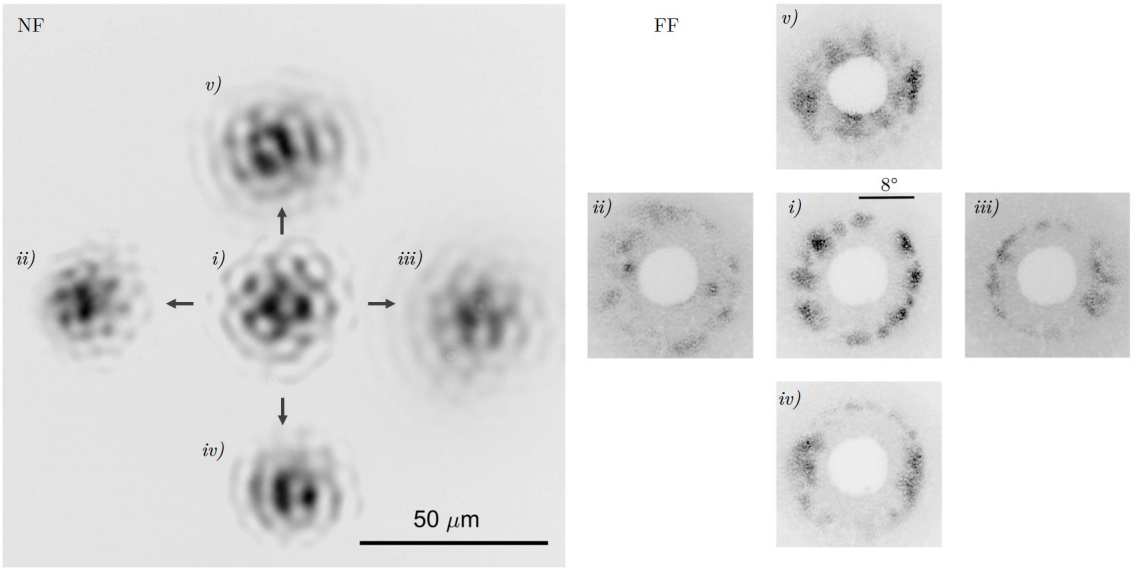

Figure 3.24. Self-imaging ($\Delta z \approx \Delta x \approx 0$) transverse window on the near-field gain, scanned by moving the pump position in a wide area (P_p = 292 mW). In left is present the corresponding far-field of each position *i)-v)* of the emission.

power, which affects (x_0, z_0), have a strong impact on the emission. Still, as it was explained in the ZEMAX analysis, for the waist values of the emission observed so far (figure 3.2), our control in x is much below their Rayleigh range. Then, we have explored the emission in the case $C \sim 0$ as a function of the x position of the SESAM.

Before describing the spatio-temporal dynamics for $C \sim 0$, we show the results of a test for the quality of self imaging condition realized when both $C \sim 0$ and $B \sim 0$. In the previous Chapter, we have demonstrated that the field curvature of the transverse window on the gain facet is barely deformed on the pumped area when B and C were close to zero (see figure 2.17). Hence, in the SIC condition, an off-axis pump beam should lead to lasing emission, provided that the pumped region is within the numerical aperture of the cavity. We have tested this translation invariance in the transverse plane of the cavity by moving the pump position around the optical axis. For high value of pump power P_p hexagonal patterns, as the ones presented in section 3.3, are emitted. The result is shown in Fig. 3.24 where we plot the near-field emission of the VECSEL as the pump is dragged in the 4 directions of the transverse section with respect the optical axis (left, right, up and down). In the left panel of Fig. 3.24 we show the corresponding far-field profiles for each position of the pump. We see that, for a shift inside a range of $150 \times 150\ \mu\text{m}^2$, lasing emission is maintained and the pattern is not strongly deformed. The change in the pattern modulation are mainly due to the inhomogeneities of the gain section, as it was observed in fig. 3.4.

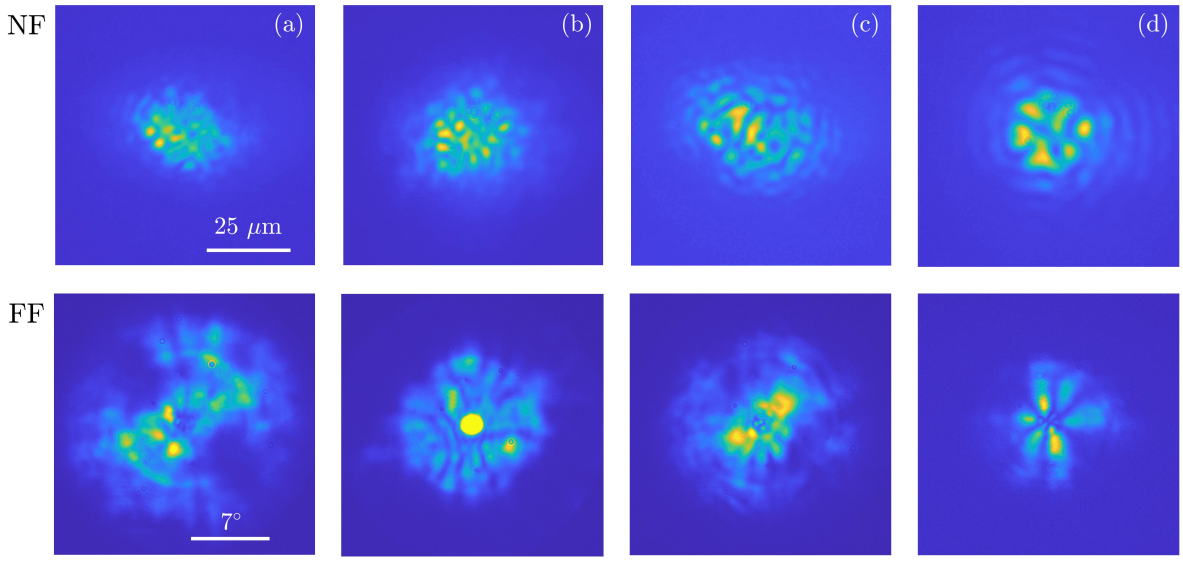

Figure 3.25. near-field (up) and (far-field) of the high numerical aperture non self-transformed patterns observed when $\Delta z \sim 0$ at $P_p = 220$ mW ($\delta\lambda = 6$). They were obtained for different values of x. (a) ~ 0, (b) 1 μm, (c) 3.5 μm and (d) 6 μm.

Figure 3.25 presents the near-field and far-field of the spatial evolution when increasing the distance x of the SESAM respect to L_4 within a range of 6 μm at constant pump power of 220 mW. It is important to point out that, in this condition, Gaussian mode solutions do not appear in any range when varying x. Instead, complex patterns appear, having a wide far-field angle and not homothetic to their near-field profile. As it is observed, the closer to $x \sim 0$ (panel a), the larger the far-field profile. For instance, the far-field emission of the pattern obtained for $x \sim 0$ covers the largest part of the full numerical aperture available in the cavity ($\theta_{max} = 14.4°$). At $x = 1$ μm the pattern observed is the result of a superposition between an high intensity on-axis pattern emission with a wide far-field pattern, as the one observed for $x \sim 0$. This coexistence of different patterns indicates that the system is closed to a degenerate state. Finally, for $x = 3.5$ and 6 μm, the intensity peak of the far-field start to decrease up to 5° (e) and 4° (d).

As a consequence of the degeneracy of the cavity, pattern emission becomes strongly dependent on pump power. This is demonstrated in figure 3.26. In panel a) the pattern corresponds to $P_p = 220$ mW, and when increasing up to $P_p = 235$ mW, more spots appear in its surroundings.

In the previous sections we have demonstrate that for a proper setting of the micro-cavity resonances detuning $\delta\lambda$, it is possible to achieve temporally localized pattern emission. The presence of coexisting pattern emissions in the situation here analyzed

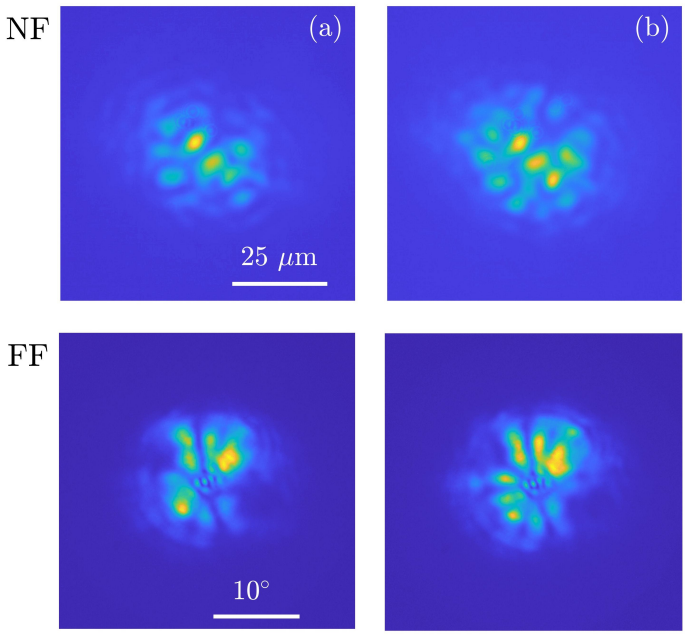

Figure 3.26. Degenerate case for a pattern at $x = 4.5\ \mu$m for (a) 220 and (b) 235 mW in pump power. near-field of panel b shows the appearance of multiple spots behind the pattern in case panel a.

suggests that spatially localized emission may be present as well. Accordingly, we report on temporally localized emission where coexisting pulsating solutions correspond to different pattern emission. In Figure 3.27 we show a spatio-temporal bifurcation diagram obtained by scanning up and down the pump power P_p. The near-field and far-field profiles together with the temporal behavior of each branch are plotted as well. When increasing P_p from zero to threshold (P_p =258 mW), the system jumps to the branch with the hexagonal pattern described in section 3 with a 4 pulses per round-trip emission in the time domain. When decreasing P_p, close to 224 mW, the system jumps to a branch characterized by the overlapping of two patterns (panel c) each one with a different temporal behavior. Coexistence of these two patterns is observed for 213 mW $< P_p <$ 222.5 mW. One is a sort single lobe pattern which is pulsating with 6 pulses per round-trip while the second one is a four lobes pattern that is pulsating at one pulse per round-trip. The trains of pulses emitted by each pattern have different intensities and they can be easily differentiated on the corresponding spatio-temporal diagram. The four-lobes is isolated in panel d) while the single lobe is isolated in panel f). For 208 mW $< P_p <$ 212 mW the single lobe pattern coexists with a stripe pattern which is shown in panel e). As the pump scans the different branches we did not observed the stairway observed in the previous sections between branches with different number of

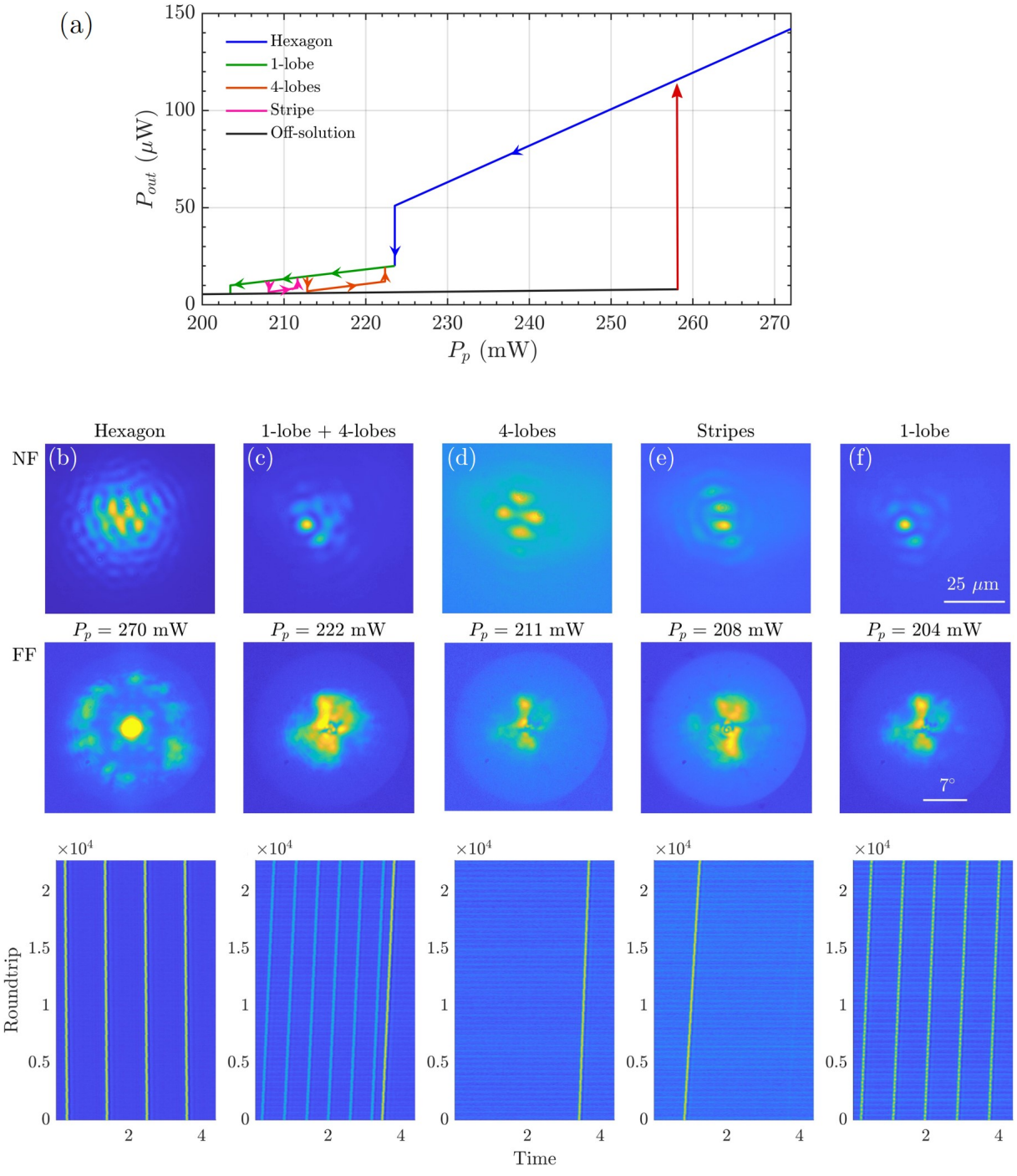

Figure 3.27. (a) Hysteresis diagram of the different pattern appearance as a function of P_p. (b)-(f) the near-field (up), far-field (middle) and space-time diagram (low) of these different solutions. $\delta\lambda$ = 5 nm.

pulse per round-trip. Different realizations of the hysteresis cycle shown in Fig. 3.27 may lead to similar patterns with a different number of pulses emitted per round-trip. For example, in panel f), the single lobe pattern in time domain consists of 5 pulses per round-trip, while the same pattern in panel b) consists of 6 pulses per round-trip. These observations are quite preliminary and they were obtained at the end of my thesis. They show the existence of a clear hysteresis between different spatio-temporal solutions at variance with observations in previous section where mulitstability was observed between solutions having different number of pulses per round-trip but sharing the same spatial emission.

3.6 TLS width and coherence time

Autocorrelation of TLS field enables to estimate with precision their coherence time. In order to realize this field autocorrelation the output signal from the VECSEL was sent to a Michelson interferometer composed by two arms of length l_1 and l_2, and closed by two high reflectivity dielectric mirrors. A 50/50 beam splitter was used for separating, and recombining the beams. The combined signal was detected by a switchable gain photo-detector (Thorlabs PDA100A-EC), and sent to the oscilloscope. One of the mirrors is attached to a piezo-electric positioner which is controlled by a periodic signal. When the length of the two arms is the same, $l_1 = l_2 = l_0$, constructive interference should be observed. Then by applying a periodic signal, the position of one mirror is longitudinally shifted of several wavelengths. Hence, interference signal on the scope oscillates from

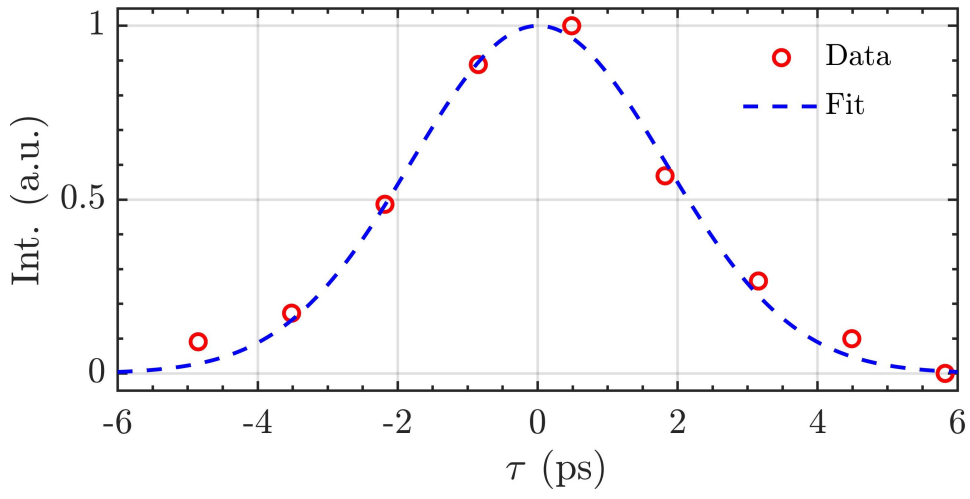

Figure 3.28. Data points (red) and fit (blue) of the coherence time reconstruction. The width at FWHM of $\mathcal{I}$ is 4.3 ps.

completely constructive (V_{max}) to destructive (V_{min}).

As l_2 is scanned, the visibility of these fringes decreases because of the finite coherence time of the pulses. Hence, we can plot fringes visibility as a function of delay time between the two arms $\tau = 2(l_2 - l_1)/c$, as shown in figure 3.28. From this measurement we can obtain a coherence time $\tau_c = 2.57$ ps which corresponds to a full spectral width of approximately 0.9 nm. This measurement compared with the optical spectra obtained in the regime of TLS, but it is more precise since the resolution of the spectrum analyzer was only 0.5 Angstrom, *i.e.* 13 GHz. Time width measurement of the pulse has been realized by using a 42 GHz bandwidth detector connected to a 33 GHz bandwidth oscilloscope. The pulse acquisition was limited by the measurement bandwidth. Accordingly, a pulse time width of about 20 ps was measured.

3.7 Conclusions

We have realized a broad-area optically pumped VECSEL with an external cavity in nearly self-imaging condition and we have driven this laser in the regime of temporal localization. Thanks to the study developed on Chapter 2, we have characterized all the possible lasing regimes depending on the value of C. We succeed to locate the SIC in the presence of a thermal lens f_{th}, by observing the evolution of the fundamental Gaussian solution as a function of the position x of the SESAM respect L_4, and when $\Delta x \to 0$, non self-transformed patterns appear. For $C < 0$, hexagon-like patterns appear, consisting of a Gaussian on-axis component, modulated by the interference of wide angle tilted waves. These latter bring less than 10% of the total power. On the other hand, when $C > 0$, the patterns are composed by multiple tilted waves, that coexist azimuthally. We explain heuristically that these tilted waves arise due to the aberration of the system, which suggests that the VECSEL is still operated at the frontier where the optical elements play a relevant role. When the detuning of $\delta\lambda$ between the gain and SESAM microcavities is properly tuned, both tilted waves and hexagonal patterns are temporally localized pulses. We have shown that they can be individually addressed by an external perturbation. Furthermore, we were able to reduce $C \sim 0$, and we observe different coexisting spatio-temporal lasing states characterized by different spatial profiles each one pulsating at a different rate per round-trip. Hence, this full spatio-temporal platform enables the experimental analysis of novel laser regimes with characteristics that are approaching the ones of dissipative light-bullets.

CHAPTER 4

Manipulation of temporal localized structures in a VECSEL with optical feedback

Contents

4.1 Introduction

In the previous Chapter we have shown that our VECSEL operated close to self-imaging condition emits complex patterns. The variety of solutions depends on the sign of parameter C of the $ABCD$ round-trip matrix, passing from the Gaussian solution, when the position of the SESAM is far from $\Delta x = 0$, to Tilted waves (for $C > 0$) or hexagonal structures (for $C < 0$) when $\Delta x \to 0$. These solutions can be operated in the time localized passive mode-locked regime, provided that the gain and the SESAM micro-cavity resonances are properly detuned. We have demonstrated the possibility of address these pulses via an external pulsation perturbation, whose repetition rate should match the cavity round-trip τ_c. In the last decade, the control, manipulation and optimization of the semiconductor PML lasers dynamics has become an extremely attractive topic due to its strong potential for applications. Optical feedback improves the timing jitter in high repetition rates mode-locked lasers and offers the possibility to precisely harness the pulse train repetition rates [Otto, 2012; Arsenijević, 2013; Jaurigue, 2015; Nikiforov, 2016]. Recent works addressed the nonlocal interactions induced by a

second delay on vectorial TLSs observed in VCSELs [Marconi, 2015b; Javaloyes, 2017]. However, the impact of feedback in PML semiconductor lasers operated in the long cavity regime still remains poorly understood, both experimentally and theoretically. To our knowledge, optical feedback was mainly studied in the context of spatial solitons were it leads to e.g., zigzagging [Puzyrev, 2016; Schemmelmann, 2017], drifts [Vladimirov, 2014], pulsations [Schelte, 2017] and chaos [Panajotov, 2014].

In this Chapter, we address the effect of optical feedback in a low repetition rate PML VECSEL operating in the long cavity regime. We have focus only in the temporal dynamics of our VECSEL, and for this purpose, only the fundamental Gaussian mode solution has been considered. This was obtained for $\Delta z < 0$ as in panel D of figure 3.14. These results were obtained with gain GaAs-861 and the SESAM GaAs-830.

4.2 Experimental results

In comparison with the results of the previous Chapter, the cavity setup, presented on figure 4.1, consists of an straight cavity where the light is extracted by a dichroic mirror, as the one presented on panel b of figure 2.14 of Chapter 2, where τ_c is long enough so that the laser operates in the localized states regime. We used the same pumping method as in [Camelin, 2018], where an elliptical @780 nm Gaussian beam was projected on the gain facet at the Brewster angle, for achieve a 15 μm circular Gaussian profile (inset on figure). In this regime, the TLSs can be independently addressed by an external perturbation [Camelin, 2016]. To avoid any spatial dynamics [Cao, 2019], the lenses are positioned in the cavity in order to insure that the output beam has a stable Gaussian profile. For that we have chosen $\Delta z = -3$ mm, and operated x position of the SESAM in the minimum value to obtain such Gaussian emission, similar to the solution D of figure 3.14.

As it was detailed in sections 3.3.1 and 3.4.1, the regime of TLSs is characterized by a multistability (as shown in 3.18) close to the lasing threshold between the multiple harmonic mode-locking regimes (HML$_n$) in which the laser emits N pulses separated by τ_c/N. The maximum number of pulses per round-trip N_m is approximately equal to the ratio of the cavity round-trip τ_c and the gain recovery time τ_g, $N_m = \tau_c/\tau_g$. For a cavity length of 63 cm $\tau_c = 4.3$ ns and, since $\tau_g = 1$ ns we find $N_m \simeq 4$. To study the sensitivity of this regime to optical feedback, we implement a light re-injection arm closed by a mirror with 99 % reflectivity at 1064 nm (feedback arm on figure 4.1). To

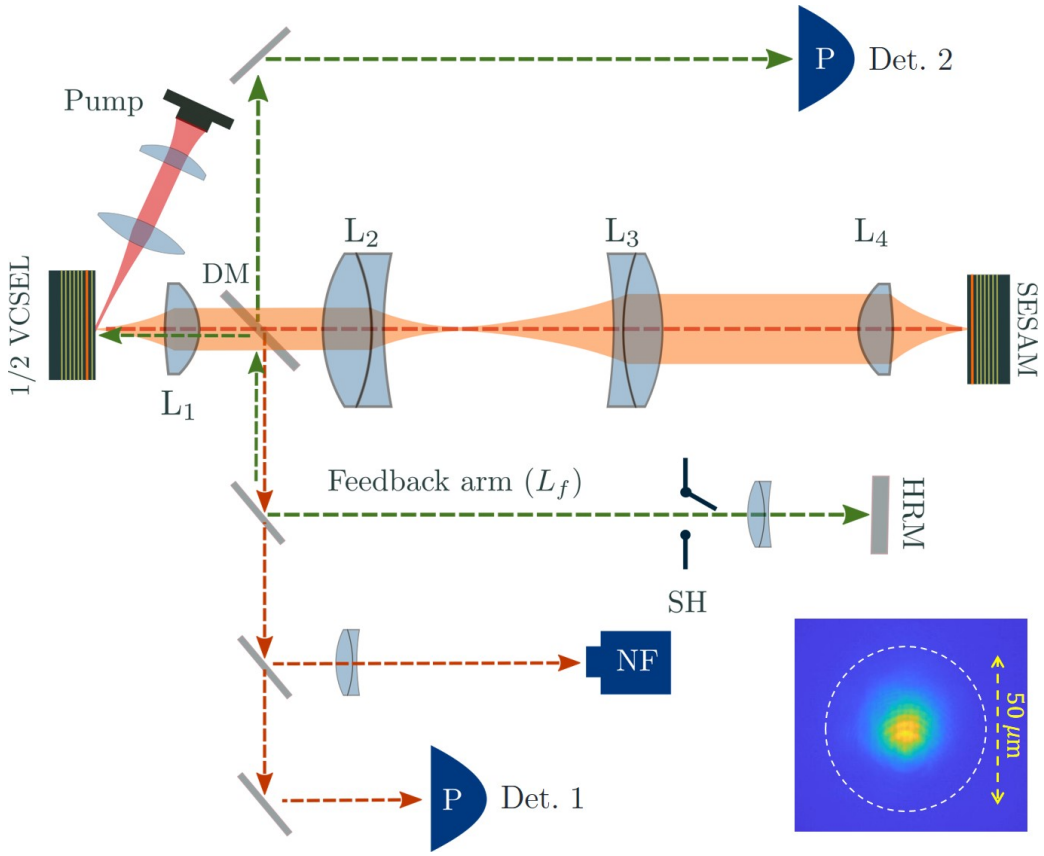

Figure 4.1. Experimental setup of the PML VECSEL with optical feedback. DM: Dichroic Mirror, C: collimator, L1 and L2: achromatic lenses, P: Photodiode, NF: spatial near-field of the VECSEL emission recorded on a camera, M: Mirror. The inset displays the NF profile of the Gaussian mode solution.

avoid some diffraction losses in the feedback arm, we place a 50 mm lens that focuses the light on the mirror, in a way that mode-matching is achieved on the gain facet.

With the presented setup one can reach a maximum of 10^{-3} % of feedback. This value is strongly limited by the intracavity dichroic mirror, that takes out only 2% of the light at 1064 nm. The remaining re-injected light that is transmitted by the dichroic mirror is collected by a fast photodiode and will be used to trig the detection on the feedback signal when the arm is open. In figure 4.2, we show the effect of the feedback when it is applied in the regime of fundamental PML (one pulse per round-trip). The re-injected pulse interacts with the gain medium after a delay τ_f that is in this case smaller than τ_c. One can see that the pulse will deplete the gain available during its interaction and produce a small pulse satellite at the distance $\Delta\tau = \tau_c - \tau_f$ form the main pulse that is visible on the temporal time trace acquired with DET2 (see setup in Fig. 4.1). Optical feedback is therefore inducing *a nonlocal effect* via light-matter interaction in the gain medium. In the example of figure 4.2, the feedback does not perturb the fundamental

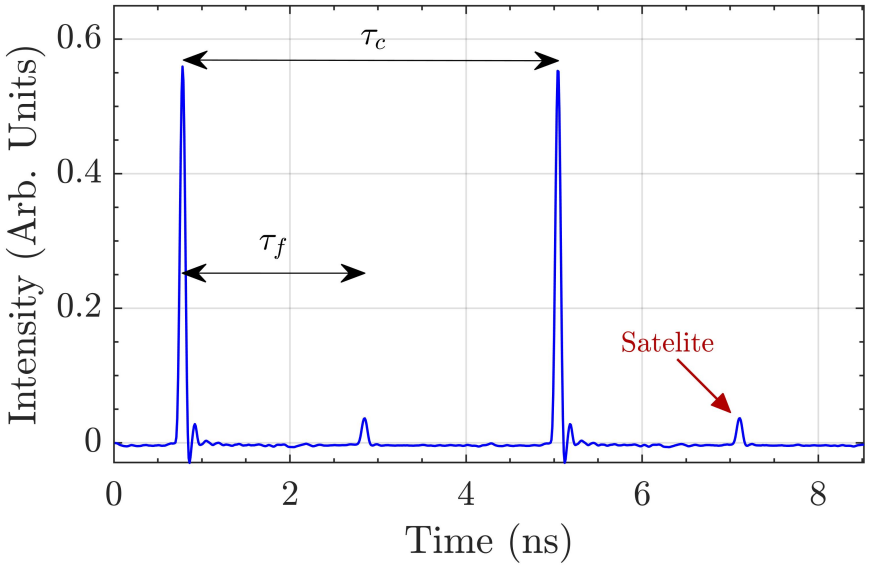

Figure 4.2. Typical pulse train with period $\sim \tau_c$ and where the feedback induced satellite is located at $\Delta\tau = \tau_c - \tau_f$ from the main pulse.

PML regime since the satellite is re-injected far from an existing pulse, i.e. $\tau_f \neq n\tau_c$ and the feedback level is low.

We analyzed experimentally the effect of feedback when τ_f is slightly smaller or larger than the temporal interval between two consecutive pulses. We first present the results when $\tau_f \sim \tau_c/2$ and prepare the PML laser in the HML_2 regime. Depending on the precise value of τ_f, the light pulse will be re-injected before or just after the emitted pulses.

In figure 4.3 a) we show the space-time diagrams for the case where τ_f is slightly larger than $\tau_c/2$, with $\tau_f = 2.24$ ns. At round-trip 0, the laser is operating in a HML_2 regime with two equidistant pulses in the cavity separated by $\tau_c/2$. At round-trip 12000, feedback is applied. We observe that in this case, the feedback has no effect on the pulse dynamics. The situation changes drastically when we set $\tau_f = 2.06$ ns, thus slightly smaller than $\tau_c/2$ (see figure 4.3 b)). In this case we see that the feedback is erasing one of the two pulses, leaving the system operating in the fundamental TLS regime. The re-injected pulse is inducing a depletion of the gain, and when this depletion occurs just before another pulse reaches the gain section, it will lower its amplification. After several round-trips of diminished amplification, this pulse may eventually get erased. We also note that the remaining pulse is speeding up and its amplitude increases when the second one disappears, this is due to the increase of local gain experienced by the pulse in the cavity [Camelin, 2016].

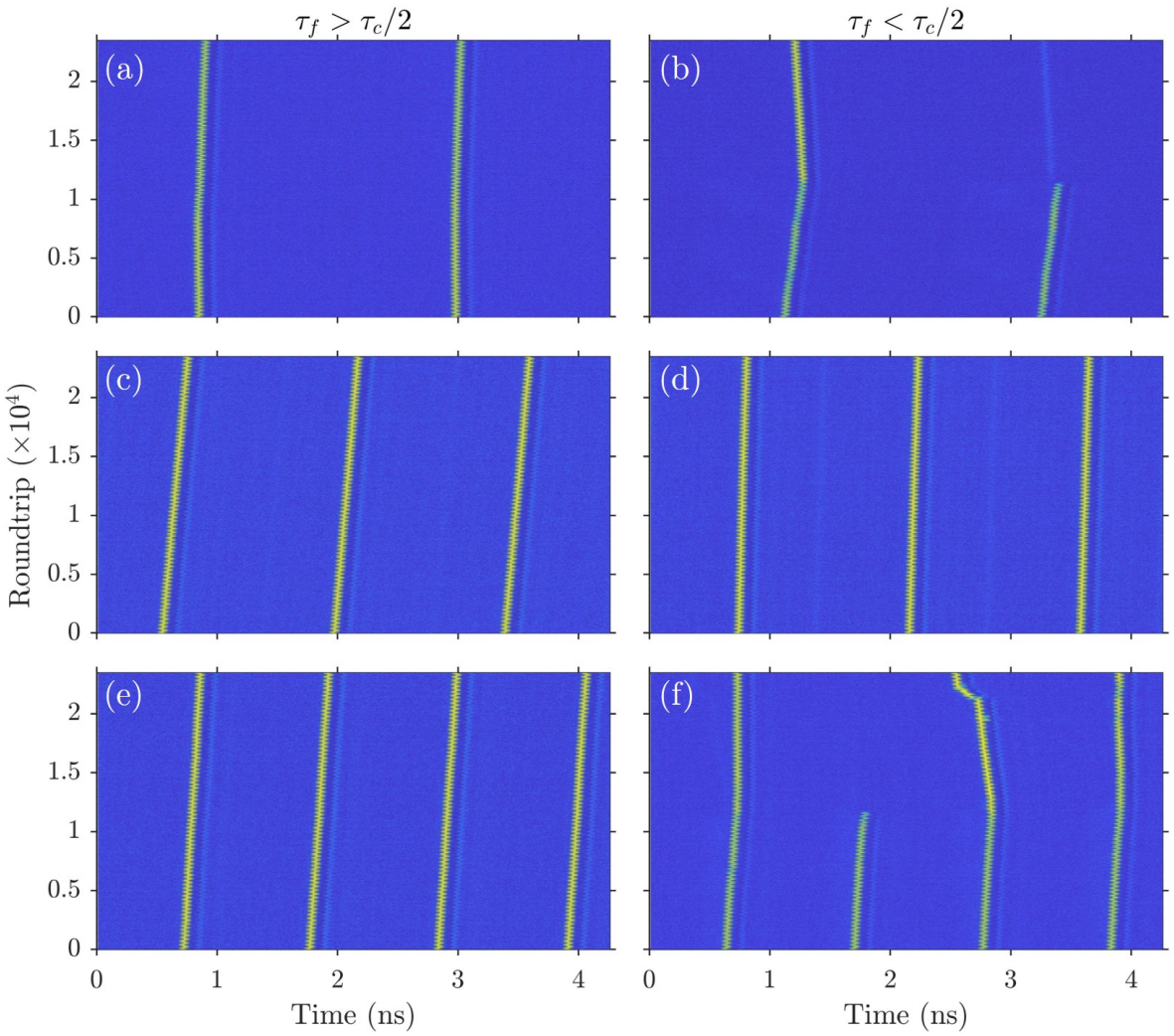

Figure 4.3. Spatio-temporal diagrams of the pulse dynamics for two (top), three (middle) and four (bottom) TLSs in the cavity for two distinct values of the feedback delay τ_f around $\tau_c/2$. Feedback is applied at round-trip 12 000.

We now analyze the effect of the feedback when the laser is operating in the HML_3 and HML_4 regimes. Again, the feedback is applied at round-trip 12000 and τ_f is slightly larger (left column) or smaller (right column) than $\tau_c/2$. figures 4.3 c)-d) show that the feedback has no effect over the HML_3 regime independently of the precise value of τ_f chosen around $\tau_c/2$. Indeed, in this case the feedback-induced gain depletion occurs exactly between two pulses that are already present in the cavity; the feedback depleted gain has enough time to relaxes to equilibrium and the other pulses do not feel this parasitic depletion. However, we observe that feedback can erase a pulse when starting from the HML_4 solution, comparing figures 4.3 e)-f), in a way similar to the HML_2 case. Since both solutions HML_4 and HML_2 contain a pulse separated of $\tau_c/2$, the feedback with a delay slightly smaller than $\tau_c/2$ is going to act. After one pulse is erased, we

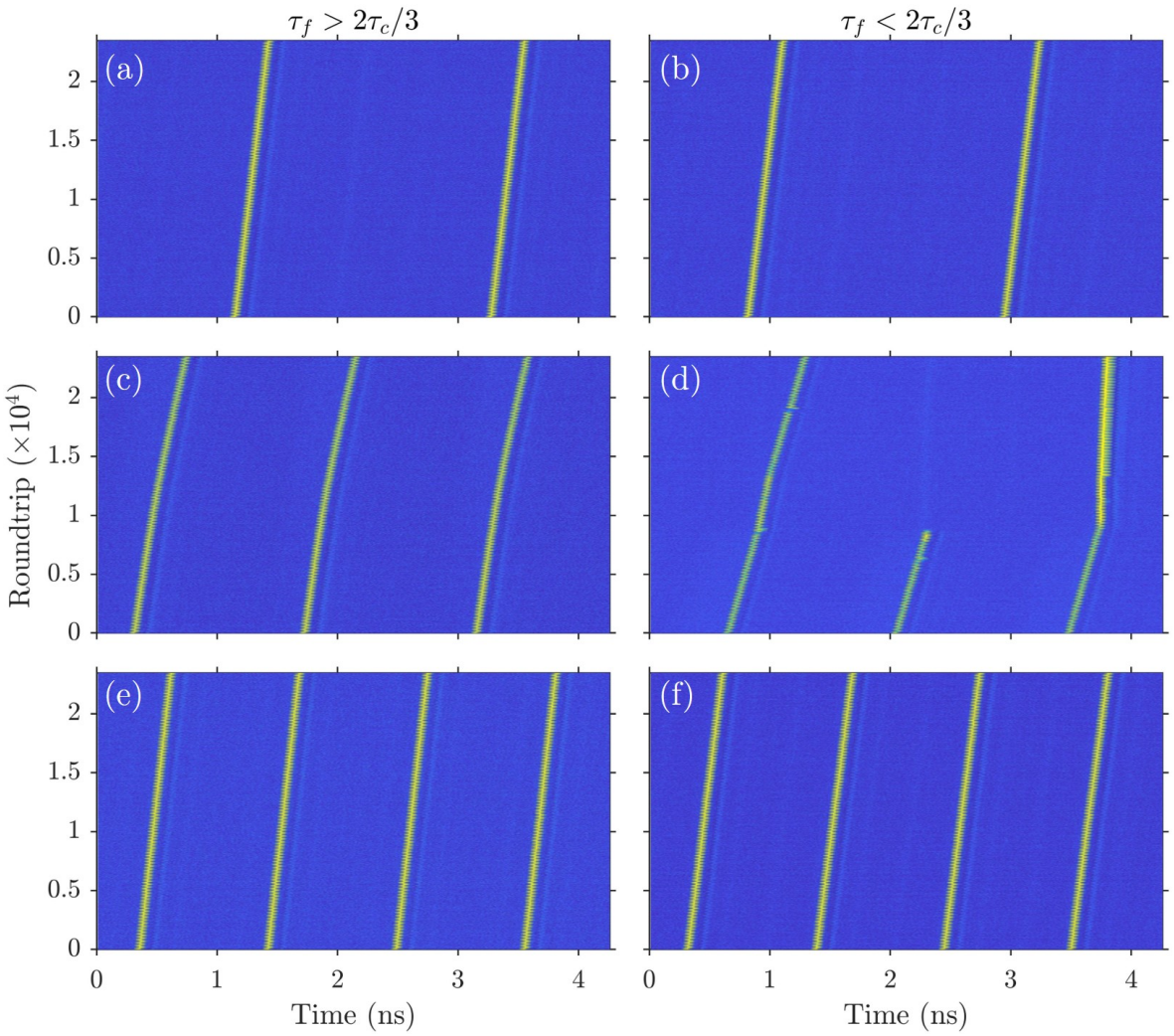

Figure 4.4. Spatio-temporal diagrams of the pulse dynamics for two (top), three (middle) and four (bottom) TLSs in the cavity for two distinct values of the feedback delay around $2\tau_c/3$. Feedback is applied at roundtrip 9 000.

clearly observe how the three remaining pulses start the process of rearrangement. This process is not captured until the end, but the space-time map gives an indication of the timescales at play.

Finally, we conclude our experimental analysis by setting the feedback delay to another value this time around $2\tau_c/3$. Our results are shown in figure 4.4 for the $\mathrm{HML}_{2,3,4}$ solutions and τ_f slightly larger (left) or smaller (right) than $2\tau_c/3$. In this condition, we see that, as opposed to the previous case, the only solution that is being affected when $\tau_f \lesssim 2\tau_c/3$ is the HML_3 solution (figure 4.4d) while the even solutions $\mathrm{HML}_{2,4}$ are not affected at all, comparing panels a with b, and e with f. In figure 4.4 d), we observe the same reconfiguration of the pulse positions in the cavity as in the $\tau_f < \tau_2/2$ case.

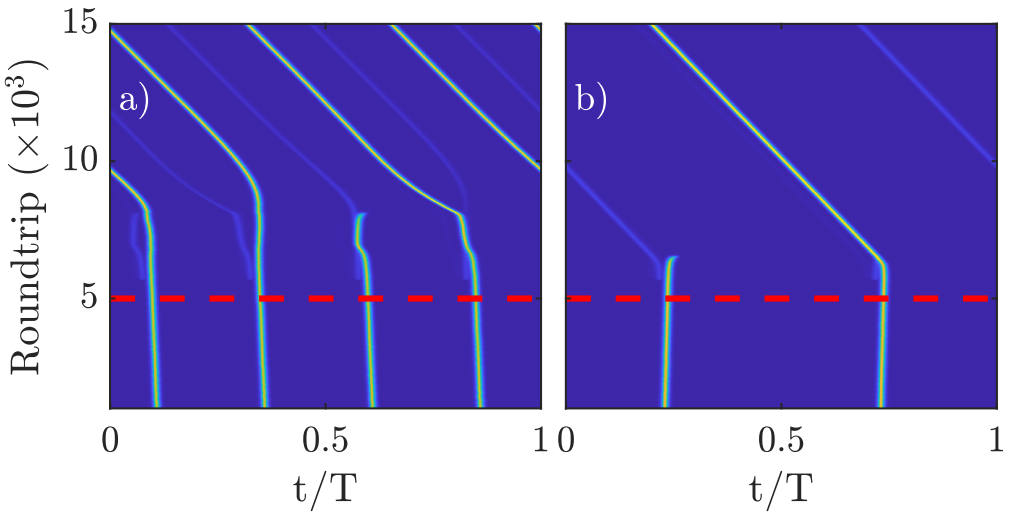

Figure 4.5. Direct numerical simulations of Eqs. (4.1-4.3) for the HML_4 a) and HML_2 b) solutions. Time delayed feedback is turned on after 5000 round-trips as indicated by the dashed red line. The gain value are a) $g = 1.08$, b) $g = 0.952$ and $\tau_f = 48$.

4.3 Theoretical Analysis

In order to understand the experimental observations, a theoretical analysis was developed with the collaboration of the groups of the Univserite de les Illes Balleares and Münster Univesity. We have employed a widely used theoretical framework that considers a PML laser in a ring geometry, in which the gain medium is coupled to a saturable absorber and a narrow band optical filter. Such a description is embodied in the delayed differential equation (DDE) model first presented in [Vladimirov, 2005]. This model is extended by a term describing the time-delayed feedback as in [Otto, 2012; Jaurigue, 2015]. Denoting by U the amplitude of the optical field, G the gain, and Q the saturable losses, the DDE model reads

$$\frac{\dot{U}}{\gamma} = \sqrt{\kappa}\exp\left[\frac{1-i\alpha_g}{2}G\left(t-\tau_c\right) - \frac{1-i\alpha_a}{2}Q\left(t-\tau_c\right)\right]\times$$
$$U\left(t-\tau_c\right) - U\left(t\right) + \eta e^{i\Omega}U\left(t-\tau_f\right), \tag{4.1}$$
$$\dot{G} = g_0 - \Gamma G - e^{-Q}\left(e^{G}-1\right)|U|^2, \tag{4.2}$$
$$\dot{Q} = q_0 - Q - s\left(1-e^{-Q}\right)|U|^2, \tag{4.3}$$

where time has been normalized to the SA recovery time, τ_c is the fundamental delay which corresponds to the round-trip time, $\alpha_{g,a}$ are the linewidth enhancement factors

of the gain and absorber sections, respectively, κ the fraction of the power remaining in the cavity after each round-trip, g_0 the pumping rate, Γ the gain recovery rate, q_0 is the value of the unsaturated losses which determines the modulation depth of the SA, s the ratio of the saturation energy of the SA and of the gain sections and γ is the bandwidth of the spectral filter, η is the feedback rate, Ω is the feedback phase and τ_f the round-trip time of the feedback loop. The lasing threshold for resonant feedback reads $g_{\text{th}} = \Gamma\left[q_0 - \ln(\kappa) + 2 \cdot \ln(1 - |\eta|)\right]$, and we defined a normalized gain value $g = g_0/g_{\text{th}}$. We fix $(\gamma, \kappa, \Gamma, q_0, \alpha_g, \alpha_a, s, \eta, \Omega) = (10, 0.8, 0.04, 0.3, 1.5, 0.5, 10, 0.005, 0)$ while the cavity round-trip is set to $\tau_c = 100$.

At $g = 1$ the off state $(U, G, Q) = (0, g_0/\Gamma, q_0)$ becomes unstable and a branch of continuous wave (CW) solutions emerges. This branch undergoes several Andronov-Hopf (AH) bifurcations from which the fundamental (FML) and the HML_n solutions emerge. In the long delay limit the AH bifurcations become subcritical and eventually the branches of pulsating solutions detach from the CW branch. In this case, the latter may extend below the lasing threshold and coexist with the off state [Marconi, 2014b]. There, the localized solutions gain stability via Saddle-Node bifurcation of Limit Cycles (SN) for the FML solution or a Torus bifurcation for HML_n solutions. The direct numerical simulations of equations (4.1-4.3) displayed in figure 4.5 reproduce well the experimental findings depicted in figure 4.3,4.4.

The system is initialized with the HML_4 and the HML_2 solutions and optical feedback is applied after 5000 roundtrips (red dashed line); in both cases feedback destroys the HML_n solution and the system settles after a transient on a HML_{n-1} solutions instead. This begs the question in which regimes time-delayed feedback has a destabilizing effect on the TLSs. A detailed bifurcation analysis using path continuation techniques was performed employing the software package `DDE-BIFTOOL` [Engelborghs, 2002] which can follow solutions in parameter space, continue bifurcation points in two-parameter planes and allows to determine the stability of periodic solutions by computing their Floquet multipliers μ. The normalized gain g is used as the main continuation parameter while the solution measure is $P = \max(|U|^2)$.

In figures 4.6 a)-c) we present the bifurcation diagrams in g for a HML_4 solution for different values of τ_f close to $\tau_c/2$. In panels a-c, solid lines (respect to dashed ones) stand for stable (respect to unstable) solutions. The black star in panel a indicates the parameters in figure 4.5 a), the blue dots mark SN bifurcations and the green squares

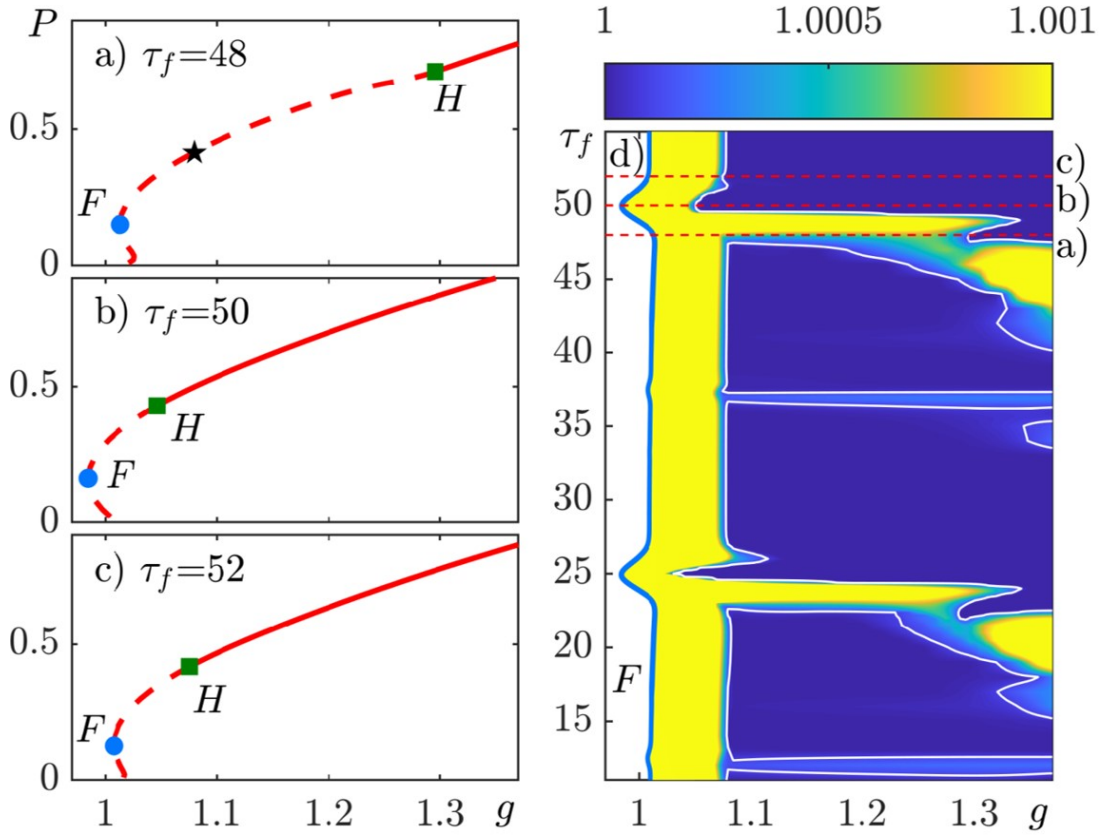

Figure 4.6. (a)-(c) Bifurcation diagrams of equations (4.1,4.3) for a HML_4 solution. (d) Full plane (τ_f, g) with the cuts (a)-(c) marked in dashed lines and the blue line denotes the SN bifurcation.

denote the Torus bifurcations in which the solutions gain stability. In panel a the satellite is placed close to the leading edge of the main pulse as in figure 4.5 a). As expected the branch is unstable for a wide range of g because the satellite depletes the gain which cannot recover fast enough before the main pulse arrives. Only for high gain values when enough amplification is provided for both the satellite and the main pulse, the solution restabilizes via a torus bifurcation H (green square). When the time-delayed feedback is applied resonantly as seen in figure 4.6 b), *i.e.* when the satellite coincides with the main pulse, the range of stability increases significantly. Placing the satellite at the trailing edge of the main pulse does not destabilize the solution (see panel c)). However, the range of stability is slightly smaller than in the resonant case.

To quantify these results even further, it is helpful to consider the (τ_f, g)-plane which is presented in figure 4.6 d). The blue line on the left marked with F corresponds to the SN bifurcation marked in panels a-c. The dashed red lines indicate the cross-sections at which a-c are plotted. The colormap shows $\max(|\mu|)$. Blue regions within the white contour line correspond to stable regions while the rest is unstable. Here, the colormap encodes the absolute value of the maximal Floquet multiplier for a given HML_4 solution.

It is obtained by following 104 branches in g of approximately 80 steps each for different (non-uniformly distributed) values of τ_f. After computing the Floquet multipliers for each periodic solution, the data were interpolated. The white contour line in figure 4.6 d) represents the border of stability of the HML_4 solution.

It can be clearly seen that the region in which time-delayed feedback destabilizes the HML solution is limited to the vicinity of the leading edge of the main pulse ($47.5 \lesssim \tau_f \lesssim 49.4$). When the satellite is placed even closer to the main pulse, the opposite is the case and the satellite increases the range of stable HML solutions, which can be seen in form of a bump in the colormap at $\tau_f = \tau_c/2 = 50$. The bump also occurs in the line corresponding to the SN bifurcation F. Placing the satellite on the trailing edge of the main pulse does not influence the dynamics as the satellite is unable to interact with the main pulse. As the displayed branches correspond to a HML_4 solution one can expect to see more resonances in the (τ_f, g)-plane at $\frac{\tau_f}{\tau_c} = \frac{1}{4}, \frac{3}{4}, 1$, etc. Indeed, at $\tau_f = 25$ a similar resonance in form of a bump in the colormap and the SN line can be observed. Interestingly, it has a different shape compared to the $\tau_f = 50$, since $\tau_f = 25$ couples all main pulses to their neighboring main pulse while $\tau_f = 50$ creates two interspersed pairs of coupled pulses. Another peculiar property can be seen at $\tau_f = 12.5$ and $\tau_f = 37.5$. At these points second order resonance can be observed, meaning that the satellite's satellite destabilizes the main pulse for a short range. The SN line also exhibits small bumps for these values.

4.4 Conclusion

Our analysis shows that coherent optical feedback acts as a reliable discriminator between the various multistable HML_n solutions that coexists in a long-cavity PML VECSELs. Provided that feedback is applied slightly before one of the pulse present in the cavity, it may hinders the appearance of the associated HML_n solution. This present and additional method for address TLS in a VCSEL, in comparison with the one presented in Chapter 5. Our results are well reproduced by a DDE model for PML including delayed feedback and a two-parameter bifurcation analysis exhibit strongly asymmetrical resonances around $\tau_f = \tau_c/n$ that are the result of the breaking of the temporal inversion symmetry due to gain depletion.

CHAPTER 5

Towards gain-pinned spatio-temporally localized structures in VECSELs

Contents

5.1 Introduction

In large aspect-ratio resonators the correlation length of the spatial structures emitted maybe much shorter than the size of the system. Spatially localized structures are the paradigmatic example of this situation, as it was shown in [Barland, 2002; Genevet, 2008]. In our system, despite the efforts to reach a large aspect-ratio, the patterns emitted exhibits a correlation length close to the diameter of the pumped area. This correlation was checked in Chapter 3 in different ways. *i*) The spatially resolved monitoring of the output profile reveals that pulsation is synchronous everywhere within the pattern emitted. *ii*) The overlap in an interferometer of different parts of the pattern generates interference fringes, thus revealing coherence of the whole pattern. *iii*) The phase of patterns emitted was measured with a wavefront camera which reveal a phase relationship between all parts of the pattern. We conclude spatial decorrelation does

not appear spontaneously and other methods need to be implemented for forcing such effect. One of this method consists of using a spatially localized gain profile which can pin SLS and stabilize them [Mak, 2003; Malomed, 2014; Caboche, 2009a].

Recently it was experimentally observed that by shaping the gain of a semiconductor micro-cavity laser, gain-pinned dissipative solitons can be obtained [Pieczarka, 2020]. Gain shaping in VECSELs, and hence transverse emission selection, can be obtained by spatial modulation of the pump through a spatial light modulator (SLM) or by additional (small size) pump beams that overlap to the flat top main pump. Another method, much less flexible, consist of depositing an absorptive mask on the top of the gain mirror which reduces drastically the pump intensity reaching the quantum-wells. State-of-the-art lithography technology enables to design arbitrary patterns on the mask with nanometric resolution. In the recent years, the use of a gain mask filter in VECSELs provide advantages for the control of the transverse mode emission. This broadens the versatility of VECSELs in terms of applications, such as vortex generation [Seghilani, 2016], and coherent tunable THz sources via multi-mode for beating [Blin, 2017].

In this chapter we describe the results obtained by implementing these two solutions. We show that temporally localized structures are emitted from those spots in the gain mirror section, *hot spots* from now on, where the pump level is in the multistable region (see figure 3.19, $P_{off} < P_p < P_{th}$), provided that the gain level outside these spots is kept below this region $P_p < P_{off}$. The pulse emission from different hot spots may be uncorrelated, thus confirming that we are operating the VECSEL in the large-aspect ratio and that, the resonator design would allow spatial localization. It is important to stress that, in agreement with the results in Chapter 3, this spatial localized emission of TLS relies on the gain profile. If the hot spots are removed, the TLS emission stops. We may call these structures gain-pinned spatio-temporal localized structures, according to [Pieczarka, 2020].

5.2 Hot spots by adding small section pump beams

A flexible method to create hot spots that can be removed in the pumping profile consist in overlapping small size pump beams to the main homogeneous flat-top pump. We modify the set-up (see figure 5.1) by adding another pump laser @ 780nm, we split the beam along two paths and we recombine them in a polarization beam splitter. In each arm, a half-wave plate was used for controlling their polarization, and hence its

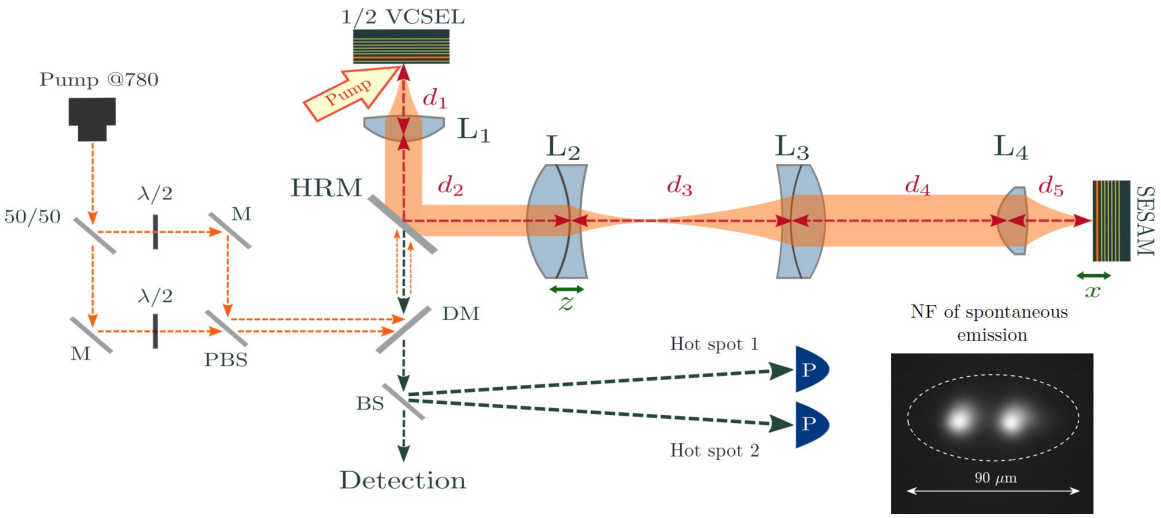

Figure 5.1. Experimental setup for the L-shape cavity. The two perturbations were generated out from a CW@780 nm laser sent to a Mach-Zhender interferometer. The beams power was controlled by half-wave plates, and sent to the cavity with a dichroic mirror (DM). The detection of each channel was done by creating the image plane of the gain in the Fraunhofer regime. The inset shows the spontaneous emission the two pumps are targeting the gain. The dashed line represents the size of the main flat-top beam profile.

transmitted power through the PBS. This power can be reduced up to a 60% in each arm. The beams were sent to the cavity with a dichroic mirror (DM) placed on the detection path which allows injection of the pump beams onto the gain mirror together with transmission of the output from the VECSEL towards the detection part. Two independent fast detectors were added in order to detect separately the output from the hot spots. After beam resizing, the hot spots on the gain mirror have a Gaussian shape with a waist of 7 μm (inset of 5.1).

We operate the VECSEL close to SIC in the tilted waves emission regime ($\Delta z < 0$). The detuning between the gain section and SESAM micro-cavities is set in the regime of temporal localization, as explained in Chapter 3. The flat-top power P_p is reduced significantly below the multistable region of figure 3.19 ($P_p < P_{off}$), while the small size pump beams power is set for reaching a total pump level in the hot spots above the multistable region ($P_{tot} > P_{off}$). Under such conditions we observe that two tilted waves with opposite transverse wavevectors are emitted from each hot spots (figure 5.2). These two tilted waves are counterpropagating, as the one emitted by the full pump profile in figure 3.15a of Chapter 3 but, because of the reduced size of the hot spot, the fringes in the near field emission profile are barely visible. We can notice that the patterns emitted remain spatially confined around the hot spots and that, if the two spots are sufficiently far-apart, their emissions do not overlap onto the gain mirror.

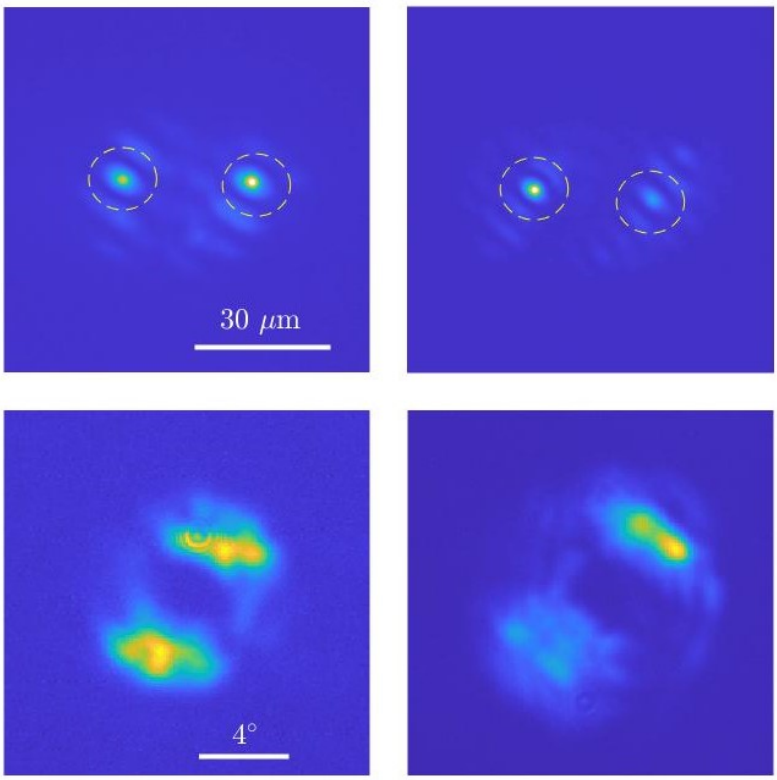

Figure 5.2. Near (up) and far (down) fields of the patterns observed by combining the main flat-top profile with the two perturbations (orange circles). The power values are P_p = 120 mW and $p_1 = p_2$ = 35 mW. These patterns are two separated group of fringes, each one located around the position of the small pumps. In the FF it is seen they are tilted waves with angle (a) 3.5° and (b) 5°.

Temporal emission from each hot spot exhibit four pulse per round-trip emission. By setting the power of each small size pump beams, the hot spots pump level is decreased within the multistable region ($P_{off} < P_{tot} < P_{th}$). Then, the number of pulses emitted per round-trip follow staircase-like bifurcation diagram as the one shown in figure 3.19. This indicate that hot spot has become a spatially localized source of TLS. Nevertheless, it is important to keep in mind that, because $P_p < P_{off}$, the existence of TLS is supported by the presence of the hot spot and, if the small size pump beam are switched off, TLS emission stops. On the other hand, as shown in Chap. 3, if the homogeneous flat-top pump is brought in the multistable regime, the emission does not stay localized around the hot spot (see figure 5.2).

When both hot spots are driven in the multistable region, by setting properly the power of each small size pump beam, we can drive the VECSEL to emit different pulsating solutions from each hot spot. An example of this situation is shown in Fig. 5.3 where we show by using the total spatio-temporal like representation, and the time trace

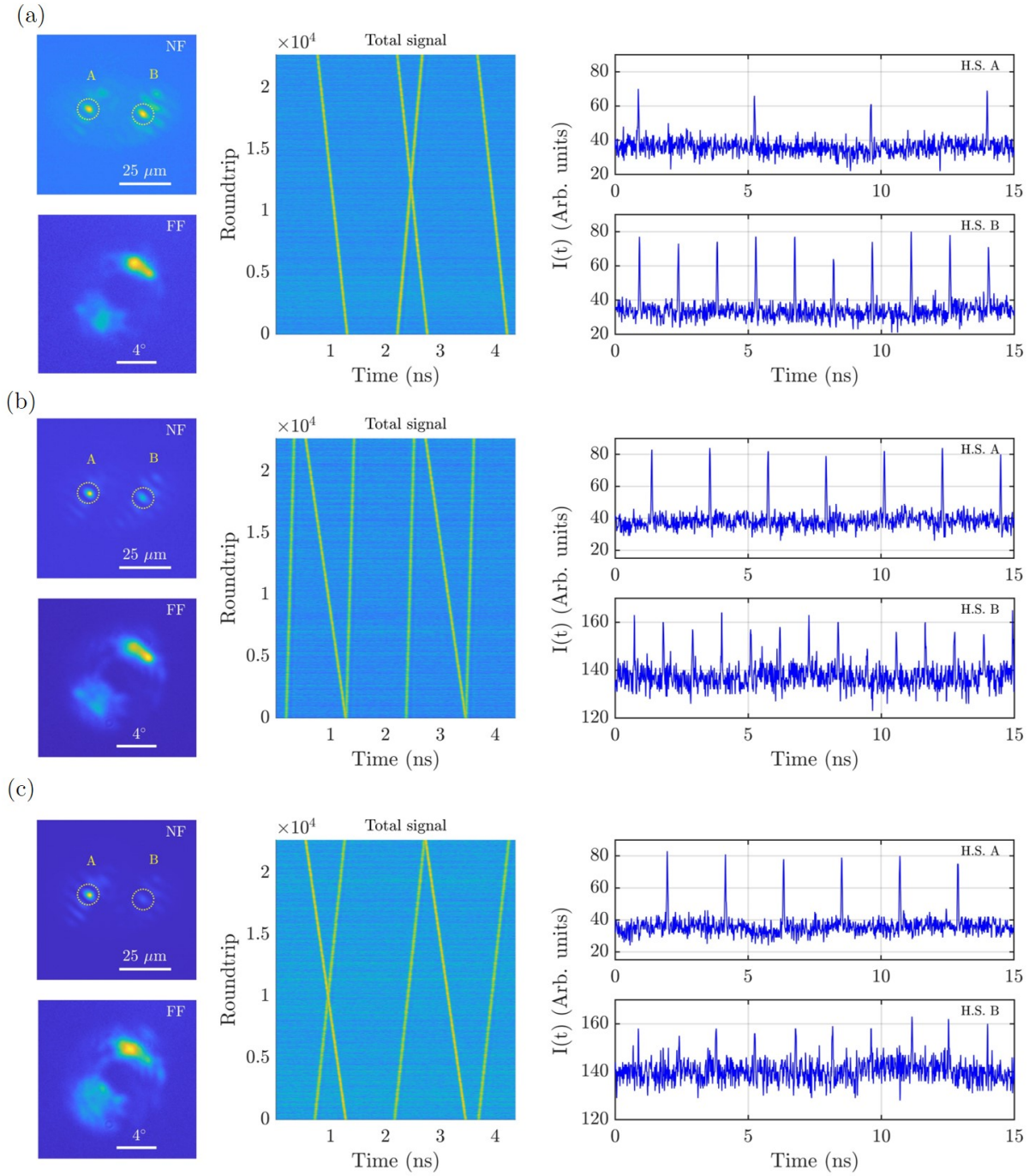

Figure 5.3. Spatial and temporal emission with two different hot spots induced by two different small pumps. NF and FF (left), the total spatio-temporal map (center) and the hot spot's individual time traces are shown for the solutions (a) $N_A = 1$, $N_B = 3$, (b) $N_A = 2$, $N_B = 3$ and (c) $N_A = 2$, $N_B = 4$.

evolution of the VECSEL emission from each hot spot. We observe we can have different pulses per round-trip solutions for each hot spot, $N_A = 2$ and $N_B = 3$ (panel a). By increasing the pump power in A we can pass to the solution $N_A = 2$ (panel b), without affecting the emission of hot spot B. In the same way, when we increase the pump power in B we pass to a solution $N_B = 4$, without changing hot spot A (panel c). This result show that our VECSEL resonator enables decorrelated emission from distant point in the transverse section. This is obtained by forcing the system with inhomogeneous gain profile. However, according to our results in Chapter 3, this decorrelation is not spontaneously achieved by self-organization.

The results described so far were obtained in a resonator configuration close to SIC for a negative value of Δz, where tilted waves are emitted when the gain profile is homogeneous. When we set the value of Δz for obtaining on-axis hexagonal pattern emission in the homogeneous pump situation, we have obtained an emission at the hot spots which is very similar to the one described in Fig. 5.2, i.e. two counterpropagating tilted wave emission. Despite having tuned Δz widely, we have never obtained axial emission from the hot spots.

5.3 Hot spots by absorptive masks onto the top facet of gain mirror

Another method to draw hot spots onto the gain mirror section for TLS pinning is based on depositing an absorptive layer with arbitrary profile on the top facet of the gain mirror. This is achieved by depositing an absorptive Cr layer onto the top of the gain chip where a spatial pattern can be designed via e-beam lithography and etching. This pattern has arbitrary shape, and it can be realized with a nanometric resolution while the Cr filter induces $\sim 90\%$ optical losses for a filling factor of 1; due to the absorption of the pump. Several square Cr masks having a side of 200 μm and different patterns were deposited onto a gain mirror (V0450) sample in collaboration with technological centre Renatech at C2N in Paris. These masks have been arranged in groups of 9×9 of them (total size of ~ 2.2 mm). Each group is repeated several times through the full section of the sample. A picture taken under microscope of a single group of masks is presented on figure 5.4, where the darker zones correspond to the Cr deposition. The shapes and sizes of each mask in a group were chosen with different purposes. For instance, arrays of holes, parallel or diagonal, with sizes from 8 to 50 μm for pin the emission to them and obtain spatial decorrelation. The same occurs with arrays of

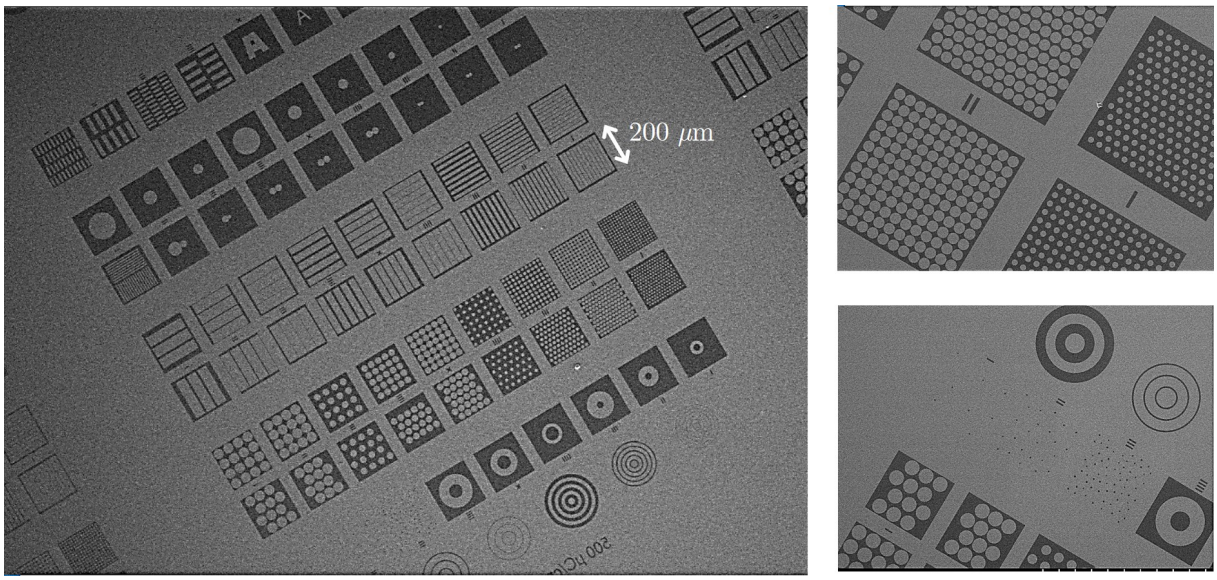

Figure 5.4. Picture under microscope of the array of masks used. The darker zones correspond to the filtering Cr deposition, that provide around 90% of losses. The size of each mask is 200 mum, and they are arranged in a 9×9 pitch

parallel periodic lines. More complex masks were done, such as arrays of rings or even letters, for improve the suppression of off-axis modes and to test our SIC. It is important to point out that the sample region between different masks, where no absorptive mask is present, can be used for making a reference point with the homogeneous gain condition. Experimentally we can use these regions simply by shifting transversally the sample with respect to the pump axis.

First of all, we test the absorptive masks by operating the gain mirror in a VECSEL cavity closed by an HR plane mirror, thus aiming at CW emission. We demonstrate that VECSEL lasing emission can be achieved when the mask patterns consist of periodical holes or lines, but also when more complex patterns are imposed, such as a letter. When using the saturable absorber, not all these patterns lead to lasing emission anymore. However, by choosing the proper size of mask, a balance between losses, and therefore, output power can be obtained. We provide a proof-of-principle of a multiplexed source of TLS. That is, several hot spots in the gain mirror section emitting decorrelated TLS.

5.3.1 VECSEL continuous wave emission with absorptive mask

Cr layer increase the losses due to the pump absorption. Then, in order to verify how the emission of our VECSEL will be affected, in terms of imaging condition and pumping power, a 95% reflectivity mirror was used instead of the SESAM. In this condition, only CW emission may be obtained. As a rule of thumb, the larger the absorptive mask area,

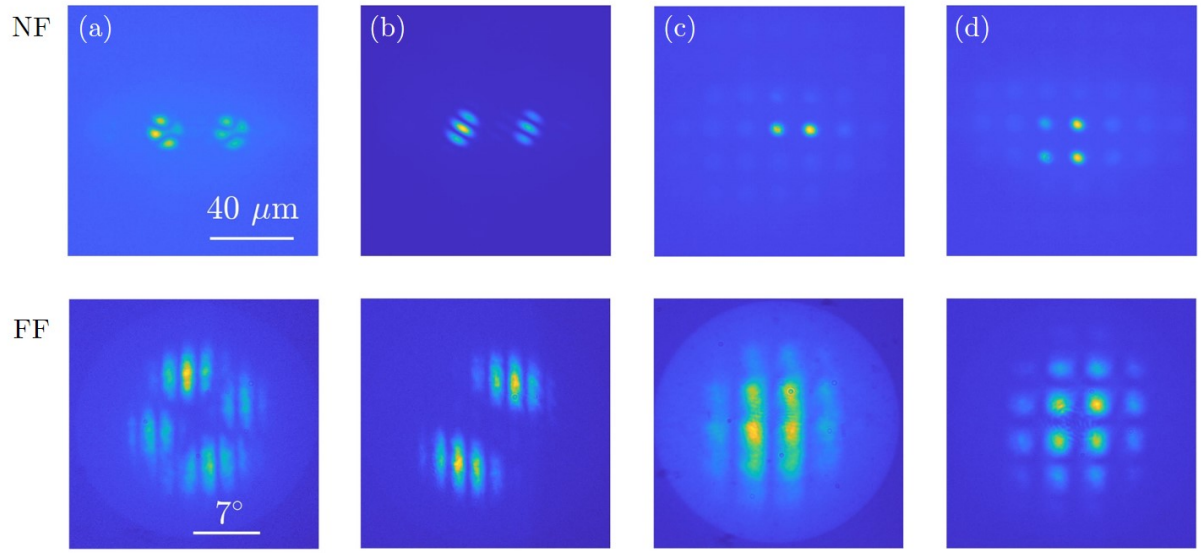

Figure 5.5. Laser emission using masks with array of circular holes. (a) and (b) are different scenarios wit the 15 μm holes array. (c) and (d) for 8μm diameter holes.

the higher the threshold for lasing in terms of pump power, and the lower the output power.

We start by testing masks with an array of holes. Emission was obtained for all the sizes, from diameters of 40 μm to the smaller one 8 μm. Figure 5.5 present different situations for holes diameter of 15 μm (a-b) and 8 μm (c-d). In the first case, the holes are separated 30 μm from its diameter and only two holes are pumped, in the second situation four holes are pumped. P_p is set at 115 mW. Close to SIC, laser emission is only observed for a short range (less than 5 μm) in terms of the position of the last mirror (the distance called L_4 in Chapter 2).

In panel a, we show emission of a mode TEM_{11} is observed from each hot spots. The corresponding far-field reveals a pattern profile homothetic to a mode TEM_{11} with an intensity modulation in form of vertical rolls due to the duplicated emission at the two hot spots. When approaching $B \rightarrow 0$ by increasing x value, different spatial structures appear. In panel b, the two hot spots emit a couple of counterpropagating tilted waves, whose interference fringes remain confined within the hot spots. Both hot spots emit tilted waves with the same angle and direction, accordingly the corresponding far-field reveals two spots which are modulated by vertical fringes corresponding to the interference of the two hot spots emission. Fundamental Gaussian emission (TEM_{00}) has also been observed, for all the sizes of holes arrays. In panel c and d 8 μm hot spots with 13 μm separation, and the pump area covers 4 of them. Panel b shows the

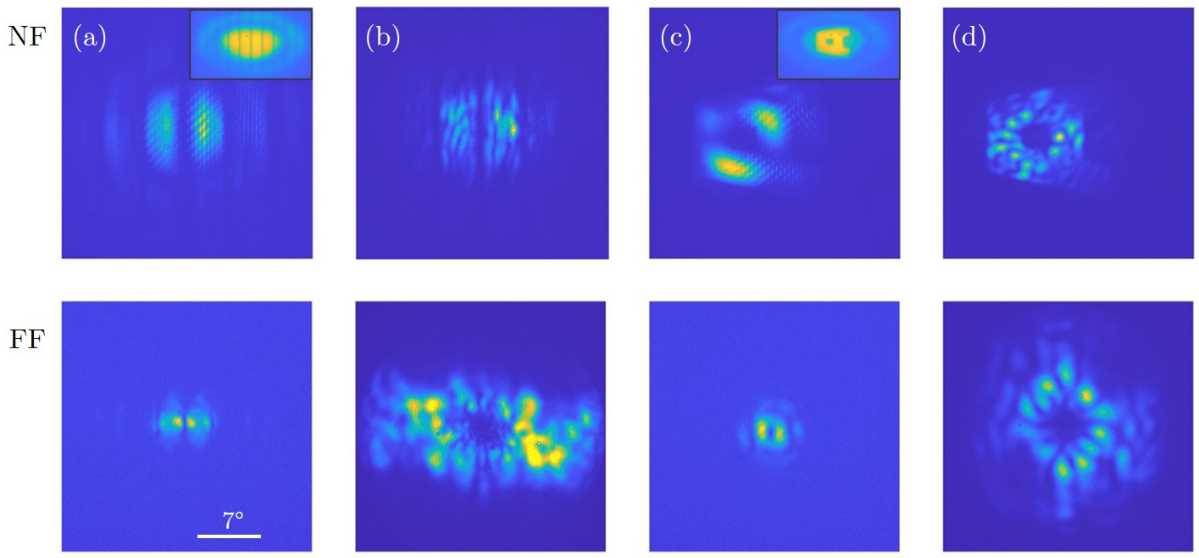

Figure 5.6. Laser emission using complex masks far and close to SIC. (a)-(b) correspond to the 2 μm vertical lines with separation of 30 μm. (c) and (d) are for the letter **A** with dimensions 50×50 μm and width of 15 μm. The insets on (a) and (b) correspond the spontaneous emission of the corresponding mask.

emissions of just two spots, creating vertical stripes which modulate the Gaussian spot in the far-field profile. When 4 hot spots on a square geometry are emitting Gaussian beams, the Gaussian spot in the far field is modulated both horizontally and vertically, thus resulting in a grid shaped pattern.

More complex masks were analyzed as well. Some examples are presented in figure 5.6, for different positions of the HR mirror closing the VECSEL cavity. First two panels show the emission using a mask of 2 μm separated by 30 μm, with a difference of 3.5 μm in x. In (a), the near field emission has a TEM_{10} structure, with two lobes cut by the Cr lines. Its FF shows a similar structure with a numerical aperture of 4°. By shifting the mirror closer to SIC, then complex patters are emitted by the lines. Because we are approaching SIC, the Cr mask becomes more visible in the near field emission profile. The corresponding non homothetic FF profile reveals a complex structure filling horizontally the full NA available (19.5°). Something similar happens when using a mask with the letter **A**, having dimensions of 50×50 μm and 15 μm width (panels c-d 5.6). Far from SIC, an annular pattern appears in the near field deformed by the frontiers of the letter shape, with a similar FF profile of small angle (3.5°). Once more, by getting to SIC, the letter profile becomes sharper, and a complex emission appears. This time it does fill the full FF.

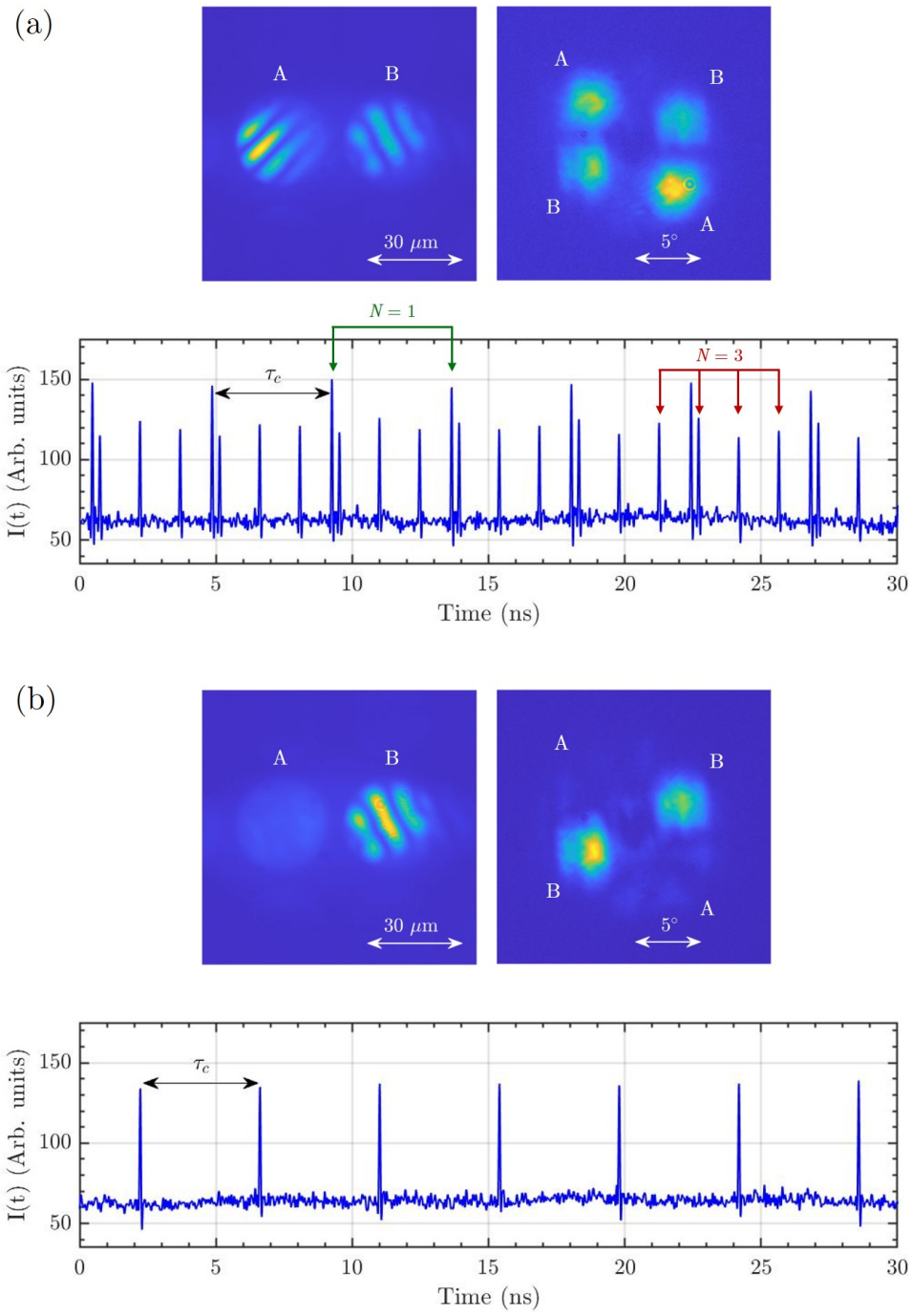

Figure 5.7. Spatio-temporal behavior of a PML multiplex VECSEL, using a 30 μm holes mask. NF and FF show the full emission obtained with the Flat-top beam. In (a), P_p = 160 mW, the two pumped holes emit orthogonal TWs with 3.5° angle in FF. The corresponding time trace is composed of two different trains of pulses with N_A = 3 and N_B = 1. In (b) the P_p is reduced to 152 mW and the hole A is turned off, leaving just the panel B operating with N_B = 1.

5.4 Multiplex source of localized pulses

When the HR mirror is replaced by the SESAM, losses in the external cavity are increased significantly and no laser emission could be obtained close to SIC when using the smallest shapes of masks, such as the array of 8 μm holes. For instance, with the array of 8 μm holes no lasing emission has been achieved. Even though, for hole sizes larger than 30 μm diameter, TLS emission was achieved. The separation distance was the same as its diameter, thus only two holes were inside the pump area. Despite this low number of hot spots, the result of this experiment provides proof of principle for a multiplex source of localized pulses.

The VECSEL cavity is set close to SIC with $-1\,\text{mm} < \Delta z < 0$ while the detuning between the two microcavities is raised to $\delta\lambda = 9$ nm. For these parameters, the two hot spots emit a couple of counterpropagating tilted waves whose direction may be different for each spot. Since we are close to SIC, the system is azimuthally degenerated, and it's possible to select the azimuthal directions of the tilted waves of each hole by tilting the SESAM position. In Figure 5.7 the tilted waves direction from one hot spot is orthogonal to the one emitted from the other spots. The near field fringes are strictly limited within the hot spots. In the time domain, the full trace is composed by two different signals, with different number of pulses. The time trace in panel a shows the combination of a train with $N = (N_A, N_B) = (3, 1)$. Since the number of pulses is different in each train, then the round-trip suffers an small variation, and the trigger scope is not able to trig both signals at the same time. Moreover, in the time trace can be observed that the intensity amplitude is not the same for such trains. Therefore, we are in presence of a spatio-temporal decorrelation which is dependent only of the main parameter control: P_p. When reducing P_p it is possible to switch off the emission of one of the holes, keeping the remaining with the solution . Lower panel in Fig. 5.7 shows the remaining of the left hole emission, pulsating with $N_B = 1$.

When decreasing $\delta\lambda$ to 8 nm, these tilted waves are temporally localized, featuring generalized multistability between the trivial solution and pulsating solutions with a number of pulses per round-trip ranging from $N = 0, \cdot, 8$. Bistable regime of the system is achieved when $T = 22°$, then, $\delta\lambda = 8$ nm. For monitoring the time dynamics of the independent holes emission, the detection of 5.1 was used again, collecting independently Channel 1 (hole A) and 2 (hole B). Multistability appears for the same parameters of the system. Figure 5.8 presents the spatio-temporal maps of the total

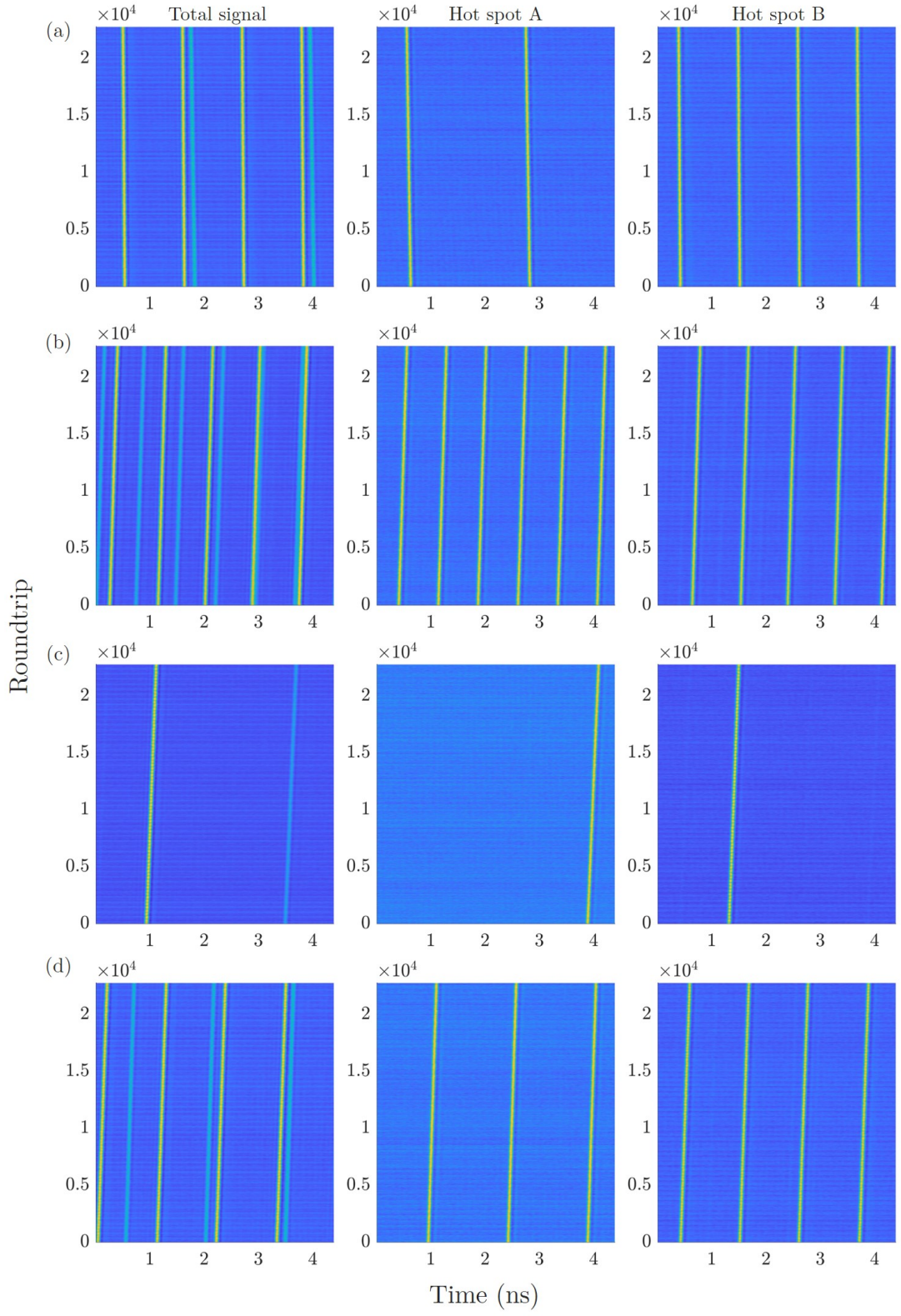

Figure 5.8. Spatio-temporal maps of the total signal (left), and channels 1 (middle) and 2 (right), showing the multistability of the multiplex VECSEL when $\delta\lambda = 8$ nm, and $P_p = 185$ mW. The solutions with $N =$ (a) $(2, 4)$, (b) $(6, 5)$, (c) $(1, 5)$, and (d) $(3, 4)$, are some of the states in coexistence, also with the off-solution.

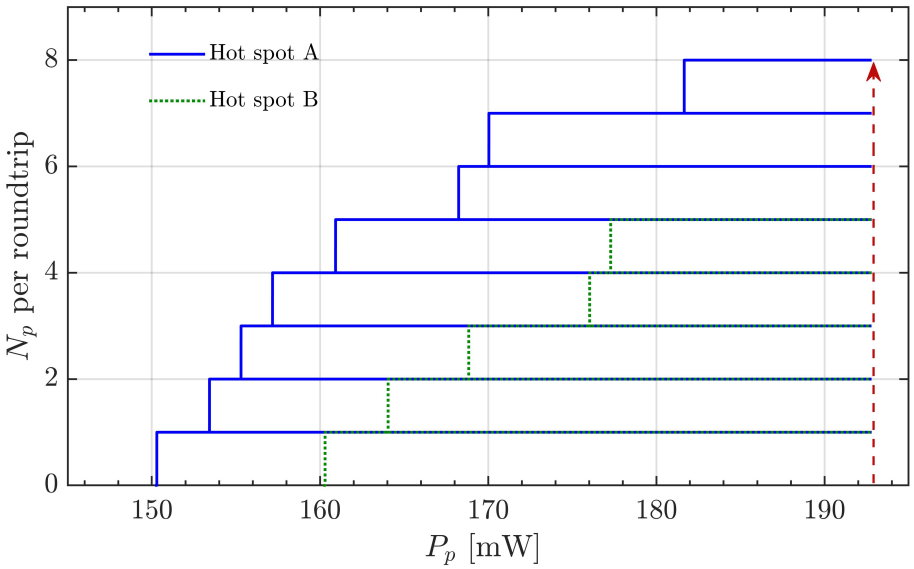

Figure 5.9. Bifurcation diagram showing the stability for each solution N_1 (blue) and N_2 (green). The lasing threshold is at 192.5 mW (red dashed line).

emission signal and the two independent channels taken at the same time, for $P_p = 185$ mW. In first panel, the total signal shows two trains of pulses with different intensities. They correspond to the solutions $N = (N_1, N_2) = (2, 4)$, and they can be independently observed in its respective channel scope. It's clear they do not interact inside the cavity, since the signals are not perturbed by the other. The same happens for the rest of the panels, b-d, showing $N = (6, 5)$, $(1, 1)$, and $(3, 4)$, respectively. All these solutions coexist with the off-state in each spot. Noteworthy, regardless the number of pulses emitted, the pulse timing from each spot is almost the same. Since we know that the number of pulses emitted per round-trip affects the timing of the pulses [Javaloyes, 2016b], we conclude that must be a coupling between the two spots through the active medium.

The stability of each pulsating state emitted by each spot can be tested by changing the pumping current as explained in Chap.3. The bifurcation diagram of these states emitted by each one of the two spots is presented in 5.9. We start from the off-solution, increasing the pump power up to lasing threshold, 192.5 mW. Each hot spot jumps into different solutions with $N = (8, 5)$. As P_p decreases, each solution losses its stability and the number of pulses is reduced by one. This happens for P_p values of 181 mW for hot spot A, and 177.3 mW. The new solution are, $N_A = 7$ and $N_B = 4$, respectively. This can be done progressively until one pulse per round-trip is emitted by hot spot B. Figure 5.9 indicates that the pump limits for multistability are different for each spot.

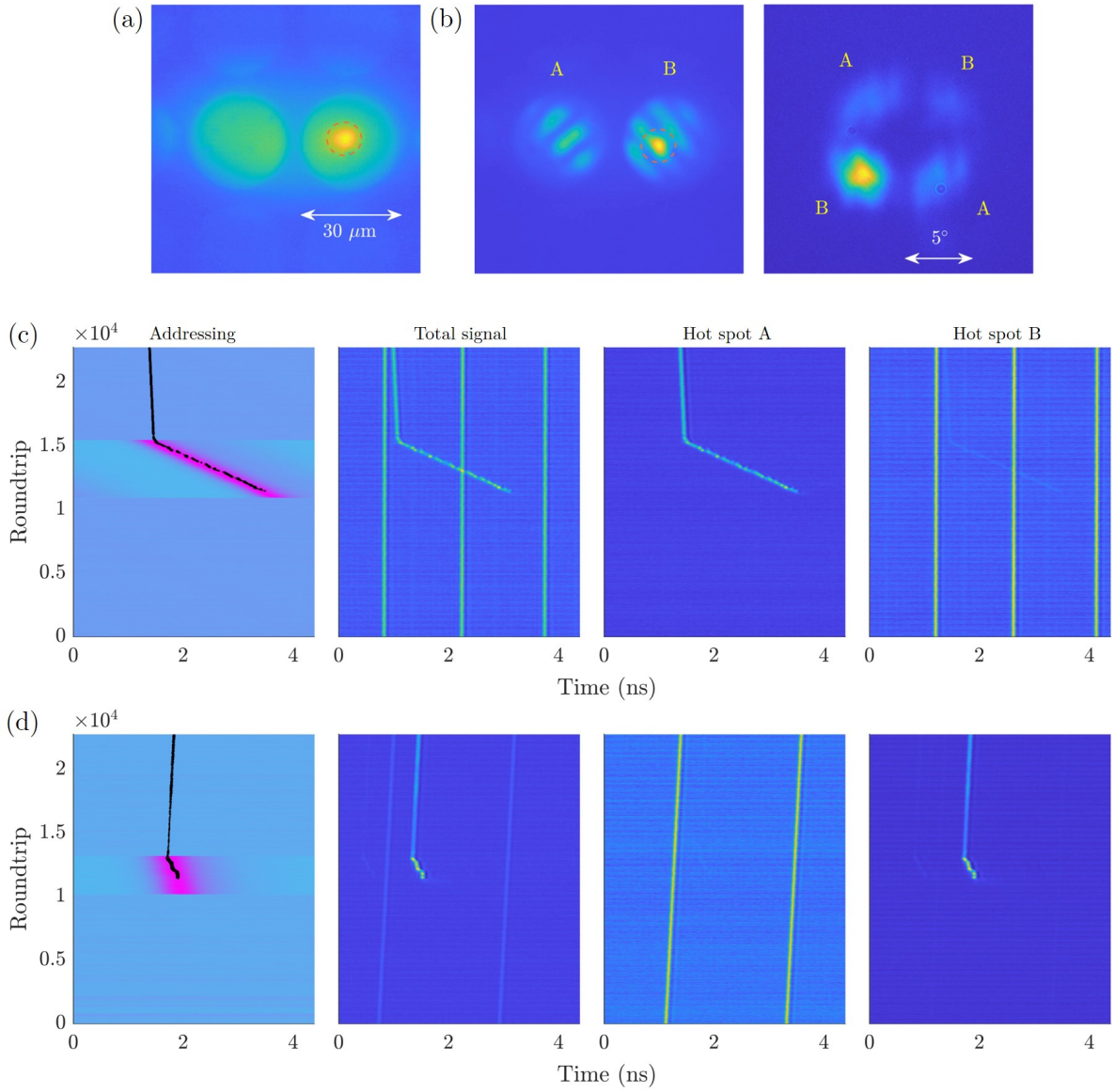

Figure 5.10. (a) Spontaneous emission of the mask, showing the writing beam position. (b) NF and FF in lasing operation, leaving the writing beam on. In (c) and (d) ot is presented the writing of a TLS in hot spot A and B, respectively.

5.4.1 Gain-pinned TLS addressing

In Chapter 3 it was shown that a pulsating writing beam can address TLS in the pattern regime, provided that such pulse has a repetition rate close to the cavity round-trip. Then, with the same technique we aim at observing the same effect. We set the VECSEL in a regime where one of the hot spots is in the off solution, while the other is pulsating. The writing beam targets only one of the two hot spots. Because we have tilted wave emission, we know from Chapter 3 that the addressing beam needs to target the region where bright fringes appear as a result of the interference of the two counterpropagating tilted waves. The position of the writing beam is shown in figure 5.10a. Because we are dealing with temporally localized structures, we expect to turn one pulse per round-trip solution in hot spot B and that this solution remains once the perturbation is removed. We also expect that this operation will not affect the TLS emitted by the other spot.

Figure 5.10 presents two scenarios. In first panel, the system is prepared in such way the total number of pulses is $N = (0, 3)$. The writing beam is open with the gate at the round-trip 10000, and a pulse in spot B is created and follows the timing of the perturbation pulse. After, this latter disappears close to the round-trip 15500, the solution $N = (1, 3)$ remains stable. The localized pulse in spot B, changes is timing and evolves with the same timing as the pulses in spot A. This locking of the timing of TLS discloses again a coupling between the emission from the two spots. This coupling affects the timing of the structures but it is weak enough to enable independent addressing of TLS in the two spots. In panel b. we realize a similar operation: the system is set in the solution $N = (2, 0)$. Then the gate opens at the round-trip 10200, and after some, a pulse in spot B switches on. At the round-trip 13200 the gate is closed, and the remaining pulse in follows stable its own path. These experimental evidences reveal that the system can sustain spatially uncorrelated emission, a further confirmation of operation close to SIC. In conclusion, we have shown that several sources of TLS can be printed onto the same gain sample and addressed individually in space and in time.

5.5 Conclusions

We have demonstrated that gain-pinned spatio-temporal decorrelated states are possible in a self-imaging PML VECSEL, provided that the gain is locally shaped. These PML states can be operated in the temporally localized regime. We have explored two solutions for gain pinning the emission by creating hot spots in the gain surface. The first

was done by introducing two external narrow pump beams in addition to the flat-top pump. The intensity of such beams had to be enough for being in the multistable regime, while the intensity of the main pump had to be reduced below such regime, in order to avoid spatial correlation. Therefore, we demonstrated the emission of two different tilted waves, located in each hot spot, that emit decorrelated TLS. On the other hand, the use of Cr mask filter on the gain facet allowed to create as well different hot spots. By using an array of 30 μm holes, we were able to have two hot spots inside the pump area, and each hot spot emits a different set of tilted waves, with orthogonal direction each other. These tilted waves were operated in the PML TLS regime, and we demonstrate that spatial and temporal bistability is possible. As it was done in Chapter 3, we demonstrated the TLS one hot spot can be independently addressed without affecting the spatio-temporal dynamics of the other. Even though the mask size was chosen for achieve emission and obtain enough output power, more scenarios could be explored. For instance, mask with more denser amount of holes, provided that the output signal of each hot spot is reduced. On the other hand, a suitable option is to introduce Cr mask in the SESAM facet, avoiding pump power absorption. Furthermore, so far it was not possible to obtain Gaussian emission in each hot-spot, due to the amount of losses. Nevertheless, the tilted waves observed in section 5.4, present all the requirements for being gain-pinned spatio-temporal localized states. In principle these gain-pinned spatio-temporal states, even though they are not an on-axis solution, appear in the regime of degeneracy. If one could increase the pumped area for achieving emission from more hot spots on the mask, the VECSEL could be operated as an all-optical buffer, similar to the one based on light bullets.

CHAPTER 6

General conclusions and perspectives

In this work we have demonstrated that a broad area VECSEL, composed by a gain mirror and a saturable absorber, can emit patterns when the self-imaging condition is approached. These spatial structures exhibit non homothetic far-field and near-field profiles. In the time domain these patterns are temporally localized pulses, hence they can be individually addressed by pump pulses.

On the base on previous works performed in semiconductor lasers and in collaboration with the groups of IES in Montpelier and C2N in Paris, we have followed a road map to develop a VECSEL satisfying the requirements for achieving both spatial and temporal localization. Gain mirror and SESAM samples were designed accordingly and preliminary results have shown that temporal LS can be obtained with VECSEL. Nevertheless, no spatial emission beyond Gaussian fundamental mode was observed in this first set up. We have understood that for achieving large aspect-ratio VECSEL several points needed to be addressed: *i)* the effect of thermal/electronic lens on the gain mirror which affects significantly the SIC as calculated for the cold cavity, *ii)* the homogeneously pumped area on the gain section and *iii)* external cavity optical design for achieving the largest numerical aperture and minimizing anisotropies and aberrations. These issues were solved leading to *i)* an observational criterium for assessing SIC by shifting the position of one lens and the SESAM. Moreover, our ABCD matrix analysis has enabled to relate the matrix elements to these positions. *ii)* a flat-top pump profile. *iii)* a 8f telecentric cavity with an L shape and a magnification of two between the SESAM and the gain mirror for enhancing saturation fluence ratio between the latter and the former. The cavity was characterized by ZEMAX simulation tool.

When approaching SIC we have observed that fundamental Gaussian emission gives

way to pattern with non homothetic far-field and near-field profile. The characteristics of these patterns were depending on parameter C of the ABCD roundtrip matrix. When $C < 0$, on-axis patterns appear for $B \rightarrow 0^+$ and they present an hexagonal-like structure in the near field, whose origin comes from the interference between a high intensity on-axis component and high numerical aperture tilted waves. On the other hand, when $C > 0$, patterns appear for $B \rightarrow 0^-$ and they consist of a set of counterpropagating tilted waves with opposite transverse wavevectors. These wavevectors share the same modulus and they draw a circle in the far field profile. When the rotational symmetry is broken by some anisotropy in the cavity, only two spots are observed in the far field and a roll pattern appears in the near-field. Tilted wave emission is explained by lens aberrations, namely the longitudinal focal shift of the collimator facing the SESAM.

When the micro-cavity resonances of the gain λ_G and the SESAM λ_{SA} are properly detuned, these patterns are temporal localized structures in time domain and they can be individually addressed by an external pump perturbation, whose repetition rate matches with the cavity FSR. Therefore, we have reported the first observation of temporally localized patterns.

When reducing $C \sim 0$ we observe different coexisting spatio-temporal lasing states characterized by different spatial profiles each one pulsating at a different rate per round-trip. Hence, this full spatio-temporal platform enables the experimental analysis of novel laser regimes with characteristics that are approaching the ones of light-bullets.

These experimental results are the first observations in a truly spatio-temporal lasers, exploiting both spatial and temporal large aspect-ratio condition. Hence, these results will feed theoretical analysis of such a complete platform with possible connections to general non linear dynamics behaviors. While a model is almost ready for describing the tilted wave appearance, only preliminary steps are taken for a theoretical explanation of hexagonal on-axis patterns which are unexpected in such a system. The results obtained for $C \sim 0$ have not yet been considered for a theoretical analysis. We expect that the observations realized will be a strong motivation for analyzing spatio-temporal dynamics in lasers.

On the other hand, several parameters are still to be explored. First of all, the spherical aberration signs which fixes the characteristics of the wavefront when the system is very close to SIC. So far, we were not able to find a lens capable of replacing the collimator facing the SESAM and behaving differently in terms of aberrations.

Another interesting parameter for spatial localization would be the confinement factor of the micro-cavities. More samples are being prepared for increasing this parameter by the group of IES and C2N, For instance, by adding much more top Bragg mirrors, Γ can go above 50. The withdraw is now, that the SESAM GaAS-831 will not saturate. Furthermore, this drastic increase in Γ will reduce the micro-cavity bandwidth and the width of a possible pulse will increase by one or two orders of magnitude. One solution indeed is to increase then parameter Γ but not too far from the current values we have.

We presented an alternative method for manipulating the temporal LS in a VECSEL using time delayed feedback as a solution selector, for reinforcing or hinder the appearance of one of the multiple coexisting PML solutions of the system. We built a coupled second external cavity of round-trip τ_f, in order to send back a small portion of the emission ($< 0.1\%$). The length of this cavity was set to a fraction of the VECSEL round-trip τ_c, in order to match $\tau_f = \tau_c/n$. We operated the system in the temporal LS regime for the fundamental Gaussian solution, when $C > 0$. This feedback perturbation allowed to turn off one pulse on the emission when τ_f is slightly shorter than τ_c/n, provided that the number of pulses inside the cavity N is a multiple of n. These results, in collaboration with the groups of Spain and Germany, were theoretically confirmed using the delay differential equations model for a PML laser in a ring cavity. Together with the addressing method presented in Chapter 3, clearly demonstrate that our PML pulses are localized structures.

Finally, we demonstrated the first steps towards gain-pinned spatio-temporal LS. We realized that spatio-temporal decorrelation in our VECSEL, even though does not appear spontaneously, can be induced my adding hot spots into the gain profile. These spots were generated by *i)* modulating the pump profile and *ii)* by adding an absorptive Cr mask filter on top of the gain facet. Thanks to these hot-spots, it was possible to obtain spatio-temporal decorrelated states operating in the temporal LS regime. Cr mask results were obtained using the mask of 30 μm holes, where only two of them fit inside the pumping area. Even if we succeed to generate a proof of principle of a multiplexed source of temporal LS, it is necessary to increase the number of hot spots for having more sources of temporal LS on the same VECSEL. It is important noting that a three dimensional buffer, as the one shown in the first chapter, can be realized only with these multiple hot-spots generating temporal LS. Hence, this path is a very promising one as an alternative to one of the most important applications of light bullets. Moreover these hot spots are coupled between them, though they are capable of emitting

an independent number of pulses. Hence, we believe that they may be an interesting configuration for realizing multiple frequency combs for LIDAR and sensing.

Bibliography

[Ackemann, 2021] Ackemann, T., Labeyrie, G., Baio, G., Krešić, I., Walker, J. G., Costa Boquete, A., Griffin, P., Firth, W. J., Kaiser, R., Oppo, G.-L., et al. (2021). Self-organization in cold atoms mediated by diffractive coupling. *Atoms*, 9(3):35. (Cited on page 60.)

[Ackemann, 1994] Ackemann, T. and Lange, W. (1994). Non- and nearly hexagonal patterns in sodium vapor generated by single-mirror feedback. *Physical Review A*, 50(6):R4468–R4471. (Cited on page 3.)

[Ackemann, 2001] Ackemann, T. and Lange, W. (2001). Optical pattern formation in alkali metal vapors: Mechanisms, phenomena and use. *Applied Physics B*, 72(1):21–34. (Cited on page 60.)

[Arecchi, 1995] Arecchi, F. T. (1995). Optical morphogenesis: pattern formation and competition in nonlinear optics. *Physica D*, page 26. (Cited on pages 2, 3, and 5.)

[Arecchi, 1999] Arecchi, F. T., Boccaletti, S., and Ramazza, P. (1999). Pattern formation and competition in nonlinear optics. *Physics Reports*, 318(1-2):1–83. (Cited on page 60.)

[Arecchi, 1993] Arecchi, F. T., Boccaletti, S., Ramazza, P. L., and Residori, S. (1993). Transition from boundary- to bulk-controlled regimes in optical pattern formation. *Physical Review Letters*, 70(15):2277–2280. (Cited on page 2.)

[Arnaud, 1969] Arnaud, J. A. (1969). Degenerate Optical Cavities. *Applied Optics*, 8(1):189. (Cited on pages 40 and 79.)

[Arsenijević, 2013] Arsenijević, D., Kleinert, M., and Bimberg, D. (2013). Phase noise and jitter reduction by optical feedback on passively mode-locked quantum-dot lasers. *Applied Physics Letters*, 103(23):231101. (Cited on page 86.)

[Astrov, 2001] Astrov, Y. A. and Purwins, H.-G. (2001). Plasma spots in a gas discharge system: birth, scattering and formation of molecules. *Physics Letters A*, 283(5-6):349–354. (Cited on page 4.)

[Baili, 2009] Baili, G., Morvan, L., Alouini, M., Dolfi, D., Bretenaker, F., Sagnes, I., and Garnache, A. (2009). Experimental demonstration of a tunable dual-frequency semiconductor laser free of relaxation oscillations. *Optics letters*, 34(21):3421–3423. (Cited on page 22.)

[Ball, 2015] Ball, P. (2015). Forging patterns and making waves from biology to geology: a commentary on turing (1952)'the chemical basis of morphogenesis'. *Philosophical Transactions of the Royal Society B: Biological Sciences*, 370(1666):20140218. (Cited on page 2.)

[Barland, 2002] Barland, S., Tredicce, J. R., Brambilla, M., Lugiato, L. A., Balle, S., Giudici, M., Maggipinto, T., Spinelli, L., Tissoni, G., Knödl, T., Miller, M., and Jäger, R. (2002). Cavity solitons as pixels in semiconductor microcavities. *Nature*, 419(6908):699–702. (Cited on pages 7, 9, and 96.)

[Blin, 2017] Blin, S., Paquet, R., Myara, M., Chomet, B., Le Gratiet, L., Sellahi, M., Beaudoin, G., Sagnes, I., Ducournau, G., Latzel, P., et al. (2017). Coherent and tunable thz emission driven by an integrated iii–v semiconductor laser. *IEEE Journal of Selected Topics in Quantum Electronics*, 23(4):1–11. (Cited on page 97.)

[Born, 2013] Born, M. and Wolf, E. (2013). *Principles of optics: electromagnetic theory of propagation, interference and diffraction of light*. Elsevier. (Cited on page 77.)

[Bowman, 1998] Bowman, C. and Newell, A. (1998). Natural patterns and wavelets. *Reviews of Modern Physics*, 70(1):289. (Cited on page 1.)

[Caboche, 2009a] Caboche, E., Barland, S., Giudici, M., Tredicce, J., Tissoni, G., and Lugiato, L. (2009a). Cavity-soliton motion in the presence of device defects. *Physical Review A*, 80(5):053814. (Cited on pages 9 and 97.)

[Caboche, 2009b] Caboche, E., Pedaci, F., Genevet, P., Barland, S., Giudici, M., Tredicce, J., Tissoni, G., and Lugiato, L. (2009b). Microresonator defects as sources of drifting cavity solitons. *Physical review letters*, 102(16):163901. (Cited on page 9.)

[Camelin, 2016] Camelin, P., Javaloyes, J., Marconi, M., and Giudici, M. (2016). Electrical addressing and temporal tweezing of localized pulses in passively-mode-locked semiconductor lasers. *Physical Review A*, 94(6):063854. (Cited on pages 15, 63, 87, and 89.)

[Camelin, 2018] Camelin, P., Schelte, C., Verschelde, A., Garnache, A., Beaudoin, G., Sagnes, I., Huyet, G., Javaloyes, J., Gurevich, S. V., and Giudici, M. (2018). Temporal localized structures in mode-locked vertical external-cavity surface-emitting lasers. *Optics Letters*, 43(21):5367. (Cited on pages 27, 28, and 87.)

[Cao, 2019] Cao, H., Chriki, R., Bittner, S., Friesem, A. A., and Davidson, N. (2019). Complex lasers with controllable coherence. *Nature Reviews Physics*, 1(2):156–168. (Cited on page 87.)

[Cermak, 2010] Cermak, P., Triki, M., Garnache, A., Cerutti, L., and Romanini, D. (2010). Optical-feedback cavity-enhanced absorption spectroscopy using a short-cavity vertical-external-cavity surface-emitting laser. *IEEE Photonics Technology Letters*, 22(21):1607–1609. (Cited on page 22.)

[Chomet, 2018] Chomet, B., Zhao, J., Ferrieres, L., Myara, M., Guiraud, G., Beaudoin, G., Lecocq, V., Sagnes, I., Traynor, N., Santarelli, G., Denet, S., and Garnache, A. (2018). High-power tunable low-noise coherent source at 106 μm based on a surface-emitting semiconductor laser. *Applied Optics*, 57(18):5224. (Cited on page 22.)

[Cisternas, 2020] Cisternas, J., Escaff, D., Clerc, M. G., Lefever, R., and Tlidi, M. (2020). Gapped vegetation patterns: Crown/root allometry and snaking bifurcation. *Chaos, Solitons & Fractals*, 133:109617. (Cited on page 4.)

[Cocquelin, 2009] Cocquelin, B., Holleville, D., Lucas-Leclin, G., Sagnes, I., Garnache, A., Myara, M., and Georges, P. (2009). Tunable single-frequency operation of a diode-pumped vertical external-cavity laser at the cesium d2 line. *Applied Physics B*, 95(2):315–321. (Cited on page 22.)

[Coullet, 2000] Coullet, P., Riera, C., and Tresser, C. (2000). Stable Static Localized Structures in One Dimension. *Physical Review Letters*, 84(14):3069–3072. (Cited on page 7.)

[Cross, 1993] Cross, M. C. and Hohenberg, P. C. (1993). Pattern formation outside of equilibrium. *Reviews of modern physics*, 65(3):851. (Cited on page 1.)

[D'Alessandro, 1991] D'Alessandro, G. and Firth, W. J. (1991). Spontaneous hexagon formation in a nonlinear optical medium with feedback mirror. *Physical Review Letters*, 66(20):2597–2600. (Cited on page 3.)

[Edmundson, 1992] Edmundson, D. and Enns, R. (1992). Robust bistable light bullets. *Optics letters*, 17(8):586–588. (Cited on page 17.)

[Engelborghs, 2002] Engelborghs, K., Luzyanina, T., and Roose, D. (2002). Numerical bifurcation analysis of delay differential equations using dde-biftool. *ACM Transactions on Mathematical Software (TOMS)*, 28(1):1–21. (Cited on page 93.)

[Faraday, 1831] Faraday, M. (1831). On the forms and states assumed by fluids in contact with vibrating elastic surfaces. *Philos. Trans. R. Soc. London*, 121:39–346. (Cited on page 1.)

[Fauve, 1990] Fauve, S. and Thual, O. (1990). Solitary waves generated by subcritical instabilities in dissipative systems. *Physical review letters*, 64(3):282. (Cited on pages 4 and 7.)

[Firth, 1996] Firth, W. and Scroggie, A. (1996). Optical bullet holes: robust controllable localized states of a nonlinear cavity. *Physical review letters*, 76(10):1623. (Cited on page 5.)

[Gardner, 1967] Gardner, C. S., Greene, J. M., Kruskal, M. D., and Miura, R. M. (1967). Method for solving the korteweg-devries equation. *Physical review letters*, 19(19):1095. (Cited on page 6.)

[Garnache, 2002] Garnache, A., Hoogland, S., Tropper, A., Sagnes, I., Saint-Girons, G., and Roberts, J. (2002). Sub-500-fs soliton-like pulse in a passively mode-locked broadband surface-emitting laser with 100 mw average power. *Applied Physics Letters*, 80(21):3892–3894. (Cited on page 16.)

[Genevet, 2008] Genevet, P., Barland, S., Giudici, M., and Tredicce, J. R. (2008). Cavity Soliton Laser Based on Mutually Coupled Semiconductor Microresonators. *Physical Review Letters*, 101(12):123905. (Cited on pages 11, 21, 25, and 96.)

[Genevet, 2010] Genevet, P., Turconi, M., Barland, S., Giudici, M., and Tredicce, J. R. (2010). Mutual coherence of laser solitons in coupled semiconductor resonators. *The European Physical Journal D*, 59(1):109–114. (Cited on page 12.)

[Gibbs, 1985] Gibbs, H. (1985). *Optical bistability: controlling light with light*. Academic Press. (Cited on page 4.)

[Gollub, 1999] Gollub, J. P. and Langer, J. S. (1999). Pattern formation in nonequilibrium physics. *Reviews of Modern Physics*, 71(2):S396. (Cited on page 1.)

[Grelu, 2012] Grelu, P. and Akhmediev, N. (2012). Dissipative solitons for mode-locked lasers. *Nature Photonics*, 6(2):84–92. (Cited on pages 6 and 7.)

[Grynberg, 1988] Grynberg, G., Le Bihan, E., Verkerk, P., Simoneau, P., Leite, J. R., Bloch, D., Le Boiteux, S., and Ducloy, M. (1988). Observation of instabilities due to mirrorless four-wave mixing oscillation in sodium. *Optics communications*, 67(5):363–366. (Cited on page 3.)

[Guina, 2017] Guina, M., Rantamäki, A., and Härkönen, A. (2017). Optically pumped VECSELs: review of technology and progress. *Journal of Physics D: Applied Physics*, 50(38):383001. (Cited on page 22.)

[Gurevich, 2017] Gurevich, S. V. and Javaloyes, J. (2017). Spatial instabilities of light bullets in passively-mode-locked lasers. *Physical Review A*, 96(2):023821. (Cited on page 18.)

[Gustave, 2017] Gustave, F., Radwell, N., McIntyre, C., Toomey, J., Kane, D., Barland, S., Firth, W., Oppo, G.-L., and Ackemann, T. (2017). Observation of Mode-Locked Spatial Laser Solitons. *Physical Review Letters*, 118(4):044102. (Cited on pages 17 and 19.)

[Hachair, 2008] Hachair, X., Barbay, S., Elsass, T., Sagnes, I., and Kuszelewicz, R. (2008). Transverse spatial structure of a high Fresnel number Vertical External Cavity Surface Emitting Laser. *Optics Express*, 16(13):9519. (Cited on page 74.)

[Hachair, 2004] Hachair, X., Barland, S., Furfaro, L., Giudici, M., Balle, S., Tredicce, J. R., Brambilla, M., Maggipinto, T., Perrini, I. M., Tissoni, G., and Lugiato, L. (2004). Cavity solitons in broad-area vertical-cavity surface-emitting lasers below threshold. *Physical Review A*, 69(4):043817. (Cited on page 23.)

[Haelterman, 1992] Haelterman, M., Trillo, S., and Wabnitz, S. (1992). Additive-modulation-instability ring laser in the normal dispersion regime of a fiber. *Optics letters*, 17(10):745–747. (Cited on page 12.)

[Hansen, 1988] Hansen, U. and Yuen, D. A. (1988). Numerical simulations of thermal-chemical instabilities at the core–mantle boundary. *Nature*, 334(6179):237–240. (Cited on page 1.)

[Haus, 2000] Haus, H. A. (2000). Mode-locking of lasers. *IEEE Journal of Selected Topics in Quantum Electronics*, 6(6):1173–1185. (Cited on page 14.)

[Hegarty, 1999] Hegarty, S. P., Huyet, G., Porta, P., McInerney, J. G., Choquette, K. D., Geib, K. M., and Hou, H. Q. (1999). Transverse-mode structure and pattern formation in oxide-confined vertical-cavity semiconductor lasers. *Journal of the Optical Society of America B*, 16(11):2060. (Cited on page 74.)

[Henry, 1982] Henry, C. (1982). Theory of the linewidth of semiconductor lasers. *IEEE Journal of Quantum Electronics*, 18(2):259–264. (Cited on page 11.)

[Iga, 2000] Iga, K. (2000). Surface-emitting laser-its birth and generation of new optoelectronics field. *IEEE Journal of Selected Topics in Quantum Electronics*, 6(6):1201–1215. (Cited on page 8.)

[Iga, 1988] Iga, K., Koyama, F., and Kinoshita, S. (1988). Surface emitting semiconductor lasers. *IEEE Journal of Quantum Electronics*, 24(9):1845–1855. (Cited on page 8.)

[Ippen, 1994] Ippen, E. P. (1994). Principles of passive mode locking. *Applied Physics B*, 58(3):159–170. (Cited on page 14.)

[Jacquemet, 2007] Jacquemet, M., Domenech, M., Lucas-Leclin, G., Georges, P., Dion, J., Strassner, M., Sagnes, I., and Garnache, A. (2007). Single-frequency cw vertical external cavity surface emitting semiconductor laser at 1003 nm and 501 nm by intracavity frequency doubling. *Applied Physics B*, 86(3):503–510. (Cited on page 22.)

[Jaurigue, 2015] Jaurigue, L., Pimenov, A., Rachinskii, D., Schöll, E., Lüdge, K., and Vladimirov, A. G. (2015). Timing jitter of passively-mode-locked semiconductor lasers subject to optical feedback: A semi-analytic approach. *Physical Review A*, 92(5):053807. (Cited on pages 86 and 92.)

[Javaloyes, 2016a] Javaloyes, J. (2016a). Cavity Light Bullets in Passively Mode-Locked Semiconductor Lasers. *Physical Review Letters*, 116(4):043901. (Cited on pages 18 and 24.)

[Javaloyes, 2016b] Javaloyes, J., Camelin, P., Marconi, M., and Giudici, M. (2016b). Dynamics of Localized Structures in Systems with Broken Parity Symmetry. *Physical Review Letters*, 116(13):133901. (Cited on page 108.)

[Javaloyes, 2017] Javaloyes, J., Marconi, M., and Giudici, M. (2017). Nonlocality induces chains of nested dissipative solitons. *Physical Review Letters*, 119(3):033904. (Cited on page 87.)

[Jewell, 1989] Jewell, J., Scherer, A., McCall, S., Lee, Y.-H., Walker, S., Harbison, J., and Florez, L. (1989). Low-threshold electrically pumped vertical-cavity surface-emitting microlasers. *Electronics Letters*, 25(17):1123–1124. (Cited on page 8.)

[Keller, 2006] Keller, U. and Tropper, A. C. (2006). Passively modelocked surface-emitting semiconductor lasers. *Physics Reports*, 429(2):67–120. (Cited on page 14.)

[Kivshar, 2003] Kivshar, Y. S. and Agrawal, G. (2003). *Optical solitons: from fibers to photonic crystals*. Academic press. (Cited on page 12.)

[Kondo, 1995] Kondo, S. and Asai, R. (1995). A reaction–diffusion wave on the skin of the marine angelfish pomacanthus. *Nature*, 376(6543):765–768. (Cited on page 2.)

[Kuznetsov, 1986] Kuznetsov, E., Rubenchik, A., and Zakharov, V. E. (1986). Soliton stability in plasmas and hydrodynamics. *Physics Reports*, 142(3):103–165. (Cited on page 16.)

[Kuznetsov, 1997] Kuznetsov, M., Hakimi, F., Sprague, R., and Mooradian, A. (1997). High-power (> 0.5-w cw) diode-pumped vertical-external-cavity surface-emitting semiconductor lasers with circular tem/sub 00/beams. *IEEE Photonics Technology Letters*, 9(8):1063–1065. (Cited on page 22.)

[Laskin, 2015] Laskin, A., Juzumas, V., Urniežius, A., Laskin, V., Šlekys, G., and Ostrun, A. (2015). Building beam shaping optics for micromachining. In *Components and Packaging for Laser Systems*, volume 9346, pages 224–232. SPIE. (Cited on page 30.)

[Laurain, 2009] Laurain, A., Myara, M., Beaudoin, G., Sagnes, I., and Garnache, A. (2009). High power single–frequency continuously–tunable compact extended–cavity semiconductor laser. *Optics Express*, 17(12):9503–9508. (Cited on page 31.)

[Laurain, 2010] Laurain, A., Myara, M., Beaudoin, G., Sagnes, I., and Garnache, A. (2010). Multiwatt–power highly–coherent compact single–frequency tunable Vertical–External–Cavity–Surface–Emitting–Semiconductor–Laser. *Optics Express*, 18(14):14627. (Cited on page 22.)

[Le, 1991] Le, H., Di Cecca, S., and Mooradian, A. (1991). Scalable high-power optically pumped gaas laser. *Applied physics letters*, 58(18):1967–1969. (Cited on page 22.)

[Leo, 2010] Leo, F., Coen, S., Kockaert, P., Gorza, S.-P., Emplit, P., and Haelterman, M. (2010). Temporal cavity solitons in one-dimensional Kerr media as bits in an all-optical buffer. *Nature Photonics*, 4(7):471–476. (Cited on pages 12 and 13.)

[Liehr, 2013] Liehr, A. (2013). *Dissipative solitons in reaction diffusion systems*, volume 70. Springer. (Cited on page 2.)

[Lioubashevski, 1999] Lioubashevski, O., Hamiel, Y., Agnon, A., Reches, Z., and Fineberg, J. (1999). Oscillons and propagating solitary waves in a vertically vibrated colloidal suspension. *Physical review letters*, 83(16):3190. (Cited on page 4.)

[Liu, 1999] Liu, X., Qian, L., and Wise, F. (1999). Generation of optical spatiotemporal solitons. *Physical review letters*, 82(23):4631. (Cited on page 17.)

[Lorenser, 2004] Lorenser, D., Unold, H., Maas, D., Aschwanden, A., Grange, R., Paschotta, R., Ebling, D., Gini, E., and Keller, U. (2004). Towards wafer-scale integration of high repetition rate passively mode-locked surface-emitting semiconductor lasers. *Applied Physics B*, 79(8):927–932. (Cited on page 14.)

[Lugiato, 1988] Lugiato, L., Oppo, G.-L., Pernigo, M., Tredicce, J., Narducci, L., and Bandy, D. (1988). Spontaneous spatial pattern formation in lasers and cooperative frequency locking. *Optics communications*, 68(1):63–68. (Cited on page 59.)

[Lugiato, 1987] Lugiato, L. A. and Lefever, R. (1987). Spatial Dissipative Structures in Passive Optical Systems. *Physical Review Letters*, 58(21):2209–2211. (Cited on page 6.)

[Lutgen, 2003] Lutgen, S., Albrecht, T., Brick, P., Reill, W., Luft, J., and Späth, W. (2003). 8-w high-efficiency continuous-wave semiconductor disk laser at 1000 nm. *Applied Physics Letters*, 82(21):3620–3622. (Cited on page 22.)

[Mak, 2003] Mak, W. C., Malomed, B. A., and Chu, P. L. (2003). Interaction of a soliton with a localized gain in a fiber bragg grating. *Physical Review E*, 67(2):026608. (Cited on page 97.)

[Malomed, 2014] Malomed, B. A. (2014). Spatial solitons supported by localized gain. *JOSA B*, 31(10):2460–2475. (Cited on page 97.)

[Marconi, 2014a] Marconi, M., Javaloyes, J., Balle, S., and Giudici, M. (2014a). How Lasing Localized Structures Evolve out of Passive Mode Locking. *Physical Review Letters*, 112(22):223901. (Cited on pages 15, 21, 24, and 63.)

[Marconi, 2015a] Marconi, M., Javaloyes, J., Balle, S., and Giudici, M. (2015a). Passive Mode-Locking and Tilted Waves in Broad-Area Vertical-Cavity Surface-Emitting Lasers. *IEEE Journal of Selected Topics in Quantum Electronics*, 21(1):85–93. (Cited on page 16.)

[Marconi, 2014b] Marconi, M., Javaloyes, J., Barland, S., Balle, S., and Giudici, M. (2014b). Tilted waves and passive mode-locking in multi-transverse mode vcsels. (Cited on pages 16 and 93.)

[Marconi, 2015b] Marconi, M., Javaloyes, J., Barland, S., Balle, S., and Giudici, M. (2015b). Vectorial dissipative solitons in vertical-cavity surface-emitting lasers with delays. *Nature Photonics*, 9(7):450–455. (Cited on page 87.)

[Mc Laughlin, 1983] Mc Laughlin, D., Moloney, J. V., and Newell, A. C. (1983). Solitary waves as fixed points of infinite-dimensional maps in an optical bistable ring cavity. *Physical review letters*, 51(2):75. (Cited on page 5.)

[McDonald, 1990] McDonald, G. S. and Firth, W. (1990). Spatial solitary-wave optical memory. *JOSA B*, 7(7):1328–1335. (Cited on page 5.)

[Michalzik, 2013] Michalzik, R. (2013). Vcsels: A research review. *VCSELs*, pages 3–18. (Cited on page 8.)

[Mignot, 2009] Mignot, A., Feugnet, G., Schwartz, S., Sagnes, I., Garnache, A., Fabre, C., and Pocholle, J.-P. (2009). Single-frequency external-cavity semiconductor ring-laser gyroscope. *Optics letters*, 34(1):97–99. (Cited on page 22.)

[Minardi, 2010] Minardi, S., Eilenberger, F., Kartashov, Y. V., Szameit, A., Röpke, U., Kobelke, J., Schuster, K., Bartelt, H., Nolte, S., Torner, L., Lederer, F., Tünnermann, A., and Pertsch, T. (2010). Three-Dimensional Light Bullets in Arrays of Waveguides. *Physical Review Letters*, 105(26):263901. (Cited on page 17.)

[Newell, 1969] Newell, A. C. and Whitehead, J. A. (1969). Finite bandwidth, finite amplitude convection. *Journal of Fluid Mechanics*, 38(2):279–303. (Cited on page 2.)

[Nikiforov, 2016] Nikiforov, O., Jaurigue, L., Drzewietzki, L., Lüdge, K., and Breuer, S. (2016). Experimental demonstration of change of dynamical properties of a passively mode-locked semiconductor laser subject to dual optical feedback by dual full delay-range tuning. *Optics Express*, 24(13):14301–14310. (Cited on page 86.)

[Noblet, 2012] Noblet, Y. and Ackemann, T. (2012). Analysis of spatial emission structures in vertical-cavity surface-emitting lasers with feedback from a volume bragg grating. *Physical Review A*, 85(5):053812. (Cited on page 38.)

[Otto, 2012] Otto, C., Lüdge, K., Vladimirov, A., Wolfrum, M., and Schöll, E. (2012). Delay-induced dynamics and jitter reduction of passively mode-locked semiconductor lasers subject to optical feedback. *New Journal of Physics*, 14(11):113033. (Cited on pages 86 and 92.)

[Ouvrard, 2005] Ouvrard, A., Garnache, A., Cerutti, L., Genty, F., and Romanini, D. (2005). Single-frequency tunable sb-based vcsels emitting at 2.3 μm. *IEEE Photonics Technology Letters*, 17(10):2020–2022. (Cited on page 22.)

[Ouyang, 1991] Ouyang, Q. and Swinney, H. L. (1991). Transition from a uniform state to hexagonal and striped turing patterns. *Nature*, 352(6336):610–612. (Cited on page 3.)

[Palma, 1997] Palma, C. and Bagini, V. (1997). Extension of the fresnel transform to abcd systems. *JOSA A*, 14(8):1774–1779. (Cited on page 35.)

[Panajotov, 2014] Panajotov, K. and Tlidi, M. (2014). Chaotic behavior of cavity solitons induced by time delay feedback. *Optics letters*, 39(16):4739–4742. (Cited on page 87.)

[Paschotta, 2002] Paschotta, R., Häring, R., Garnache, A., Hoogland, S., Tropper, A., and Keller, U. (2002). Soliton-like pulse-shaping mechanism in passively mode-locked surface-emitting semiconductor lasers. *Applied Physics B*, 75(4):445–451. (Cited on page 14.)

[Pedaci, 2008a] Pedaci, F., Barland, S., Caboche, E., Genevet, P., Giudici, M., Tredicce, J. R., Ackemann, T., Scroggie, A., Firth, W., Oppo, G.-L., et al. (2008a). All-optical delay line using semiconductor cavity solitons. *Applied Physics Letters*, 92(1):011101. (Cited on pages 7, 9, and 23.)

[Pedaci, 2006] Pedaci, F., Genevet, P., Barland, S., Giudici, M., and Tredicce, J. (2006). Positioning cavity solitons with a phase mask. *Applied physics letters*, 89(22):221111. (Cited on pages 7, 9, and 23.)

[Pedaci, 2008b] Pedaci, F., Tissoni, G., Barland, S., Giudici, M., and Tredicce, J. (2008b). Mapping local defects of extended media using localized structures. *Applied Physics Letters*, 93(11):111104. (Cited on pages 7 and 23.)

[Pieczarka, 2020] Pieczarka, M., Poletti, D., Schneider, C., Höfling, S., Ostrovskaya, E. A., Sęk, G., and Syperek, M. (2020). Observation of gain-pinned dissipative solitons in a microcavity laser. *APL Photonics*, 5(8):086103. (Cited on page 97.)

[Puzyrev, 2016] Puzyrev, D., Vladimirov, A., Gurevich, S., and Yanchuk, S. (2016). Modulational instability and zigzagging of dissipative solitons induced by delayed feedback. *Physical Review A*, 93(4):041801. (Cited on page 87.)

[Ramazza, 2003] Ramazza, P., Boccaletti, S., Bortolozzo, U., and Arecchi, F. (2003). Control of localized structures in an optical feedback interferometer. *Chaos: An Interdisciplinary Journal of Nonlinear Science*, 13(1):335–341. (Cited on page 4.)

[Richter, 2005] Richter, R. and Barashenkov, I. V. (2005). Two-dimensional solitons on the surface of magnetic fluids. *Physical review letters*, 94(18):184503. (Cited on page 4.)

[Rosanov, 1990] Rosanov, N. N. and Khodova, G. V. (1990). Diffractive autosolitons in nonlinear interferometers. *Journal of the Optical Society of America B*, 7(6):1057. (Cited on page 5.)

[Saleh, 2019] Saleh, B. E. and Teich, M. C. (2019). *Fundamentals of photonics*. john Wiley & sons. (Cited on page 32.)

[Schäpers, 2000] Schäpers, B., Feldmann, M., Ackemann, T., and Lange, W. (2000). Interaction of localized structures in an optical pattern-forming system. *Physical Review Letters*, 85(4):748. (Cited on page 5.)

[Schelte, 2017] Schelte, C., Panajotov, K., Tlidi, M., and Gurevich, S. V. (2017). Bifurcation structure of cavity soliton dynamics in a vertical-cavity surface-emitting laser with a saturable absorber and time-delayed feedback. *Physical Review A*, 96(2):023807. (Cited on page 87.)

[Schemmelmann, 2017] Schemmelmann, T., Tabbert, F., Pimenov, A., Vladimirov, A. G., and Gurevich, S. V. (2017). Delayed feedback control of self-mobile cavity solitons in a wide-aperture laser with a saturable absorber. *Chaos: An Interdisciplinary Journal of Nonlinear Science*, 27(11):114304. (Cited on page 87.)

[Segel, 1969] Segel, L. A. (1969). Distant side-walls cause slow amplitude modulation of cellular convection. *Journal of Fluid Mechanics*, 38(1):203–224. (Cited on page 2.)

[Seghilani, 2016] Seghilani, M. S., Myara, M., Sellahi, M., Legratiet, L., Sagnes, I., Beaudoin, G., Lalanne, P., and Garnache, A. (2016). Vortex Laser based on III-V semiconductor metasurface: direct generation of coherent Laguerre-Gauss modes carrying controlled orbital angular momentum. *Scientific Reports*, 6(1):38156. (Cited on page 97.)

[Sekimura, 2013] Sekimura, T., Noji, S., Ueno, N., and Maini, P. (2013). *Morphogenesis and pattern formation in biological systems: experiments and models*. Springer Science & Business Media. (Cited on page 1.)

[Siegman, 1986] Siegman, A. E. (1986). *Lasers*. University science books. (Cited on pages 34 and 35.)

[Stuart, 1966] Stuart, J. (1966). Studies in non-linear stability theory. by wiktor eckhaus. springer-verlag, 1965. 117 pp. dm 22. *Journal of Fluid Mechanics*, 25(2):414–415. (Cited on page 2.)

[Swift, 1977] Swift, J. and Hohenberg, P. C. (1977). Hydrodynamic fluctuations at the convective instability. *Physical Review A*, 15(1):319. (Cited on page 2.)

[Tanguy, 2008] Tanguy, Y., Ackemann, T., Firth, W. J., and Jäger, R. (2008). Realization of a Semiconductor-Based Cavity Soliton Laser. *Physical Review Letters*, 100(1):013907. (Cited on page 10.)

[Taranenko, 1997] Taranenko, V. B., Staliunas, K., and Weiss, C. O. (1997). Spatial soliton laser: Localized structures in a laser with a saturable absorber in a self-imaging resonator. *Physical Review A*, 56(2):1582–1591. (Cited on page 38.)

[Tlidi, 1994] Tlidi, M., Mandel, P., and Lefever, R. (1994). Localized structures and localized patterns in optical bistability. *Physical Review Letters*, 73(5):640–643. (Cited on page 5.)

[Tlidi, 2014] Tlidi, M., Staliunas, K., Panajotov, K., Vladimirov, A. G., and Clerc, M. G. (2014). Localized structures in dissipative media: from optics to plant ecology. *Philosophical Transactions of the Royal Society A: Mathematical, Physical and Engineering Sciences*, 372(2027):20140101. (Cited on page 1.)

[Triki, 2008] Triki, M., Cermak, P., Cerutti, L., Garnache, A., and Romanini, D. (2008). Extended continuous tuning of a single-frequency diode-pumped vertical-external-cavity surface-emitting laser at 2.3 μm. *IEEE Photonics Technology Letters*, 20(23):1947–1949. (Cited on page 22.)

[Tropper, 2004] Tropper, A., Foreman, H., Garnache, A., Wilcox, K., and Hoogland, S. (2004). Vertical-external-cavity semiconductor lasers. *Journal of Physics D: Applied Physics*, 37(9):R75. (Cited on pages 14 and 22.)

[Turing, 1952] Turing, A. (1952). The chemical basis of morphogenesis. *Philosophical Transactions of the Royal Society of London*, 237. (Cited on page 1.)

[Umbanhowar, 1996] Umbanhowar, P. B., Melo, F., and Swinney, H. L. (1996). Localized excitations in a vertically vibrated granular layer. *Nature*, 382(6594):793–796. (Cited on page 4.)

[Vladimirov, 2014] Vladimirov, A., Pimenov, A., Gurevich, S., Panajotov, K., Averlant, E., and Tlidi, M. (2014). Cavity solitons in vertical-cavity surface-emitting lasers. *Philosophical Transactions of the Royal Society A: Mathematical, Physical and Engineering Sciences*, 372(2027):20140013. (Cited on page 87.)

[Vladimirov, 2005] Vladimirov, A. G. and Turaev, D. (2005). Model for passive mode locking in semiconductor lasers. *Physical Review A*, 72(3):033808. (Cited on page 92.)

[Yariv, 1991] Yariv, A. (1991). *Optical electronics*. Saunders College Publishing. (Cited on page 31.)

[Yoshida, 1982] Yoshida, A. (1982). Spherical aberration in beam optical systems. *Applied Optics*, 21(10):1812. (Cited on pages 76 and 77.)

[Yoshida, 1975] Yoshida, A. and Asakura, T. (1975). Effect of aberrations on off-axis gaussian beams. *Optics Communications*, 14(2):211–214. (Cited on page 76.)

[Yoshida, 1976] Yoshida, A. and Asakura, T. (1976). Diffraction patterns of off-axis gaussian beams in the presence of third-order spherical aberration in the optical system. *Optics Communications*, 19(3):387–392. (Cited on page 78.)

[Yoshida, 1978] Yoshida, A. and Asakura, T. (1978). Diffraction patterns of off-axis gaussian beams in the optical system with astigmatism and coma. *Optics Communications*, 25(2):133–136. (Cited on page 77.)

[Yoshida, 1979] Yoshida, A. and Asakura, T. (1979). Focusing properties of an off-axis gaussian beam. *Optics & Laser Technology*, 11(1):49–54. (Cited on page 76.)